Design and commissioning of a multi-reflection time-of-flight mass-spectrometer for Barium tagging with nEXO

Kevin Murray

Department of Physics

McGill University, Montreal

A thesis submitted in partial fulfillment of the requirements for the degree of

Doctor of Philosophy

Abstract

The mechanism by which neutrino masses arise is still unknown, yet it is clear from neutrino oscillation experiments that they do have mass. The observation of neutrinoless double beta decay ($0\nu\beta\beta$), a lepton number violating process that is beyond the current Standard Model, could shed light on the neutrino mass scale and hierarchy. The existence of this decay would show that the neutrino is a Majorana particle i.e. it is its own antiparticle. This could provide a natural explanation for the smallness of the neutrino masses, as well as a measurement of the effective Majorana neutrino mass. The proposed nEXO experiment aims to search for $0\nu\beta\beta$ in ^{136}Xe with a time-projection chamber and five-tonnes of enriched liquid Xe. The Ba-tagging project is a potential future upgrade to nEXO, that seeks to provide a positive identification of a candidate $0\nu\beta\beta$ event as a true ^{136}Xe $\beta\beta$ decay, by extracting and identifying the daughter ^{136}Ba ion. A spatially resolved multi-element laser ablation ion source (LAS) was developed for the Ba-tagging system along with a multi-reflection time-of-flight mass-spectrometer (MRTOF). The LAS uses a motorized mirror mount to precisely position the ablation laser spot on the surface of a multi-element target. Elements within the target can be selectively ablated with a spatial resolution of $\sim 50\mu$m for calibration of the MRTOF. The MRTOF will be used for systematic studies of the Ba-tagging extraction technique, as well as confirmation of the ^{136}Ba ion isotope mass. A mass-resolving power of m/Δm = 5×10^4 is needed to separate ^{136}Xe from ^{136}Ba, which can be achieved by the MRTOF which is expected to have a mass-resolving power in excess of m/Δm > 1×10^5.

Résumé

Le mécanisme par lequel émergent les masses des neutrinos est encore inconnu, mais il est clair d'après les expériences d'oscillation des neutrinos qu'ils ont bien une masse. L'observation de la double désintégration bêta sans neutrinos ($0\nu\beta\beta$), un processus au-delà du modèle standard actuel qui violerait la conservation du nombre leptonique, pourrait éclairer l'échelle de masse des neutrinos et leur hiérarchie. L'existence de cette désintégration démontrerait que le neutrino est une particule de Majorana, c'est-à-dire qu'il est sa propre antiparticule. Cela pourrait fournir une explication naturelle pour la petitesse des masses des neutrinos, ainsi qu'une mesure de la masse effective des neutrinos de Majorana. L'expérience proposée nEXO vise à rechercher le $0\nu\beta\beta$ dans du ^{136}Xe avec une chambre à dérive et cinq tonnes de xénon enrichi liquide. Le projet désigné « Ba-tagging »est une potentielle amélioration future de nEXO qui vise à identifier de façon positive, parmi des événements candidats, un événement de $0\nu\beta\beta$ dans du ^{136}Xe en extrayant et en identifiant l'ion fils de ^{136}Ba. Une source d'ions à ablation laser résolue spatialement pour éléments multiples (« LAS »), ainsi qu'un spectromètre de masse à temps de vol avec réflexions multiples (« MRTOF »), ont été développés pour le système de Ba-tagging. Le LAS utilise une monture à miroir motorisée pour positionner précisément le faisceau d'ablation laser sur la surface d'une cible à éléments multiples. Les éléments de la cible peuvent être sélectivement pulvérisés avec une résolution spatiale de $\sim 50\mu$m découlant de la calibration du MRTOF. Le MRTOF sera utilisé pour des études systématiques de la technique d'extraction de Ba-tagging, ainsi que pour confirmer la masse isotopique de l'ion de ^{136}Ba. En vertu de sa résolution massique prévue de $m/\Delta m > 1\times10^5$, le MRTOF peut fournir la résolution de $m/\Delta m = 5\times10^4$ nécessaire pour séparer le ^{136}Ba du ^{136}Xe.

Acknowledgements

As we all know, research is not conducted in isolation, which is especially true for research involving extremely heavy vacuum equipment. First and foremost I would like to thank my supervisor, Dr. Thomas Brunner, for giving me the opportunity to work on this project. It has been a great privilege to watch the Bunner Neutrino Lab (BνL) grow from humble beginnings into its current form, and I'm excited to see what the future holds for the lab. The next thank you is to Dr. Christopher Chambers, who was behind the scenes for almost all the work to follow. Chris was instrumental in the assembly of the LAS, MRTOF, and much of the infrastructure that comprises the current Ba-tagging system. Moreover, he suffered through endless edits to the LAS manuscript to get it published. Above all, Chris showed me the immeasurable impact that a great Postdoc can have on a project. To all the members of BνL, I appreciate all of the help and support in and outside of the lab.

Thank you to my fellow nEXO collaborators and Ba-taggers for many helpful discussions over the years, and especially to Dr. William Fairbank for all of his help and advice with the LAS and MRTOF. I had the great pleasure of visiting the EXO-200 experiment in the flesh and I'm hopeful that someday I will be able to visit nEXO. Thank you to the present and former members of the TITAN group at TRIUMF, including Dr. Ania Kwiatkowski, Dr. Yang Lan, who designed the LPT, and Dr. Pascal Reiter, who contributed to the development of the LAS and MRTOF through helpful discussions and suggestions. Thank you to Dr. Peter Schury, for hosting me at the RIKEN Nishina center in Japan for a 3 month fellowship, and for providing us with the high-voltage switches used in the MRTOF. Thank you to Eamon Egan from the McGill Physics department, for all of his help with the MRTOF's electronics

and in particular the timing system.

Thank you to my friends and family for all their love and support during the many long years of graduate studies, and to Carolina, my wife-to-be. I would like to dedicate this work to my grand-parents, David and Avril Veitch, who always took an interest in my studies. I hope that they are proud.

Contribution of the Authors

The project of Ba-tagging, that aims to extract and identify the single daughter ^{136}Ba ion from the $\beta\beta$ decay of ^{136}Xe, presents an extremely difficult technical challenge. Success in the project would improve the nEXO experiment's sensitivity to $0\nu\beta\beta$, as well as showcase multiple advancements in the field of ion transport and trapping. The work of the author was centred on the development of the LAS and MRTOF for the Ba-tagging system for a potential future upgrade of nEXO.

The LAS uses a novel technique to selectively ablate the materials in a multi-element target for the calibration of mass-spectrometers and other ion traps. Thus the LAS is a powerful tool not only for Ba-tagging, but for mass spectrometry as well, since it can produce diverse species of ions that span a large mass range. This work concerns the development of the LAS system and its application to the commissioning of the MRTOF. The LAS/MRTOF combination constitutes a unique system in which an MRTOF is coupled to a 2D scanning LAS. This system has so far demonstrated an available mass-resolving power of up to m/Δm = 2×10^4 with Cu^+ ions. The MRTOF has been designed to achieve a mass-resolving power in excess of 1×10^5 when supplied with cooled ions from the Linear Paul Trap, to meet the requirements of Ba-tagging. A summary of the contributions from the author to each chapter is given below, along with contributions from the co-authors.

Chapter 1: An introduction in which the author summarizes the motivations for Ba-tagging as well as the development of the LAS and MRTOF for the Ba-tagging system.

Chapter 2: The author gives an overview of the theoretical framework for massive neutrinos and neutrinoless double beta decay, which is the broader context in which the thesis work takes place.

Chapter 3: The author gives an overview of the nEXO experiment and the potential upgrade of the Ba-tagging system. An overview is also given of the different approaches to Ba-tagging which are being studied in Canada and the US.

Chapter 4: The author presents the first LAS system and the technique by which elements in a multi-element target can be selectively ablated. In this chapter the spatial resolution with which the LAS can selectively ablate material is characterized by the author. The first LAS system was designed by undergraduate students Zachary Feng and Louis Richez, and assembled by Rane Simpson and Dr. Yuta Ito. The LAS was commissioned by Dr. Yuta Ito, who developed the scanning technique. The data presented was recorded by the author with the help of Dr. Christopher Chambers, with the exception of the ion transport efficiency data which was recorded by Dr. Yang Lan.

Chapter 5: The author presents the theoretical principles that underpin the design and operation of the MRTOF. The design of the MRTOF and the ion-optics that precede it are presented, where all 3D models shown were created by the author, with the exception of the Faraday Cup which was designed by Dr. Christopher Chambers. All technical drawings of the models displayed in the appendix were sketched by the author, under the supervision of Xiao Shang. The electrodes comprising the MRTOF and ion optics were machined by the Physics department machine shop at the Université de Montreal. Simulations with SIMION to characterize the MRTOF's performance were conducted by the author, with simulated ions from the LPT's RFQ buncher provided by Dr. Yang Lan as the ion source. The code used to calculate and plot the emittance of the ion bunch in Fig. 5.2 was supplied by Dr. Yang Lan.

Chapter 6: The author presents the clean assembly of the MRTOF, conducted by the author and with the help of Dr. Christopher Chambers to move and assemble vacuum pieces. The rail-system on which the MRTOF was assembled was designed by Dr. Christopher Chambers.

Chapter 7: The process of commissioning the MRTOF and resulting first measurements with Cu^+ ions is presented. Eamon Eagan from the physics department helped with the verilog syntax and logic when programming the FPGA timing system. The HV switches used for trapping were provided by Dr. Peter Schury from RIKEN. Labview software to control the power-supplies, laser and the DAQ system was written by the author. The presented measurements were recorded by the author.

Chapter 8: Concluding remarks are given by the author.

Contents

List of Figures

List of Tables

List of Acronyms

$0\nu\beta\beta$: Neutrinoless double beta decay

$2\nu\beta\beta$: Two neutrino double beta decay

FC : Faraday cup

FPGA : Field-programmable gate array

FWHM : Full Width Half Maximum

ID : Inner Diameter

IH : Inverted hierarchy

LAS : Laser ablation ion source

LPT : Linear Paul trap

MRP : Mass-resolving power

MRTOF : Multi-reflection time-of-flight mass-spectrometer

NH : Normal hierarchy

OD : Outer Diameter

OFHC : Oxygen-free high thermal conductivity

RFQ : Radio Frequency Quadrupole

ROI : Region of interest

SEMF : Semi-empirical mass formula

SHV : Safe high voltage

SM : Standard Model

TOF : Time of flight

UHV : Ultra-high vacuum

Chapter 1

Introduction

The discovery of neutrino oscillations has demonstrated the existence of nonzero neutrino mass eigenstates [1, 2], which suggests that the current Standard Model (SM) description of neutrinos is inadequate. To build a more complete description, the fundamental properties of neutrinos must be probed further. Neutrinoless double beta decay ($0\nu\beta\beta$) is a lepton number violating process that, if observed, would confirm the Majorana nature of neutrinos [3], and provide an excellent probe into the neutrino mass hierarchy and absolute mass scale. Moreover, since lepton number conservation is assumed as a symmetry in the formulation of the SM, the observation of $0\nu\beta\beta$ would provide further evidence for physics beyond the SM [4].

The proposed nEXO experiment aims to search for $0\nu\beta\beta$ with a five-tonne liquid Xe time-projection chamber, enriched to 90% in the isotope ^{136}Xe [5]. The sensitivity of nEXO to the $0\nu\beta\beta$ half-life is projected to reach 1.35×10^{28} yr at 90% confidence level in 10 years of data taking [6]. Since the $\beta\beta$ decay of ^{136}Xe produces the stable isotope ^{136}Ba, the search for $0\nu\beta\beta$ decay in ^{136}Xe allows for the unique opportunity to extract and identify the decay daughter from the detector volume in a process called Ba-tagging. Ba-tagging is a potential future upgrade to nEXO which can suppress all backgrounds to the $0\nu\beta\beta$ decay search, except those that arise from $2\nu\beta\beta$. One approach to Ba-tagging, currently under development at multiple Canadian institutions, is to extract the decay daughter together with

a small volume of liquid Xe at the location of a candidate event. Following a phase-change from liquid to gaseous Xe, the ion is separated from Xe with an RF funnel and transported and trapped in a linear Paul trap (LPT), where the Ba daughter will be tagged with laser fluorescence spectroscopy. Ions will then be ejected from the LPT to a multi-reflection time-of-flight mass-spectrometer (MRTOF) for mass identification. Beyond identification of the Ba isotope, the MRTOF is also essential for performing systematic studies of the ion extraction technique. A mass-resolving power (MRP) of $m/\Delta m \approx 5 \times 10^4$ is needed to separate ^{136}Xe from ^{136}Ba, which makes the MRTOF an ideal mass spectrometer for Ba-tagging, as they have demonstrated MRP's well in excess of $m/\Delta m \approx 1 \times 10^5$ [7]. An MRTOF has been designed for the Ba-tagging system to meet this MRP requirement [8].

Laser ablation ion sources (LAS's) are ideal for testing and calibrating the constituent devices of the Ba-tagging system, since they can produce ions in vacuum or gas. A LAS that can spatially resolve and selectively ablate different elements from a multi-element target, with a spatial resolution of 50 μm [9], has been used for the commissioning of the MRTOF. The work to follow will discuss the project of Ba-tagging and its broader context. Followed by the development of the spatially-resolved LAS for Ba-tagging, as well as the MRTOF's design and commissioning with the LAS.

Chapter 2

Neutrino Theory

The neutrino was first postulated theoretically by Wolfgang Pauli in 1930 [10], to explain the continuous beta decay energy spectrum that had been discovered over a decade prior. The continuous energy spectrum could be neatly explained in the context of a 3-body decay, which was preferable to giving up the notion of energy conservation. Thus he proposed that an electrically-neutral, but undetected particle was also emitted in the process, and that the particle should be spin $\frac{1}{2}$ to conserve angular momentum. The mysterious particle was later dubbed the *neutrino* by 'the architect of the nuclear age', Enrico Fermi, who firmly established the theory of beta decay in 1934 [11].

It wasn't until 1956 that neutrinos were detected directly by Cowan and Reines [12], through the inverse beta decay reaction process

$$p + \bar{\nu}_e \rightarrow n + e^+ \ . \tag{2.1}$$

The antineutrino flux from a nearby nuclear reactor was measured using a water tank containing dissolved $CdCl_2$ as a neutron absorber. The tank was surrounded by two liquid scintillators that could detect the coincident 511 keV photons from electron-positron annihilation, as well as the γ photons produced from neutron capture on ^{113}Cd.

The discovery of muon neutrinos by Bruno Pontecorvo in 1962 demonstrated the existence of more than one flavour of neutrino [13]. An experiment at Brookhaven AGS used a 15 GeV proton beam to irradiate a beryllium target, creating showers of pions and kaons, which decayed into muons and muon neutrinos [14]. If ν_μ and ν_e were the same, then the reactions

$$\nu_\mu + n \rightarrow \mu^- + p \tag{2.2}$$

$$\bar{\nu}_\mu + p \rightarrow \mu^+ + n \tag{2.3}$$

and

$$\nu_e + n \rightarrow e^- + p \tag{2.4}$$

$$\bar{\nu}_e + p \rightarrow e^+ + n \tag{2.5}$$

should occur at the same rates [15]. Muons were subsequently detected with a spark chamber, and easily distinguished from electrons. The excess of muons compared to electrons demonstrated that $\nu_\mu \neq \nu_e$. When the tau lepton was discovered in 1975 [16], it exhibited the same continuous energy spectrum as the electron, hence it was immediately expected to be accompanied by an associated tau neutrino as well. The tau neutrino was detected directly in 2000 at Fermilab with the Tevatron accelerator [17]. Thus it was established that there are three neutrino flavours. However, there was a problem. By the mid 1960's, experiments had become sensitive enough to measure the flux of neutrinos coming from the sun, and the Homestake experiment discovered that the flux of electron neutrinos from the sun was about a third of what was predicted [18]. This discrepancy became known as the 'Solar Neutrino' problem [19].

Pontecorvo, inspired by kaon-antikaon oscillations, suspected that perhaps neutrinos underwent neutrino-antineutrino oscillations in 1957 [20]. In 1968, he proposed that if neutrinos had mass they could oscillate from one flavour to another [21], building on a theoretical framework that had been established by Maki, Nakigawa and Sakata [22]. The 'missing' solar neutrinos could therefore have been electron neutrinos that had oscillated to another

flavour during flight. This was a controversial idea however, since the Standard Model required neutrinos to be massless and would need to be modified to include massive neutrinos. Since then, there has been mounting evidence confirming that neutrinos do indeed oscillate between flavour eigenstates. Such as the observation of atmospheric neutrino oscillations neutrinos by Super-Kamiokande [23] in 1998. As well as the observation of solar neutrinos by the Sudbury Neutrino Observatory (SNO) in 2001, that finally resolved the Solar Neutrino problem [24].

2.1 Neutrino Oscillations

Neutrino flavour eigenstates, $(\nu_e, \nu_\mu, \nu_\tau)$, can be expressed as linear combinations of mass states, (ν_1, ν_2, ν_3), with the matrix transformation

$$\begin{pmatrix} \nu_e \\ \nu_\mu \\ \nu_\tau \end{pmatrix} = \begin{pmatrix} U_{e1} & U_{e2} & U_{e3} \\ U_{\mu 1} & U_{\mu 2} & U_{\mu 3} \\ U_{\tau 1} & U_{\tau 2} & U_{\tau 3} \end{pmatrix} \cdot \begin{pmatrix} \nu_1 \\ \nu_2 \\ \nu_3 \end{pmatrix}, \tag{2.6}$$

where $U_{\alpha i}$ are the elements of the Pontecorvo-Maki-Nakigawa-Sakata (PMNS) matrix [21, 22]. The PMNS matrix can be parameterised as

$$U = \begin{pmatrix} c_{12}c_{13} & s_{12}c_{13} & s_{13}e^{-i\delta} \\ -s_{12}c_{23} - c_{12}s_{23}s_{13}e^{i\delta} & c_{12}c_{23} - s_{12}s_{23}s_{13}e^{i\delta} & s_{23}c_{13} \\ s_{12}s_{23} - c_{12}c_{23}s_{13}e^{i\delta} & -c_{12}s_{23} - s_{12}c_{23}s_{13}e^{i\delta} & c_{23}c_{13} \end{pmatrix} \cdot P \tag{2.7}$$

Where $c_{ij} \equiv \cos(\theta_{ij})$, $s_{ij} \equiv \sin(\theta_{ij})$ with mixing angles θ_{ij}, δ is the Dirac CP-violating phase [25]. The matrix P is a unit matrix in the case of neutrinos being Dirac particles, or a diagonal matrix

$$P_{Majorana} = \begin{pmatrix} e^{i\alpha_1} & 0 & 0 \\ 0 & e^{i\alpha_2} & 0 \\ 0 & 0 & 1 \end{pmatrix} \tag{2.8}$$

in the case that neutrinos are Majorana particles, where α_1, α_1 are the phases associated with the Majorana aspect of the neutrino.

To derive the probability of oscillation suppose that a neutrino, $\nu_\alpha(\alpha = e, \mu, \tau)$, is produced with a particular flavour eigenstate in vacuum

$$|\nu(t=0)\rangle = |\nu_\alpha\rangle = \sum_i U^*_{\alpha i} |\nu_i\rangle \,, \tag{2.9}$$

where $U*_{\alpha i}$ are the elements of the PMNS matrix from Eq. (2.7). Each mass eigenstate evolves with a factor of $e^{-iE_i t}$, since they are eigenstates of the Hamiltonian in vacuum [25]. Thus the flavour eigenstate at time t can be expressed as

$$|\nu_\alpha(t)\rangle = \sum_i U^*_{\alpha i} e^{-iE_i t} |\nu_i\rangle \,. \tag{2.10}$$

Using Eq. (2.9) to solve for $|\nu_i\rangle$, $|\nu_\alpha(t)\rangle$ can be expressed as

$$|\nu_\alpha(t)\rangle = \sum_i U^*_{\alpha i} e^{-iE_i t} \sum_\beta U_{\beta i} |\nu_\beta\rangle \,. \tag{2.11}$$

The probability then of finding the neutrino in a different flavour eigenstate ν_β is

$$P(\nu_\alpha \to \nu_\beta) = |\langle \nu_\beta | \nu(t) \rangle|^2 = \left| \sum_i U_{\beta i} U^*_{\alpha i} e^{-iE_i t} \right|^2 \tag{2.12}$$

$$= \left(\sum_i U_{\beta i} U^*_{\alpha i} e^{-iE_i t} \right) \left(\sum_j U^*_{\beta j} U_{\alpha j} e^{iE_j t} \right) \tag{2.13}$$

$$= \sum_{ij} U_{\beta i} U^*_{\alpha i} U^*_{\beta j} U_{\alpha j} e^{-i(E_i - E_j)t}. \tag{2.14}$$

Adopting the ultra-relativistic limit where $L \approx ct$ is the distance travelled by the neutrino and $E_i = \sqrt{p^2 + m_i^2} \approx p + m_i^2/2p$, the oscillation probability can be written as [25]

$$P(\nu_\alpha \to \nu_\beta) = \sum_{ij} U_{\beta i} U^*_{\alpha i} U^*_{\beta j} U_{\alpha j} e^{-i\Delta m^2_{ij} L/E}, \tag{2.15}$$

where $\Delta m^2_{ji} = m^2_j - m^2_i$ is the squared difference between the neutrino masses for the neutrino mass eigenstates ν_j and ν_i. It is also assumed in Eq. (2.15) that the mass eigenstates have a well defined momentum, and that these are all equal, i.e. $p_i = p$. From the above equation there arises a few important implications. For neutrino flavour oscillation to occur it is clear that neutrinos must have mass and that these masses are not degenerate, $\Delta m^2_{ji} \neq 0$. Thus the observation of neutrino oscillations confirms that neutrinos do have masses, although it is still uncertain as to how these masses are generated. Notice also that in Eq. (2.15), neutrino oscillation is only dependent on the squared differences between mass eigenvalues. As a consequence, oscillation experiments cannot probe the scale of the lightest neutrino mass. Furthermore, the neutrino mass hierarchy is yet unsettled. There are two possible ordering scenarios permissible with the current data. One in which $m_1 < m_2 < m_3$, called normal hierarchy (NH), and one in which $m_3 < m_1 < m_2$, called inverted hierarchy (IH), shown in Fig. 2.1. The gap between m_1 and m_2, Δm^2_{sol}, has been measured with solar neutrino oscillation data, whereas the gap between the m_3 and m_1/m_2 , Δm^2_{atm}, has been measured by atmospheric neutrino oscillation observations. Measurements for the squared mass differences and mixing angles are shown in Table 2.1, for both the NH and IH cases.

Since the SM predicts that neutrinos are strictly massless, the observation of neutrino oscillation constitutes evidence for physics beyond the SM, requiring the SM to be extended to include a theoretical understanding of massive neutrinos [28]. There are two main ways to

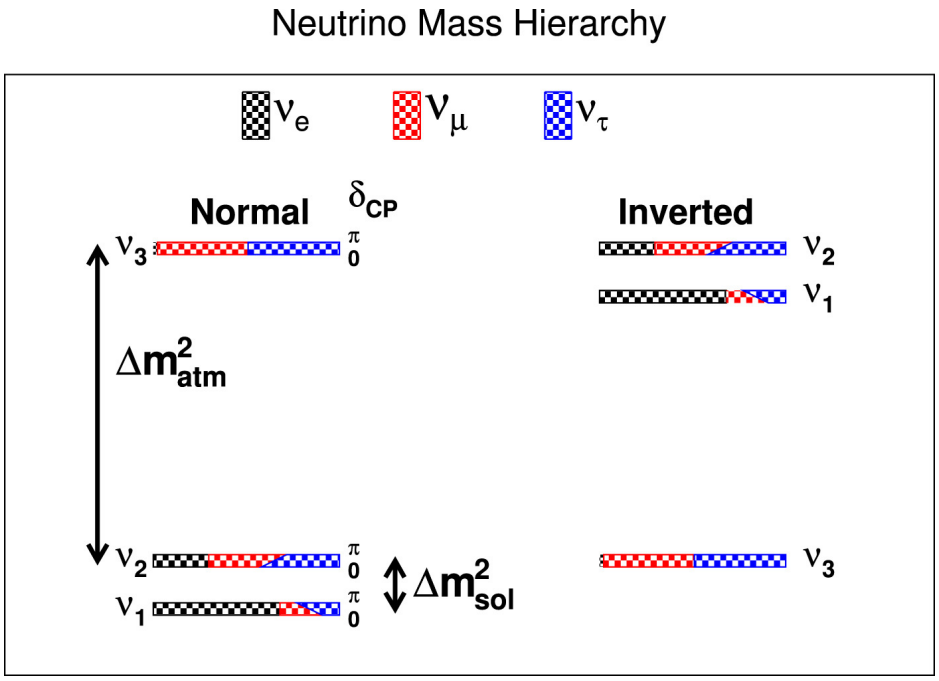

Figure 2.1 Diagram of the neutrino mass hierarchy, where $\Delta m^2_{\text{atm}} \sim |\Delta m^2_{31}| \sim |\Delta m^2_{32}|$ and $\Delta m^2_{\text{sol}} \sim |\Delta m^2_{21}|$ are the atmospheric and solar mass splittings respectively, reproduced from [26].

Table 2.1 Neutrino oscillation parameters from fit to available data with 3-neutrino mixing scheme, reproduced from [27].

Parameter	Best fit $\pm 1\sigma$
Δm^2_{21} [10^{-5} eV^2]	$7.39^{+0.21}_{-0.20}$
$\lvert\Delta m^2_{31}\rvert$ [10^{-3} eV^2] (NH)	$2.499^{+0.032}_{-0.030}$
$\lvert\Delta m^2_{31}\rvert$ [10^{-3} eV^2] (IH)	$2.509^{+0.032}_{-0.032}$
θ°_{12}	$33.82^{+0.78}_{-0.76}$
θ°_{23} (NH)	$48.3^{+1.2}_{-1.9}$
θ°_{23} (IH)	$48.6^{+1.1}_{-1.5}$
θ°_{13} (NH)	$8.61^{+0.13}_{-0.13}$
θ°_{13} (IH)	$8.65^{+0.13}_{-0.12}$

minimally extend the SM and explain the observed oscillation data. If the neutrino is a Dirac fermion like the other leptons, three additional right-handed neutrino fields ν_R are added to the SM Lagrangian, and total lepton conservation is imposed. From experiments however, the mass of the heaviest neutrino is confined within the range $5 \times 10^{-2} \leq m_h \leq 3 \times 10^{-1}$ eV [29]. Even though the individual neutrino masses are still unknown, precision measurements of the tail of the β-decay energy spectrum have placed an upper bound on the effective electron neutrino mass, $m_\nu < 0.8$ eV$/c^2$ [30], where

$$m_\nu = \sqrt{\sum_i |U_{ei}|^2 m_i^2}. \tag{2.16}$$

It is not understood why the neutrino masses are many orders of magnitude smaller than those of the other leptons. One option is that, since the neutrino is a neutral particle, it could be Majorana fermion. In which case, the neutrino and the antineutrino are the same particle and lepton number is not a conserved symmetry. This is an attractive option since it offers a potential explanation for the smallness of neutrino mass via the see-saw mechanism [31]. Through the see-saw mechanism, small neutrino masses are generated by lepton number violating interactions that are beyond the SM [32].

To better understand the neutrino mass generation mechanism, it is necessary to probe the Dirac or Majorana nature of the neutrino. Since the Majorana phase does not affect the probability for neutrino oscillation, neutrino oscillation data cannot be used as a probe to determine whether the neutrino is Dirac or Majorana. However, the search for the lepton number violating process called neutrinoless double beta decay ($0\nu\beta\beta$), could potentially demonstrate the neutrino is indeed a Majorana particle.

2.2 Neutrinoless Double Beta Decay

The possibility of two neutrino double beta decay ($2\nu\beta\beta$), in which a nucleus simultaneously emits two electrons and two neutrinos

$$\beta^-\beta^- : (A,Z) \rightarrow (A,Z+2) + 2e^- + 2\bar{\nu}_e, \tag{2.17}$$

was first considered by Maria Goeppert Mayer in a 1935 manuscript [33]. Additionally, she calculated the probability for the process to occur as well as an estimate for the half-life of 10^{17} years, where a Q-value of 10 MeV was assumed. Although $2\nu\beta\beta$ is allowed in the Standard Model, the decay is rare since it involves a second-order electroweak process. However, almost 90 years after its inception, $2\nu\beta\beta$ has been observed in over 20 isotopes with measured half-lives ranging from 10^{19} to 10^{23} years [27].

The stability of a nucleus is governed by its mass, which can be expressed with the Semi-Empirical Mass Formula (SEMF) [34]

$$M(A,Z) = Zm_p + Nm_n - a_V A + a_S A^{2/3} + a_C \frac{Z(Z-1)}{A^{1/3}} + a_A \frac{(N-Z)^2}{A} + \delta(A,Z), \tag{2.18}$$

where the last term, $\delta(A,Z)$, is zero for odd A, positive for odd-odd nuclei and negative for even-even nuclei. Thus a plot of $M(A,Z)$ vs. Z results in two shifted parabolas, as shown in Fig. 2.2. Besides $2\nu\beta\beta$, there are three additional ways in which a nucleus may decay to a lighter nucleus with the simultaneous emission of 2 neutrinos [34]

$$\beta^+\beta^+ : (A,Z) \rightarrow (A,Z+2) + 2e^+ + 2\nu_e \tag{2.19}$$

$$ECEC : 2e^- + (A,Z) \rightarrow (A,Z-2) + 2\nu_e \tag{2.20}$$

$$EC\beta^+ : 2e^- + (A,Z) \rightarrow (A,Z-2) + 2\nu_e, \tag{2.21}$$

where β^+ refers to positron emission and EC stands for electron capture. The energy released in the decay, called the Q value, is distributed amongst the decay products as well as the

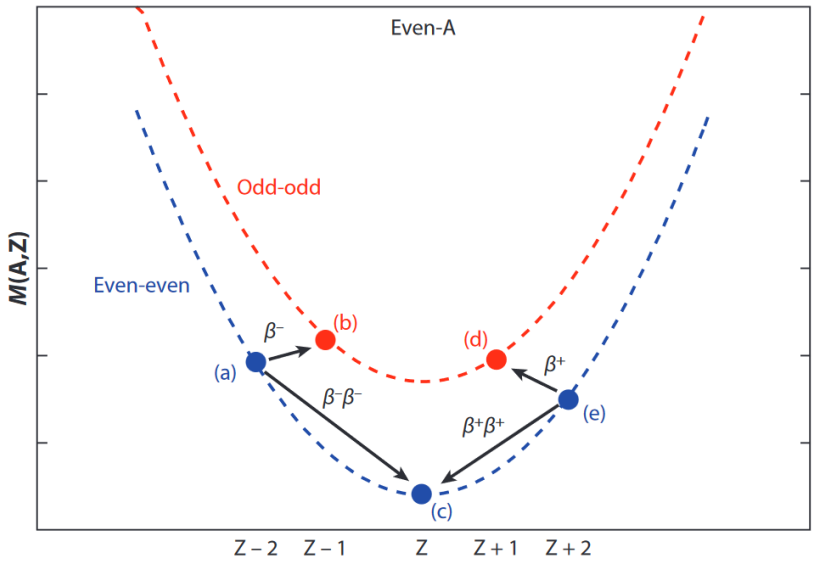

Figure 2.2 Mass parabola plot in which ordinary β decay is suppressed while $\beta\beta$ decay is allowed, reproduced from [34].

recoil of the nucleus which is usually negligible. For $\beta^-\beta^-$ decay the Q value is [34]

$$Q_{\beta\beta} = M(A,Z) - M(A,Z+2) \tag{2.22}$$

where $M(A,Z)$ is the atomic mass of the isotope (A,Z).

Candidate isotopes for the observation of $2\nu\beta\beta$ are ones in which β decay to an isobar with lower mass is kinematically impossible. Therefore, a candidate isotope for $2\nu\beta\beta$ is an even-even nucleus that is lighter than the neighbouring odd-odd $(A,Z+1)$ nucleus. Neutrinoless double beta decay $(0\nu\beta\beta)$, as the name suggests, is a $\beta\beta$ decay in which no neutrinos are produced as shown on the right in Fig. 2.3,

$$(A,Z) \rightarrow (A,Z+2) + 2e^-. \tag{2.23}$$

The half-life for this theoretical decay can be expressed as [35]

$$\left[T_{1/2}^{0\nu\beta\beta}\right]^{-1} = G_{0\nu}|\mathscr{M}|^2|f(m_i,U_{ei})|, \tag{2.24}$$

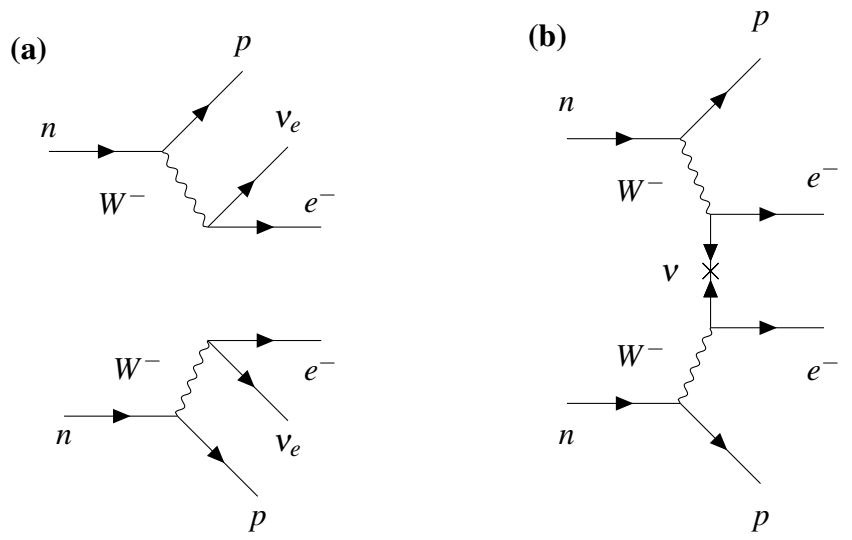

Figure 2.3 (a) Feynman diagram for two neutrino double beta decay. (b) Feynman diagram for neutrinoless double beta decay occurring via light Majorana neutrino exchange.

where $G_{0\nu}$ is the phase space factor, $\mathscr{M}$ is the nuclear matrix element. In the case that $0\nu\beta\beta$ is mediated by light neutrino exchange, the function f can be expressed as

$$f(m_i, U_{ei}) \equiv \frac{m_{\beta\beta}}{m_e} = \frac{1}{m_e}\left|\sum_k U_{ek}^2 m_k\right|. \tag{2.25}$$

From Eq. (2.24) it follows that a lower limit of the $0\nu\beta\beta$ half-life translates into an upper limit on the effective Majorana mass

$$m_{\beta\beta} \leq \frac{m_e}{\mathscr{M}\sqrt{G_{0\nu}T_{1/2}^{0\nu\beta\beta}}}. \tag{2.26}$$

The detection of $0\nu\beta\beta$ relies on the detection of the two emitted electrons. If the recoil of the nucleus is considered to be negligible, the electrons will posses kinetic energies that sum to the Q-value of the decay. In the spectrum of total electron energy, the $0\nu\beta\beta$ signal will appear as a peak at the Q-value as shown in Fig. 2.4. Since a real detector has a finite energy resolution, this peak is broadened over a region, called the region of interest (ROI), that can include contributions from background events that are not $0\nu\beta\beta$. Background events can arise from cosmic rays, radioactivity in the detector materials, and even the $2\nu\beta\beta$ decay of

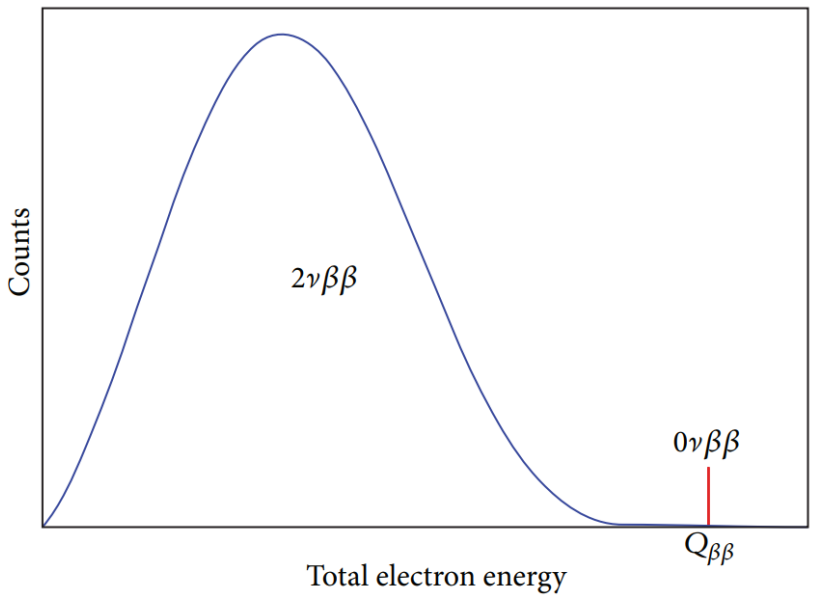

Figure 2.4 The $\beta\beta$ decay spectrum, where the $0\nu\beta\beta$ signal appears as a peak at the location of the $Q_{\beta\beta}$ value, reproduced from [35]. The size of the $0\nu\beta\beta$ peak has been enhanced to be visible.

the isotope used in the search. The expected number of $0\nu\beta\beta$ events in the ROI for a given isotope can be expressed as [36]

$$N = \ln(2)\frac{N_A}{W}\left(\frac{a\varepsilon Mt}{T_{1/2}^{0\nu\beta\beta}}\right), \tag{2.27}$$

where M and W are the mass and molar mass of the $\beta\beta$ emitting isotope, respectively, ε is the detector efficiency in the ROI, N_A is Avogadro's number, a is the isotopic abundance and t is the running time of the experiment, known as the livetime. With the inclusion of background events, the sensitivity to the $0\nu\beta\beta$ half-life can be expressed as [36]

$$T_{1/2}^{0\nu\beta\beta} \propto a\varepsilon\sqrt{\frac{Mt}{B\Delta E}}, \tag{2.28}$$

where B is the background index in units of (keV kg yr)$^{-1}$ and ΔE is the energy resolution. The product Mt is commonly referred to as the exposure, measured in kg yr.

Table 2.2 Commonly used isotopes for direct $0\nu\beta\beta$ decay searches, reproduced from [36].

Isotope	Natural Abundance (%)	$Q_{\beta\beta}$ (MeV)
^{48}Ca	0.187	4.263
^{76}Ge	7.8	2.039
^{82}Se	8.7	2.998
^{96}Zr	2.8	3.348
^{100}Mo	9.8	3.035
^{116}Cd	7.5	2.813
^{130}Te	34.08	2.527
^{136}Xe	8.9	2.459
^{150}Nd	5.6	3.371

There are 35 isotopes that are capable of $\beta\beta$ decay, however only a few of them have characteristics that make them suitable for deployment in a $0\nu\beta\beta$ decay search [36]. From Eq. (2.28) it is evident that an ideal isotope should either have a large natural abundance, or a reasonably priced enrichment process, so that it can be deployed in a large quantity in a high resolution detector with low backgrounds. A high $Q_{\beta\beta}$ value is also preferable to avoid potential sources of background from radioisotopes that may be present in the detector materials. There is no single perfect choice of isotope to optimize all these areas simultaneously, thus different experiment designs choose a smaller set of parameters to optimize instead. Some common choices of isotope are listed in Table 2.2.

The CUORE experiment is currently the largest experiment to search for $0\nu\beta\beta$ decay with a low-temperature calorimeter, also called a bolometer [37]. The detector is a $\sim$1-tonne solid state cryogenic calorimeter formed by 988 TeO_2 crystals operated at $\sim$10 mK, which is used to search for the $0\nu\beta\beta$ decay of ^{130}Te. The ^{130}Te isotope has the highest naturally occurring abundance of 34% and thus does not require further enrichment. The CUORE experiment has so far set a 90% Confidence Interval (CI) lower limit on the $0\nu\beta\beta$ decay

half-life of $T_{1/2}^{0\nu\beta\beta} > 3.2 \times 10^{25}$ yr [37], which corresponds to a median exclusion sensitivity of 1.7×10^{25} yr. CUPID is a planned tonne-scale bolometric experiment with a demonstrator experiment, CUPID-MO, currently in operation [38]. The detector has been developed to readout both scintillation light as well as thermal signals from $Li_2^{100}MoO_4$ crystals. With a dual readout, CUPID will be able to discriminate α background events in the search for the $0\nu\beta\beta$ decay of ^{100}Mo, which CUORE found to be a dominant background [39].

The GERDA and MAJORANA Demonstrator experiments searched for the $0\nu\beta\beta$ decay of ^{76}Ge with high purity Ge detectors [40, 41]. Notably, GERDA has set a strong limit on the $0\nu\beta\beta$ decay half-life of ^{76}Ge of $T_{1/2}^{0\nu\beta\beta} > 1.8 \times 10^{26}$ yr at 90% Confidence Level (CL). Ge detectors can be isotopically enriched to $\sim 90\%$ in ^{76}Ge and have demonstrated excellent energy resolution. The LEGEND experiment plans to combine the techniques developed by GERDA and the MAJORANA Demonstrator in a tonne scale search for $0\nu\beta\beta$ decay in ^{76}Ge [42]. The first phase, LEGEND-200, will use 200 kg Ge submerged in a liquid Ar shield to inform the design of LEGEND-1000 which will use 1000 kg of Ge [43].

This work concerns the search for $0\nu\beta\beta$ decay in the isotope ^{136}Xe, which has many properties that make it competitive in the search for $0\nu\beta\beta$ decay. Moreover, a $0\nu\beta\beta$ search with ^{136}Xe allows for the unique opportunity of Ba-tagging as explained in the following Chapter.

Chapter 3

Searching for $0\nu\beta\beta$ in ^{136}Xe

There are multiple factors that make ^{136}Xe a suitable candidate for observing $0\nu\beta\beta$ decay. The β decay mode is suppressed in this even-even nucleus, and the $Q_{\beta\beta}$ value is high enough to be above the Q values of many natural radioactive decays. It has a naturally occurring abundance of 8.9%, but can be enriched to 80% or higher with centrifuge techniques in large quantities, making the enrichment process easier than that of a solid state isotope like ^{76}Ge [44]. Since Xe is an excellent ionization detection medium, it can function as both the source of the decay as well as the detector. Energy deposits in Xe also produce an abundance of scintillation light [45], which is strongly anti-correlated with the produced ionization charge [46]. A detector such as a Time Projection Chamber (TPC) can use ionization and scintillation signals to reconstruct the event energy, topology and position. Moreover the ratio of ionization to scintillation signal can be used to discriminate against backgrounds such as alpha particles, which have low ionization compared to scintillation, as well as γ rays, which produce more ionization than scintillation [36].

Since Xe has a relatively high Z value of 54, a 2.5 MeV γ will have an attenuation length of ~ 9 cm in liquid Xe (LXe) [47], which makes it possible to achieve very low backgrounds within a fiducial volume. This self-shielding effect can be maximised by the construction of monolithic LXe detectors. Lastly, the $\beta\beta$ decay of ^{136}Xe produces ^{136}Ba, a stable isotope,

which allows for the unique opportunity of extracting the decay daughter from the detector volume and identifying in a process called Barium-tagging.

3.1 The EXO-200 Experiment

The EXO-200 collaboration searched for $0\nu\beta\beta$ decay in LXe, enriched to 80.6% in ^{136}Xe, from 2011 to 2018 at the Waste Isolation Pilot Plant (WIPP) in New Mexico USA. The LXe was deployed in a TPC that was split in half by a negatively biased semi-transparent common cathode, as shown in Fig. 3.1. Each half of the TPC had a drift length of $\sim$20 cm and radius of $\sim$18 cm, and the walls of the TPC were made from thin radio-pure copper. Wire planes at each end of the TPC served to collect ionization charge, which drifted under the electric field created by the cathode and field shaping rings. Scintillation light was collected by large area avalanche photo-diodes (LAAPDs) positioned behind the wire planes. The cathode was 90% transparent to scintillation light which was detected at both ends of the TPC [48]. The ionization charge on the other hand was only detected in the TPC half it was produced in. The wire planes consisted of separate "U" and "V" wires that had a relative angle of 60°.

The V plane was in front of the U plane and biased in such a way that it was transparent to passing electrons. The charge deposition and induction in the U and V planes, respectively, allowed for the reconstruction of two of the event coordinates. After being recorded as U and V coordinates they were then converted to X and Y. The third coordinate was reconstructed with the time difference between the arrival of scintillation light and ionization charge. There was a gap of 6 mm between the U and V planes and also between the V plane and LAAPD layer. Events within the fiducial volume (FV) were required to lie within a hexagon in the X and Y plane with an apothem of 162 mm, as well as be more than 10 mm away from the cathode and V-wire planes. The total mass of ^{136}Xe contained within the FV was 74.7 kg [49].

Plastic-scintillator veto panels surrounded the experiment on all sides, allowing for the detection of passing muons, which helped to mitigate the backgrounds they created. The

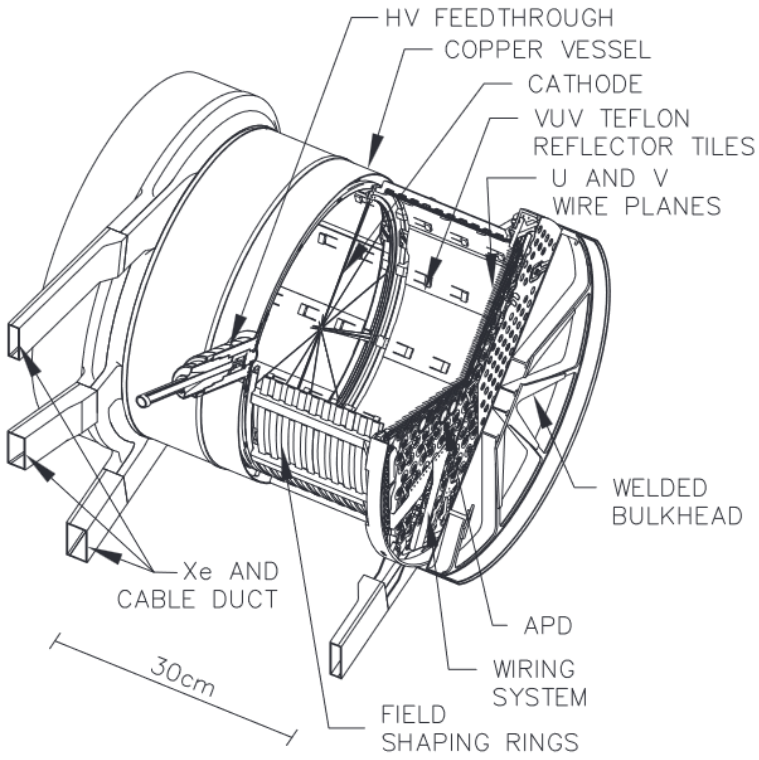

Figure 3.1 Schematic of the EXO-200 detector, reproduced from [48].

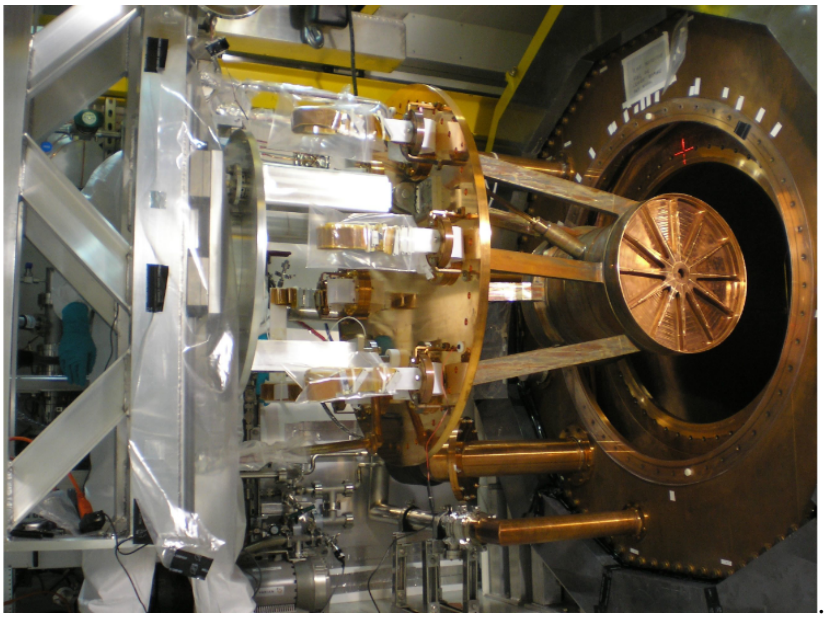

Figure 3.2 The EXO-200 detector mounted on an installation jig, reproduced from [48].

muon flux was greatly reduced by the 1624^{+22}_{-21} m of water equivalent overburden shielding [50]. The TPC was submerged in HFE-7000 cryofluid which was maintained at 167 K inside a vacuum insulated cryostat. Both the TPC and cryostat are shown in Fig. 3.2. The cryofluid provided 50 cm of shielding from environmental radioactivity, and an additional 25 cm of lead surrounded the cryostat in all directions.

Events in the TPC can be reconstructed as having energy deposited in either a single location, or multiple locations, referred to as single-site (SS) and multi-site (MS) events, respectively. The events produced by $0\nu\beta\beta$ decay are predominantly SS, whereas MS events are typically γ backgrounds. Probability density functions (pdfs) were created for the expected SS and MS spectra using GEANT4 simulations to model the detector response [51]. The charge depositions were transported to the U-V wire assemblies, where a signal was generated with a model of the electronics. The pdfs were broadened with the resolution function and their normalizations were obtained with a fit to the data. Once all of the expected backgrounds had been generated, the combined pdf was then fitted to low background data, as shown in Fig. 3.3.

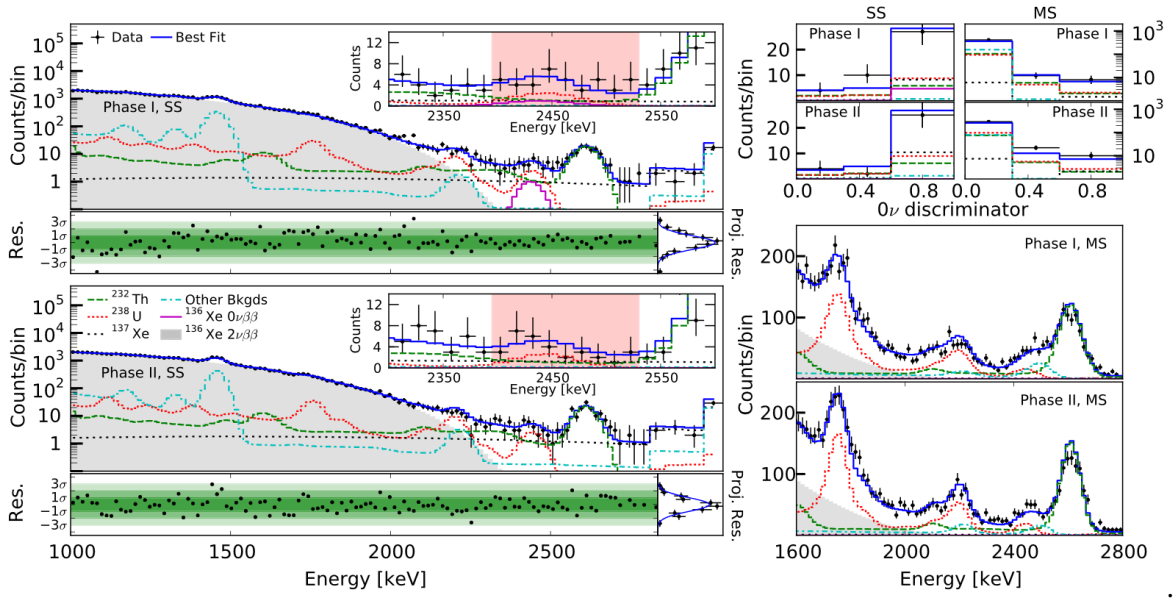

Figure 3.3 Best fits to the SS energy spectrum for low background data, reproduced from [49].

There were two phases of data taking during the period of operation. In Phase-I, which took place from 2011 to Feb 2014, an electric field of 380 V/cm was used which was produced by an -8 kV bias on the cathode. In Phase-II, the electronics were upgraded and an electric field of 567 V/cm, produced by a -12 kV bias on the cathode, was used to improve the energy resolution [49]. Both Phase-I+II data were blinded to mask candidate $0\nu\beta\beta$ events. To calibrate the detector energy scale, the sources ^{60}Co, ^{228}Th and ^{226}Ra were regularly positioned 9-11 cm from the LXe in calibration runs. The 2D energy spectra of anti-correlated charge and light signals were rotated and projected onto a 1D energy variable, in a way that minimized the energy resolution at the $0\nu\beta\beta$ decay energy of $Q_{\beta\beta}$=2457.83 $\pm$ 0.37 keV [52]. The average detector resolution was determined by calibration runs as $\sigma/Q_{\beta\beta} = 1.35 \pm 0.09\%$ and $1.15 \pm 0.02\%$ for Phase-I and Phase-II respectively.

In the most recent $0\nu\beta\beta$ search both Phase-I+II have been unblinded and fit using a Maximum Likelihood (ML) method. As of yet no statistically significant evidence for $0\nu\beta\beta$ decay has been observed. The total exposure for the experiment was 234.1 kg yr, and a lower limit on the half-life of $0\nu\beta\beta$ of was set at $T_{1/2} > 3.5 \times 10^{25}$ yr at 90% CL [49]. This half-life

corresponds to an upper limit on the Majorana neutrino mass of $m_{\beta\beta} < 93 - 206$ MeV, and a 90% CL sensitivity to $0\nu\beta\beta$ decay of 5.0×10^{25} yr. These results remain competitive with the results of other $0\nu\beta\beta$ decay searches such as CUORE or GERDA, as discussed in the previous chapter. The next generation of $0\nu\beta\beta$ decay experiments are designed to reach a sensitivity to $0\nu\beta\beta$ on the order of $10^{27} - 10^{28}$ yr, by increasing the mass of the isotope of interest into the tonne-scale.

3.2 The nEXO Experiment

The nEXO experiment is a planned successor to the EXO-200 experiment, that will use 5 tonnes of LXe enriched to 90% in ^{136}Xe. The nEXO TPC will be a right cylinder, with an inner height and diameter equal to 127.7 cm, surrounded by 33000 kg of HFE-7000 cryofluid. The cryofluid is contained within the inner vessel (IV), which is vacuum insulated from an outer-vessel (OV) as shown in Fig. 3.4. The OV is submerged within a large tank of water that provides additional shielding and acts as a muon veto, called the outer detector (OD). The IV is modelled as a sphere with a diameter of 338 cm, and the OV is likewise modelled as a sphere with a diameter of 446 cm [6].

Unlike the EXO-200 design, there is no central cathode planned for the nEXO TPC. This is to avoid the introduction of radioactivity into the centre of the TPC, to take full advantage of the LXe “self-shielding" effect. The walls of the TPC will be lined with high-purity copper field shaping rings that will provide a uniform electric drift field of about 400 V/cm. Silicon photomultipliers will be placed behind the field shaping rings and mounted onto the barrel of the TPC, and will be used to collect the scintillation light. The ionization charge is to be collected by arrays of 10x10 cm^2 dielectric tiles, which will be positioned at the top of the TPC. It is expected that a readout ASIC chip will be mounted on the reverse side of the tiles to measure the ionization charge [53].

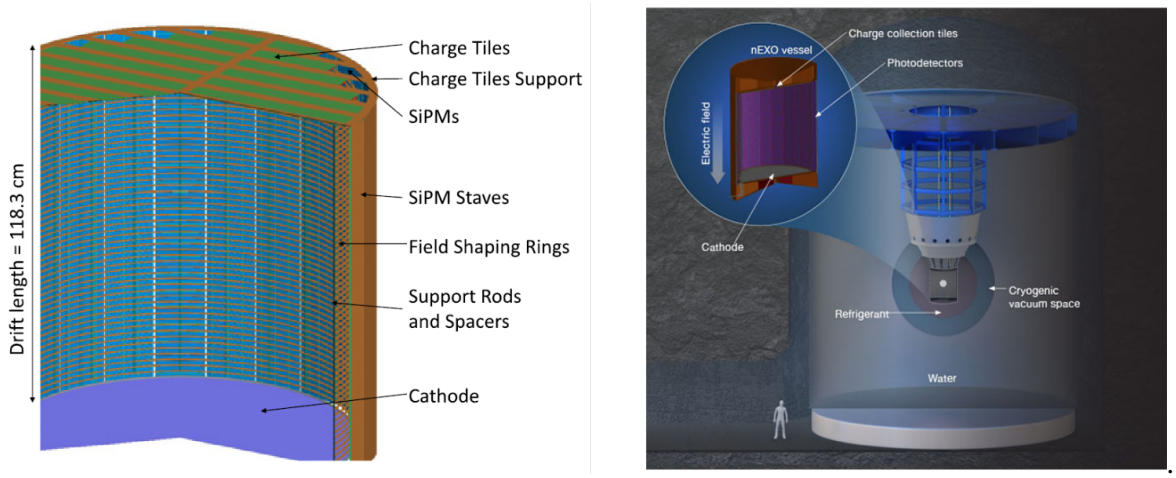

Figure 3.4 (left) Detailed view of the nEXO TPC, reproduced from [6]. (right) Anticipated installation of nEXO in the cryopit at SNOLAB.

A background model has been constructed using radioassay data as well as a comprehensive list of all expected background sources. Of primary interest are backgrounds from long-lived radionuclides like ^{238}U, which has a decay chain that produces a 2448 keV γ ray from the decay of ^{214}Bi. As well as ^{232}Th which produces a 2615 keV γ ray from ^{208}Ti decay. Backgrounds can also arise from the exposure of detector components to cosmogenic radiation. Notably, the production of neutrons from muon spallation will result in the production of ^{137}Xe from neutron capture on ^{136}Xe. ^{137}Xe is created in an excited state with an energy of 4025 keV and promptly de-excites, releasing γ's with a total energy in the range 600-4025 keV[50]. Since the release of γ's is prompt, they are rejected by the muon veto. However, ^{137}Xe undergoes β decay with a relatively long half-life of 3.82 minutes [54], with an endpoint energy of 4173 keV. Thus the β decay spectrum overlaps with the ROI for $0\nu\beta\beta$. The contributions from ^{137}Xe has been studied using GEANT4 MC simulations, and a veto has been developed to reject ^{137}Xe decays with $> 70\%$ efficiency without significantly decreasing the livetime [6].

The sensitivity and discovery potential of nEXO has been determined with simulated trial experiments [53]. If no signal is observed in 10 years of exposure, nEXO will place a lower bound on the $0\nu\beta\beta$ decay half life of $T_{1/2}^{0\nu\beta\beta} > 1.35 \times 10^{28}$ years at 90% CL [6]. A plot

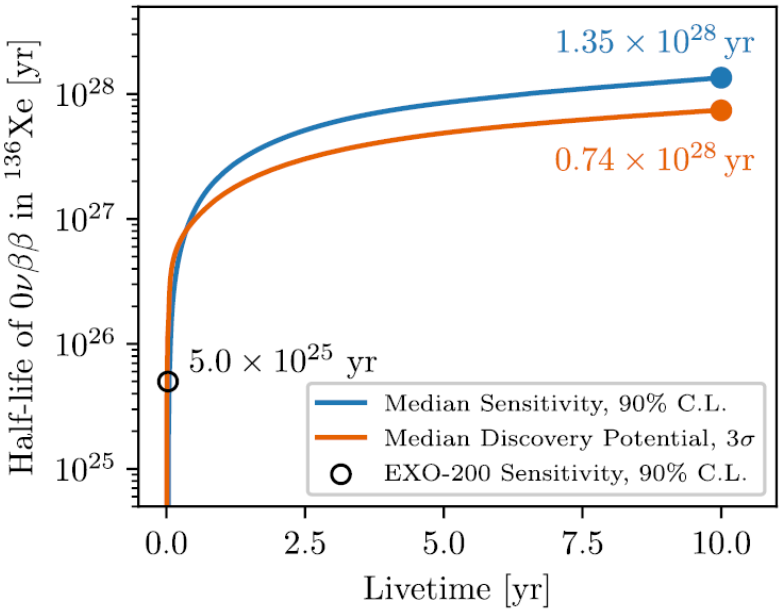

Figure 3.5 The median sensitivity and 3σ discovery potential of nEXO as a function of livetime, reproduced from [6] .

of the median sensitivity vs. livetime is shown in Fig. 3.5. Assuming that $0\nu\beta\beta$ decay is mediated by light Majorana neutrino exchange, Eq. (2.26) can be used to convert the sensitivity to the half-life of $0\nu\beta\beta$ decay into a coverage region for $\langle m_{\beta\beta}\rangle$. A plot of the exclusion sensitivity to $\langle m_{\beta\beta}\rangle$ is shown in Fig. 3.6 as a function of the lightest neutrino mass, where the allowed neutrino mass bands are derived from neutrino oscillation parameters [55]. The nEXO experiment will fully cover the IH region, as well as a significant portion of the NH. It is possible to improve the sensitivity of nEXO either by creating a larger detector or by reducing backgrounds to the $0\nu\beta\beta$ decay search. This work will focus on the background suppression technique called Ba-tagging.

As $0\nu\beta\beta$ decay experiments move towards the tonne-scale, isotope procurement becomes a dominant experimental cost. Thus it becomes imperative to manage the isotope efficiently by reducing backgrounds as much as possible. In the case of ^{136}Xe, the $\beta\beta$ decay process produces a Ba^{++} ion which is expected to reduce to Ba^{+} in LXe. This presents a unique opportunity; since the daughter ion is stable it can be located within a small volume, extracted from the detector volume and identified. If done successfully, it would allow for a background

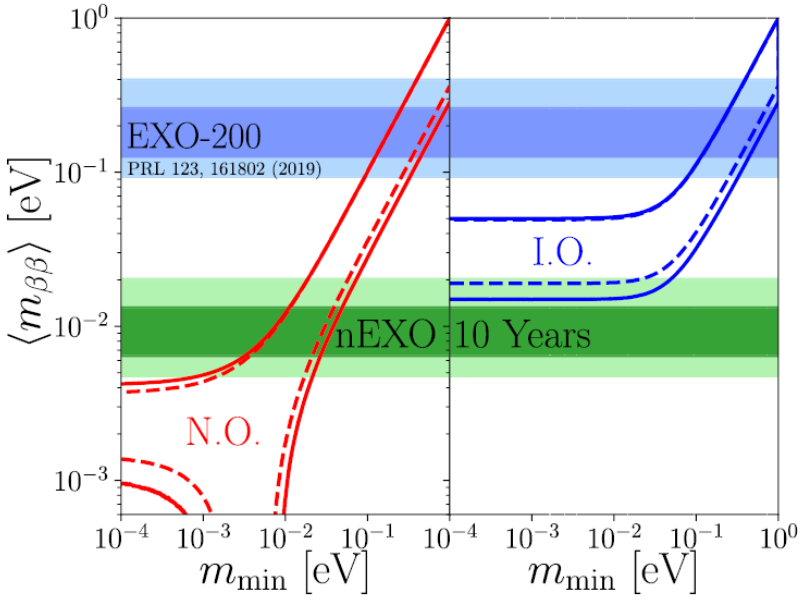

Figure 3.6 The 90% confidence level exclusion sensitivity to the effective Majorana neutrino mass, reproduced from [6].

free and unambiguous measurement of $\beta\beta$ decay in ^{136}Xe. Thus, reliable extraction and transport to the tagging apparatus is required for the final Ba-tagging process.

If the Ba-tagging system is 100% efficient, and the only background to the $0\nu\beta\beta$ decay search is $2\nu\beta\beta$, the sensitivity of nEXO to the $0\nu\beta\beta$ half-life will reach $T_{1/2} \sim 4 \times 10^{28}$ yr, resulting in a factor 2-3 increase from the scenario with no Ba-tagging [53]. Therefore the tagging process can significantly boost the experiment's sensitivity and furthermore serve as a direct verification of the $0\nu\beta\beta$ signal as being a true $\beta\beta$ decay.

3.3 Ba-tagging in the US

One method of extracting the Ba ion, which is being researched at Colorado State University (CSU), is to move a cold probe near the reconstructed $\beta\beta$ decay candidate event location and freeze some of the surrounding LXe onto it. With the Ba ion trapped in a solid Xe matrix, it can be removed from the TPC and tagged through laser fluorescence imaging. The imaging

of individual Ba ions in solid Xe has been demonstrated at CSU [56].

Another method, which was developed at Stanford University, is to electrostatically drift the Ba ion onto a substrate mounted on a probe [57]. The probe is then used to transport the Ba atom to a vacuum environment, where it can be removed with laser induced thermal desorption, re-ionized and then identified by resonance ionization spectroscopy.

A group at the University of Texas in Arlington has adapted the technique of single molecule fluorescence imaging for Ba-tagging [58]. This is to be used by the NEXT collaboration, a competing collaboration, which plans to search for $0\nu\beta\beta$ decay using a high-pressure Xe gas TPC [59]. The Ba ion will be drifted to the cathode, where it will be levitated by an RF carpet to a single molecule flourescent imaging plane for identification [60].

3.4 Ba-tagging in Canada

A candidate $0\nu\beta\beta$ event in the nEXO liquid TPC can be localised with a characteristic dimension of a few mm [6], with an expected ion fraction $> 76\%$ [61]. In a potential Ba-tagging scenario, the volume surrounding the decay daughter is extracted with a capillary in which the phase changes from liquid to gas. Laminar flow within the capillary will prevent the ion from hitting the wall of the capillary and neutralizing. The ions extracted from the TPC are then separated from neutral Xe gas with a radio frequency ion-funnel (RF funnel) [62]. They are then cooled and bunched with a Linear Paul Trap (LPT), in which the Ba ion is identified with laser spectroscopy. Ion bunches are ejected from the LPT into a MRTOF for further analysis. The concept of the Ba-tagging setup is shown in Fig. 3.7.

Different parts of this Barium tagging system are currently under development at multiple Canadian institutions. The extraction capillary, that will convert LXe to GXe, is being developed by a group at Carleton University. The RF-only ion Funnel was originally developed at Stanford to transport ions from a high-pressure gas of up to 10 bar, to high-vacuum with high

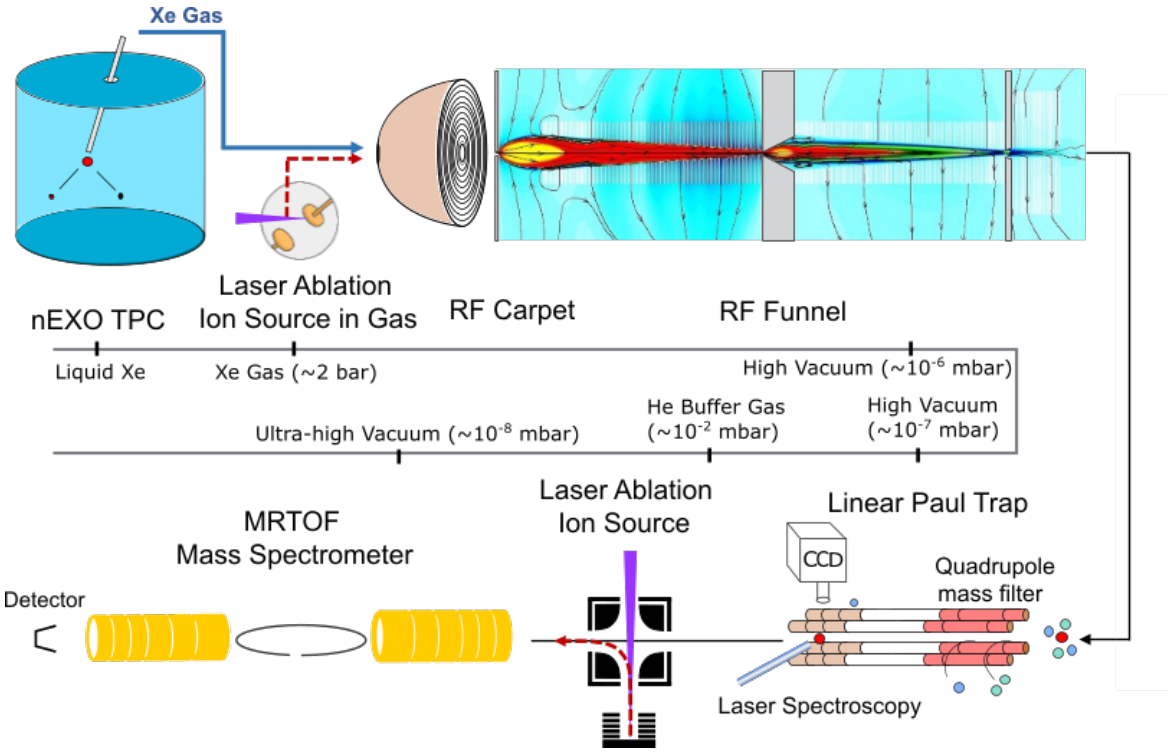

Figure 3.7 Schematic of the ba-tagging system in development at institutions across Canada.

efficiency. The RF Funnel achieves this by transporting ions with carrier gas flow instead of DC drag potentials [62]. Ion transport from a high pressure gas has been demonstrated, and the setup has since been relocated to McGill where it is currently being recommissioned. An LPT was designed at TRIUMF, that can perform laser fluorescence spectroscopy for identification of the Ba ion, and also bunch and eject ions into an MRTOF for further identification [63]. The LPT has been assembled at McGill and is currently being commissioned. The identification of single Ba ions using laser fluorescence spectroscopy has been demonstrated previously at Stanford [64], and is being developed further by the Carleton group [65].

Ion sources are needed for the commissioning and calibration of the devices in the Ba-tagging system as shown in Fig. 3.7. A LAS is a versatile ion source that can produce diverse ion species in either vacuum or gas, making it ideal for the Ba-tagging system. Moreover a LAS that uses a pulsed laser can produce ion bunches with a localised time structure, which can be

cooled and bunched in the LPT, or coupled to the MRTOF directly. In the following chapter, the development of a LAS for Ba-tagging is discussed.

Chapter 4

The spatially-resolved multi-element laser ablation ion source

This chapter concerns the development of a Laser Ablation Ion Source (LAS) that can selectively ablate different elements from a multi-element target. The technique was developed and tested with a prototype setup which is discussed in the work to follow. A second LAS with minor modifications was later built to commission the MRTOF, which is discussed in Chapter 7.

The use of lasers to produce ion beams, whether by resonance ionisation or ablation, is common in various applications, see e.g. [57][66–73]. Ions may be produced in vacuum, or at higher pressures up to $\sim$1 bar in the presence of different species of ambient gases [74]. Since the process of ablation is inherently destructive, it is typically necessary to shift the laser spot position on a target as the target surface degrades. Moreover, it may be desirable to selectively ablate specific areas of a multi-element target for applications such as mass spectrometer calibration. In high-precision mass-spectrometry applications, the positioning of a laser beam on the target surface is typically achieved by mounting the target onto a rotating wheel or $x-y$ translation stage [75–82]. In a recent development, the laser spot position was randomised by the movement of an external focusing lens which was mounted onto an $x-y$ translation stage [83]. An alternative method, presented here, is to shift the

laser spot position on the target with the final reflection into the vacuum chamber, using a high-precision motorized kinematic mirror mount.

The LAS uses a pulsed UV laser to produce ion bunches from a custom target in an Ultra-High Vacuum (UHV) system. For ablation to occur, an incident laser spot fluence of approximately $0.1 - 10$ J/cm^2 is required [84–88]. Target materials are chosen such that they span a large mass range for the purposes of mass-spectrometer calibration. For the characterization of the LAS the resulting ion bunches are guided by a quadrupole bender to a Faraday cup, instead of to a mass spectrometer, where the ion current is measured. A 2D image of the target can be reproduced by rastering the ablation laser spot across the surface of the target and recording the resulting ion current at each location. Since the ablation yield is material dependent [89], the measured ion current changes for different materials, thus it is possible to distinguish physical features of the target. The resolution of physical features of the target allows for the establishment of a coordinate system on the target surface, which can be used to selectively ablate different materials. This work characterizes the spatial resolution with which the LAS may selectively ablate the surface of a target to produce ions for the Ba-tagging system.

4.1 Experimental Setup

The LAS consists of a vacuum chamber where the ions are produced and measured, attached to an optical breadboard where the laser beam optics are located. The vacuum chamber is a 6-way DN160 CF cross, which houses the ion-source assembly, a 90° DC quadrupole deflector and a Faraday cup. UHV conditions are achieved by a turbomolecular pump attached to the bottom flange of the cross. The pressure is monitored with a cold cathode gauge, and is typically in the range of 1×10^{-8} to 1×10^{-9} Torr. A schematic drawing of the setup is shown in Fig. 4.1.

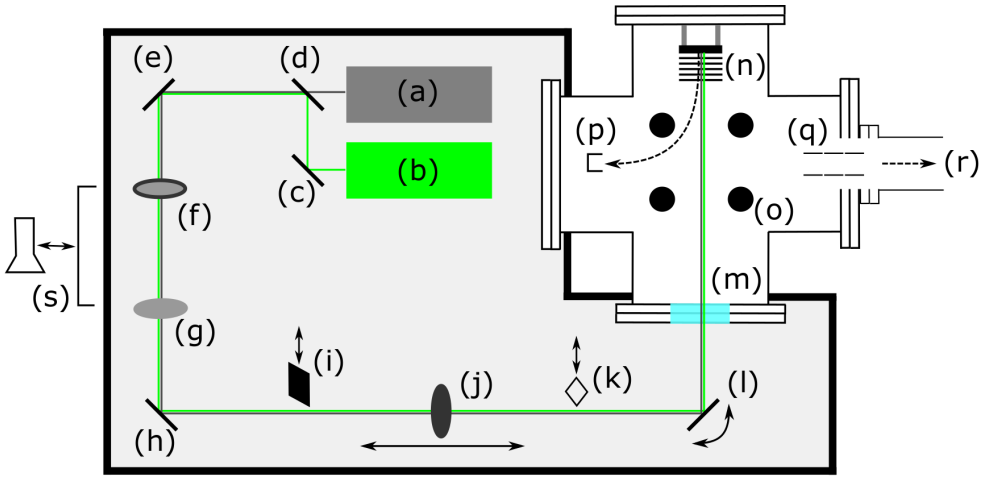

Figure 4.1 Schematic of the LAS layout. The optical components guide a 349 nm Nd:YLF UV laser (a), and a 532 nm green laser (b), into a 6-way CF cross. These lasers are for ablation and alignment purposes, respectively, and a flip mirror (d) is used to toggle between both beams. The laser light is reflected by a series of UV enhanced aluminium mirrors (c)(e)(h), and passes through a pair of diverging (f) and converging (g) lenses. The beam is then focused onto a target with a f = 750 mm UVFS plano-convex lens (j), which is mounted onto a motorized stage parallel to the optical axis. A knife-edge (i) and power meter (k) are used to measure the laser beam profile and energy. The beam is reflected onto the target by a UV-enhanced mirror mounted in a motorized kinematic mirror mount (l), which allows for precise manipulation of the laser spot on the target. The laser beam enters into the vacuum chamber through a UV transparent window (m), to strike the target (n). Once ions are produced from the target, they are accelerated by a series of ring electrodes. The ions then pass through a 90° quadrupole bender (o), to either a Faraday cup (p), or through an einzel lens (q) to another device such as a mass spectrometer. For measurements of ion transport efficiency, the diverging and converging lenses were replaced with a Thorlabs BE10-UVB beam expander (s).

4.1.1 Optical Setup for Laser Scanning

Ions are produced by a pulsed 349 nm neodymium-doped yttrium lithium fluoride (Nd:YLF) UV Spectra Physics Explorer 349 120. A series of mirrors and lenses focus the laser beam into the vacuum chamber. The UV laser can be pulsed with a variable repetition rate ranging from 1 Hz to 5 kHz, with a nominal energy of 120 μJ per pulse, and a pulse width < 5 ns [90]. A visible laser is included in the setup to ease the alignment process.

The UV laser beam is focused onto the target by a plano-convex lens with a 750 mm focal length, which is mounted onto a motorized stage oriented parallel to the beam path, so that the location of the focal plane may be remotely adjusted to optimize ablation at the target surface. After passing through the focusing lens, the laser beam is reflected into the chamber and onto the target by a mirror on a computer-controlled motorized mount. Motorised mirror mounts are used to selectively ablate materials off of a fixed target (Fig. 4.1 (l)). Two different motorized mirror mounts were used in this study. The first is a KS1-Z8 mount from Thorlabs with Z-812 series DC motor actuators. The second is a Physik Instrumente (PI) mount with N-472 linear actuators and E-871 servo controllers. The Thorlabs mount has a travel range of 12 mm, a minimum incremental movement of 0.2 μm, and a bidirectional repeatability of < 1.5 μm. The PI mirror has a travel range of 13 mm, a minimum incremental movement of 0.05 μm, and a unidirectional repeatability of 0.2 μm.

The mirror motors are controlled by a LabVIEW program that steps the laser spot in a rasterized grid across the target's surface, while recording the ion current measured at each point in the grid with the Faraday cup (Fig. 4.1 (p)). In this manner, one and two dimensional scans of a target may be produced.

4.1.2 Ion Source Assembly and Ion Optics

The ion-source assembly, shown in Fig. 4.2, enables the mounting of custom targets in a stainless steel target-holder. Ions produced by ablation are accelerated by a series of five

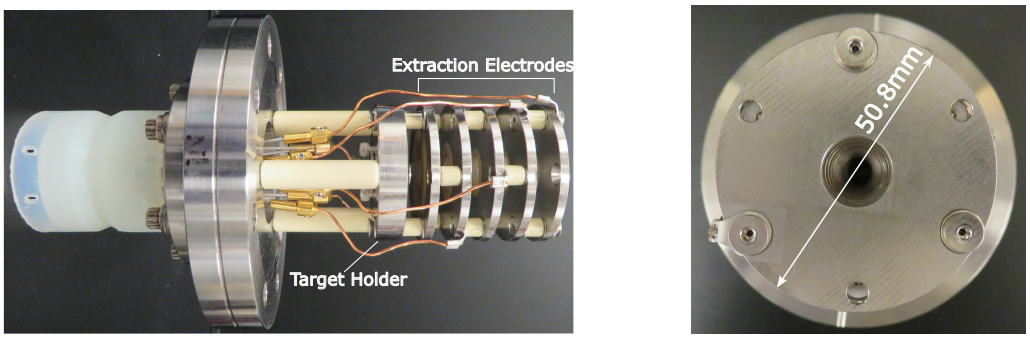

Figure 4.2 Photograph of the ion-source assembly with a view from the side (left) and from the front (right). The ion source consists of a stainless steel target-holder, which is followed by 5 electrodes that create an accelerating DC field. The target-holder and electrodes have an outer-diameter of 50.8 mm, an inter-electrode spacing of 6.4 mm, and an inner diameter of 12.7 mm. The assembly is mounted onto a DN40 CF flange with ceramic standoffs.

extraction electrodes, after which they are deflected by a 90° quadrupole bender to either a Faraday cup or another device such as a mass spectrometer. For the measurements presented in this chapter, the mass spectrometer had not been operational and all results presented here were measured with the Faraday cup. The 90° quadrupole bender is formed by 25.4 mm diameter stainless steel rods, which form a square with a center-to-center spacing of 59.1 mm between adjacent rods. The quadrupole bender's widely spaced electrodes allow surface scans over ranges as large as 50 mm in width.

DC potentials are applied to the ion source, quadrupole bender and Faraday cup with Rohde and Schwarz HMC804 power supplies, which can output up to 32V per channel. The ion current produced by the ion source is typically measured with an Agilent 34465A digital multimeter connected to the Faraday cup. For direct measurement of the ion transport efficiency through the ion-source assembly and the quadrupole bender, the ion currents leaving the target and arriving at the Faraday cup were measured simultaneously using two Keithley 6485 picoammeters. For measurement of the ion transport efficiency, the LAS had been upgraded by replacing the diverging and converging lenses with a Thorlabs BE10-UVB beam expander to reduce the laser spot diameter on the target by a factor of 2. A cylindrical Cu only target was used to investigate the homogeneity of the ion transport efficiency across the

target surface with a 2D scan.

4.2 Target Scanning in 2D

The actuated mirror moves the laser beam in two directions across the target surface. The directions of movement are to first order perpendicular to each other. The system is calibrated so that the distance actuated by the mirror stages in units of mm can be converted to distance travelled on the target surface. The inner diameter of the stainless steel target holder is used as a reference to construct the target coordinate system from a 2D scan of the target. This coordinate system can be described simply with the following transformation

$$(x', y') = (S_x x, S_y y), \tag{4.1}$$

where (x,y) are the coordinates of the mirror stages, (S_x,S_y) are scaling factors, and (x',y') are the target coordinates.

A multi-element target consisting of gold, niobium and copper (Au-Nb-Cu) was scanned in 2D by the LAS. Scans of the Au-Nb-Cu target are used here to demonstrate a measurement of the scaling factors described by Eq. (4.1). The Au-Nb-Cu target is formed by a hollow niobium cylinder, with a rectangular copper rod in its centre held in place by stainless steel set screws. A 0.1 mm thick piece of gold foil covers one half of the niobium face. The target is shown mounted into the target holder in Fig. 4.3. These metals are ideal for the calibration of a mass-spectrometer for Ba-tagging, since Nb and Au have single stable isotopes that are lighter and heavier than Ba, respectively, with Cu providing two stable isotopes in the light mass region.

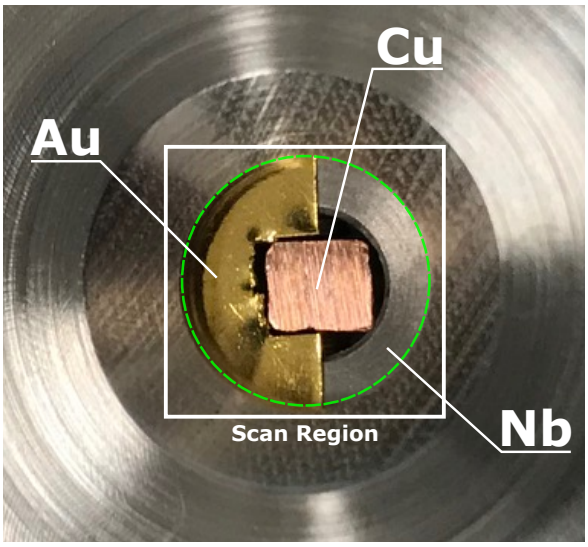

Figure 4.3 A photograph of the Au-Nb-Cu target in a stainless steel holder that forms the base of the ion source. The inner diameter of the holder, indicated by the dashed green circle, is 7.8(1) mm, which is used as a reference dimension when calibrating the laser spot motion on the target.

4.2.1 Determination of Scaling Factors

The scaling factors were calculated for each mirror, by creating a 2D scan of the target and fitting an ellipse to the diameter of the target holder. Two examples are shown in Fig. 4.4 for the PI and Thorlabs mirror mounts on the top and bottom respectively. The ellipse was fit to a total of 30 points which were selected manually at the interface of the target and the target holder. The diameter of the target holder was measured as D_{TH} = 7.8(1) mm, S_x and S_y were calculated as the ratio of D_{TH} with the best-fit values for the semi-minor and semi-major axes respectively. The measured scaling factors for both mirrors are summarized in Table 4.1, where the smallest step size on the target surface for each mirror is also presented. As will be discussed in Section 4.3, the spatial resolution of this LAS is limited by the diameter of the laser spot on the target, and not the smallest step size. Thus, both mirror mounts are able to reconstruct the physical features of the target with similar performance. Small differences in the mean ion current between the two shown scans are not caused by the use of different motorized mirror mounts, but by slight differences in the optical setup, as the scans presented here were taken at different stages of the development of the technique. Additionally, the

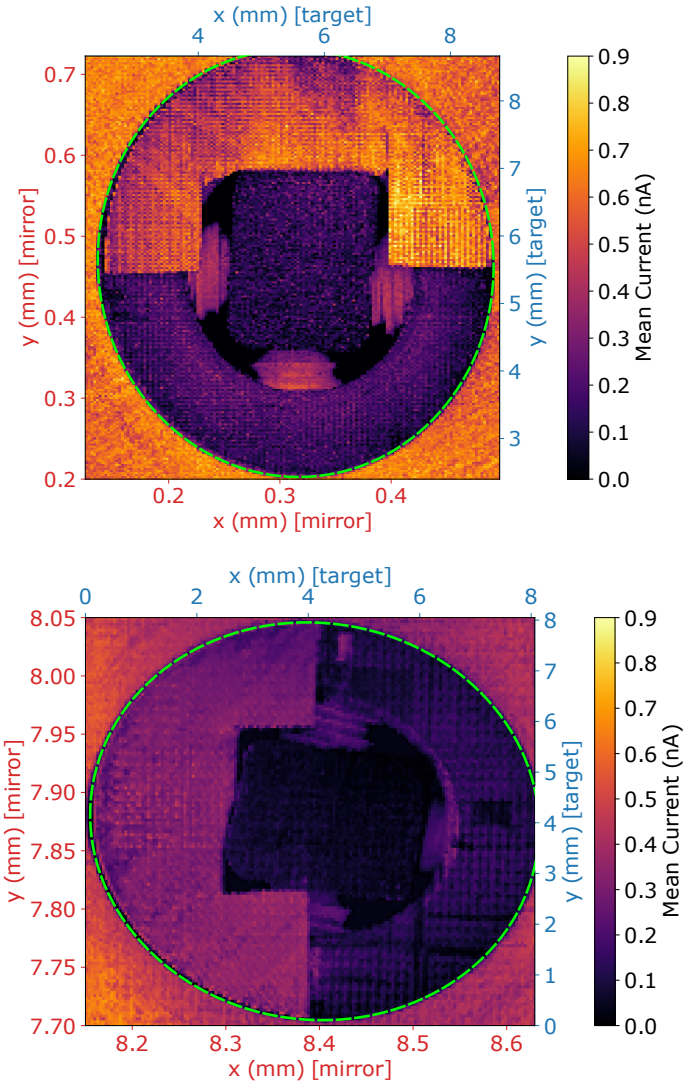

Figure 4.4 A position dependent 2D reconstruction of the ion current ablated from the target surface, using the PI (top) and Thorlabs (bottom) kinematic mirror mounts to adjust the laser spot position, where the colorbar indicates the ion current measured by the Faraday cup. The scaling factors used to convert to target coordinates are obtained by fitting an ellipse to the inner diameter of the target holder, which is marked in each image by a green dashed line, and comparing this to the physically measured value of 7.8(1) mm. The target was physically rotated by 90° counterclockwise between top and bottom scan image and the gold foil had been replaced. The orientation of metals in Fig. 4.4 is identical to the orientation indicated in Fig. 4.3.

Table 4.1 The measured scaling factors for x and y for the PI and Thorlabs actuated mirrors, obtained through the fit of an ellipse as demonstrated in Fig. 4.4.

	Scaling Factor		Smallest Step Size	
Mirror Mount	S_x	S_y	$x_{\min}(\mu\text{m})$	$y_{\min}(\mu\text{m})$
TL KS1-Z8	19.2(3)	13.9(2)	3.84(6)	2.78(4)
PI N472	21.8(3)	14.9(2)	1.09(2)	0.75(1)

surface of the target was scanned repeatedly over the development period, and differences in the amount of damage accumulated on the target surface could result in differences in the measured ion current.

The large spacing between the quadrupole electrodes allows for scanning over ranges as large as 50 mm. To demonstrate this, the focusing lens, which is mounted onto a motorized stage, was adjusted so that the laser beam was focused on the surface of the final accelerating electrode. A reconstructed 2D current map from a scan of the full electrode is shown on top in Fig. 4.5. By fitting an ellipse to the inner diameter, the scaling factors were measured in this focal plane as S_x=19.0(3) and S_y=12.8(2) for the PI mirror. The scan of the full electrode was taken over the period of a day with step sizes of 475(8) μm and 320(5) μm in x and y respectively. A detailed scan of one of the screws securing the electrode is shown at the bottom of Fig. 4.5 with a 10-fold smaller step size. Clearly visible is the feature of the venting hole in the screw center, which has a diameter of 1.0(1) mm. The scaling factors were found to remain consistent between measurements, but the system needs to be re-calibrated following changes to the optical setup.

4.2.2 Measurement of the Laser Spot Step Size

An optical microscope was used to visually measure the distance between ablated spots in order to confirm that the scaling factors accurately predict the laser spot step size on the target surface. A thin Cu foil was scanned over the full target range using the PI mirror mount, with a laser beam energy of 18.1(2) μJ per pulse at 500 Hz and a fixed step size of 20 μm in

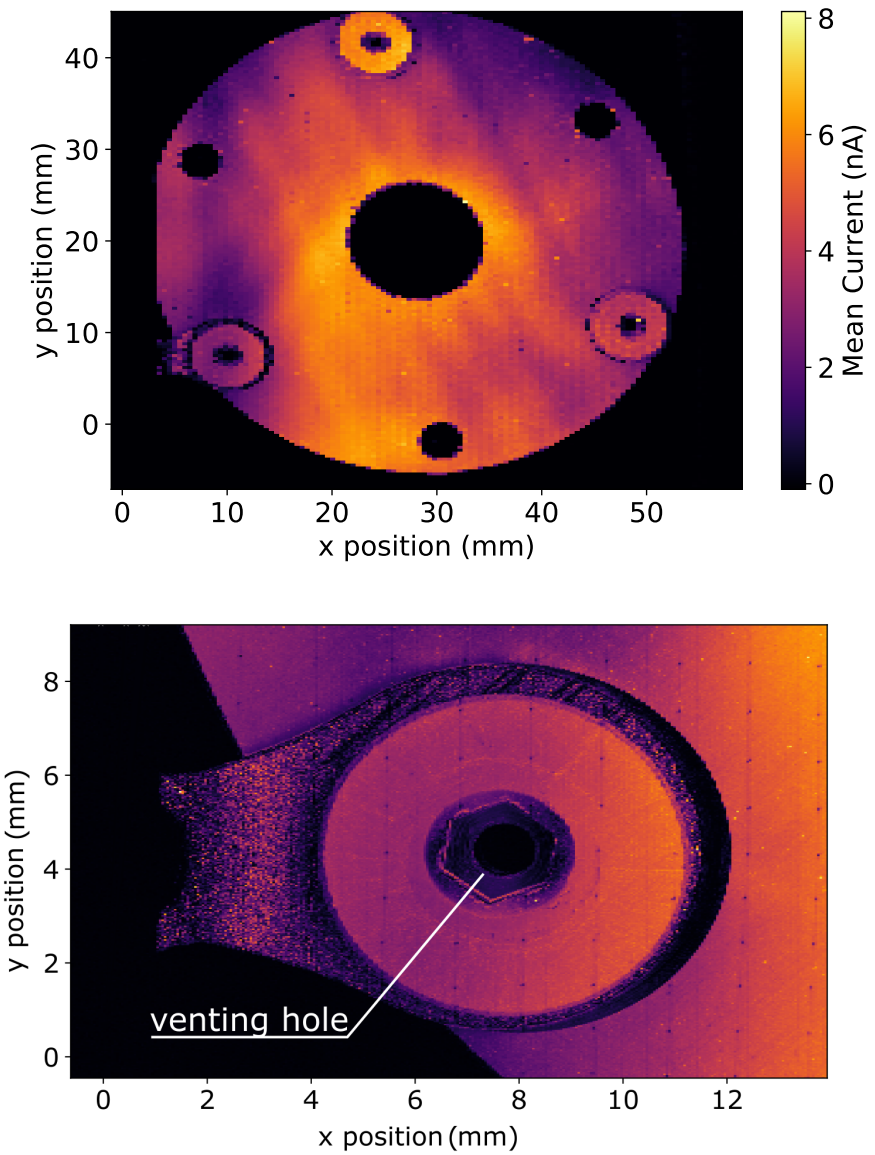

Figure 4.5 (top) A 2D current map of a scan of the final electrode of the ion-source assembly, where the colorbar indicates the ion current measured on the Faraday cup. A mirror step size of 25 μm in both the x and y directions was used, which corresponds to step size on the target of 475(8) μm and 320(5) μm respectively. (bottom) A detailed current map of a scan of a socket-head screw used to secure the electrode, where the mirror step size is a factor of 10 smaller. The dark circle is the hole of the center-vented screw.

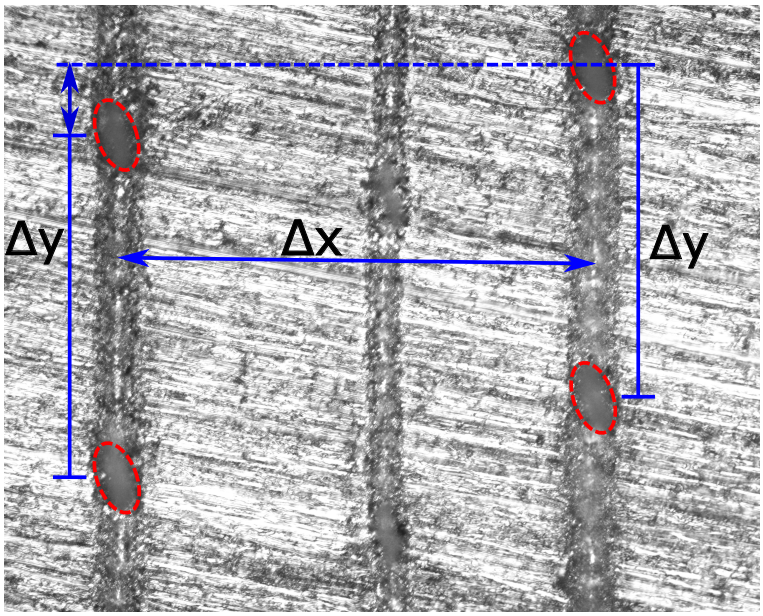

Figure 4.6 Image of ablation craters and tracks on the surface of a Cu foil recorded with an optical microscope at ×20 magnification. The distances in x and y between adjacent ablation craters, denoted by red-dashed lines, were measured as Δx = 441.6(6) μm and Δy = 305.1(9) μm respectively. The thinner track in the center was formed by a different scan with a laser beam energy of 18.1(2) μJ per pulse and is not relevant to the presented step-size measurements.

mirror coordinates in both the x and y directions. Since the laser emitted pulses while the spot was being moved on the target surface, there were ablation craters as well as tracks that connect them. To include scans at a different laser beam energy, two opposite quarters of the target were scanned a second time with higher laser beam energies of 28.8(3) μJ and 36.1(6) μJ per pulse. It was found that the size of craters and tracks created by 28.8(3) μJ and 36.1(6) μJ laser pulses were indistinguishable under the microscope, but distinguishable from craters and tracks formed by 18.1(2) μJ pulses.

The average x and y distances between the centre positions of 4 elliptical ablation craters, which are indicated with red dashed lines in Fig. 4.6, were measured at ×20 magnification with an optical microscope. The ablation craters are elliptical in shape, with the average of the four major and minor axes measured as 68(5) μm and 39(2) μm respectively. The distance in x between ablation points was measured as Δx = 441.6(6) μm, and the distance

in y was measured as Δy = 305.1(9) μm. This measured distance is in agreement with the predicted distances travelled in x and y of 438(6) μm and 302(4) μm, respectively, calculated using the scaling factors S_x = 21.9(3) and S_y = 15.1(2). It was found that the first step taken in y, after the mirror had reversed the scanning direction, was shorter than the subsequent steps in y. Thus there is a shift in y between adjacent scan lines. For reference, the difference in the y position of adjacent craters was measured as 66(2) μm.

4.3 Spatial Resolution

The spatial resolution at which surface features can be resolved with the LAS system is limited by either the diameter of the ablated crater, or the smallest step size that the laser beam can move on the target surface. The diameter of the ablated crater can be measured directly with an optical microscope, for comparison with the smallest achievable steps calculated in Table 4.1. Alternatively, the diameter of the ablated crater can be estimated theoretically with the following method.

4.3.1 Ablation Diameter

The diameter of the ablated crater is related to the focused $1/e^2$ beam diameter [1], D_f, which can be calculated from a measurement of the laser beam width before the focusing lens, using the relationship [91, 92]

$$D_f = \frac{4M^2\lambda f}{\pi D}, \tag{4.2}$$

where f is the lens' focal length, λ the laser wavelength, D is the $1/e^2$ diameter of the beam as it enters the lens and M^2 is the beam quality parameter. It is important to note that material is only ablated where the laser spot fluence is higher than the ablation threshold of the material being ablated. The relationship between the ablated crater diameter, D_a, and the

1. The $1/e^2$ beam diameter is the width between two points at which the intensity is $1/e^2$ of the peak value.

threshold fluence, F_{th}, is given by [93–95]

$$D_a^2 = \frac{D_f^2}{2} ln\left(\frac{F_0}{F_{th}}\right), \tag{4.3}$$

where the peak fluence, F_0, is

$$F_0 = \frac{8E_T}{\pi D_f^2} \tag{4.4}$$

and E_T is the total beam energy per pulse. It is also important to note that the absorptivity of the irradiated zone changes after multiple pulses. The threshold fluence after N pulses, $F_{th}(N)$ is related to the single-shot threshold fluence by a power law [96]

$$F_{th}(N) = F_{th}(1)N^{\zeta-1}, \tag{4.5}$$

where ζ is known as the incubation coefficient, and $F_{th}(1)$ is the fluence threshold of the first laser shot on a fresh target. Since the threshold fluence changes, D_a will vary depending on the number of times a particular spot has been ablated, and damage accumulation will affect the spatial resolution for repeated pulses as well as the ion beam current.

The profile of the laser beam before focusing was measured by mounting a razor blade on a micrometer stage and moving the blade in steps of 0.25 mm across the beam, while measuring the average laser beam energy that passes the blade for 10 s at each step. The laser beam energy was measured after the focusing lens but before being reflected by the motorized mirror. The resulting profile was fit with an integrated Gaussian function, shown in Fig. 4.7, from which the $1/e^2$ diameter D = 3.9(1) mm was extracted.

The M^2 beam quality parameter was specified for the laser as $M^2 < 1.3$ [90]. The M^2 parameter was also measured, by deflecting the laser beam after focusing away from the motorized mirror mount, and taking knife-edge measurements of the beam intensity profile near and around the focus, as outlined in [92]. The beam quality was measured as $M^2 = 1.32(7)$, which agrees with the laser specification of $M^2 < 1.3$. Thus D_f was calculated using Eq.

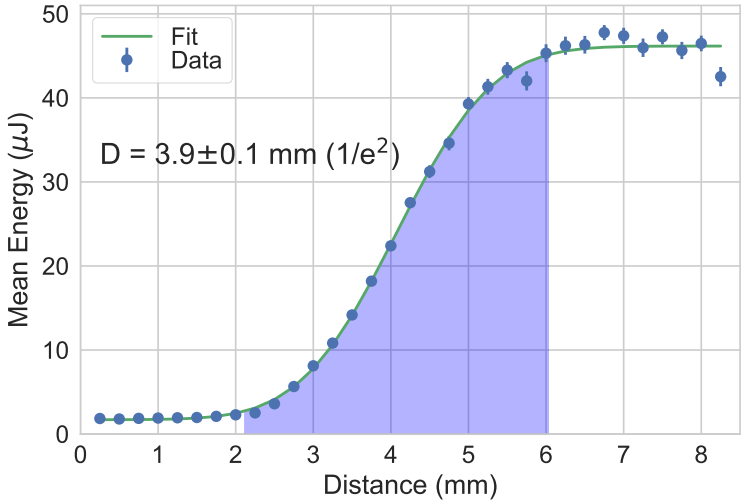

Figure 4.7 Measurement of the laser beam profile before entering the focusing lens. The mean laser energy and its associated uncertainty, calculated as the standard deviation, is fit with an integrated Gaussian function to extract the beam diameter.

(4.2), with $f = 750(8)$ mm, $\lambda = 349$ nm, and $M^2 = 1.32(7)$ as D_f = 113(7) μm, with a peak fluence of 0.9 J/cm^2. The focus of the laser beam on the target surface was optimized prior to this profile measurement by adjusting the position of the focusing lens, and maximizing the ion current produced from the target holder.

To calculate the diameter of the ablated crater with Eq. (4.3), $F_{th}(1)$ and ζ must be known. The incubation parameter ζ is sensitive to the pulse duration, and will typically have a value between 0.8-0.9 for femtosecond and nanosecond pulses, respectively [97]. However, the single-shot fluence threshold $F_{th}(1)$ can vary by orders of magnitude depending on the wavelength [98–100], pulse duration and repetition rate [101], material composition and beam diameter [102, 103]. Thus it is difficult to choose a value for $F_{th}(1)$ when calculating the ablated crater diameter for this experiment. However, it will be demonstrated in the following section that it is possible to estimate $F_{th}(1)$ using Eqs. (4.3-4.5), for comparison with results from the literature.

4.3.2 Scanning Metal Junctions

The metals of the multi-metal targets can be distinguished by the amplitude of emitted ion current produced at constant average laser beam power. This fact is utilized to perform a measurement of the spatial resolution for the setup. When the laser spot was scanned across the junction of two metals, the ion current appeared as a smeared step function. The width of this transition, D_t, was measured by fitting an integrated Gaussian function to the resulting distribution, from which the spatial resolution was extracted as the $1/e^2$ diameter. Both motorized mirror mounts were capable of repeatable increments smaller than 4 μm on the target surface, which is significantly smaller than the focused laser spot diameter on the target surface. Thus the resolution was dominated by the laser spot diameter on the target surface, and both mirror actuator types were found to have similar spatial resolutions.

The spatial resolution was measured with the Au-Nb-Cu target as well as an Al-Si-Au target. The Al-Si-Au target consisted of a 0.4 mm thick piece of aluminum foil and 0.1 mm thick gold foil on top of a silicon wafer, such that the upper portion of the face is covered with gold and the lower portion is covered by aluminum, with a 2 mm gap of silicon in between. This target provides straight edges of gold and aluminum that span the diameter of the target, allowing for more scans of metal transitions to be made before needing to replace the target. For the experiments presented here, the ion current was averaged over a time window of 0.25 s for each scan position, and the standard deviation was calculated and is presented as the statistical uncertainty. The laser repetition rate was fixed at 1000 Hz and measurements of the laser beam energy were taken at the location just before the beam reflects from the motorized mirror. The following measurements were performed with the PI mirror mount by scanning targets in the y direction, thus the scaling factor S_y=14.9(2) is used to calculate the results. The junction between the stainless steel target-holder and the niobium component of the Au-Nb-Cu target was scanned, and the resulting profile fit with an integrated Gaussian function. The $1/e^2$ full width of the transition was extracted as D_t = 50(3) μm, with the laser beam energy per pulse measured as 33(1) μJ. The Al-Si-Au target was then installed such that the aluminum and gold edges were perpendicular to the y-direction. The

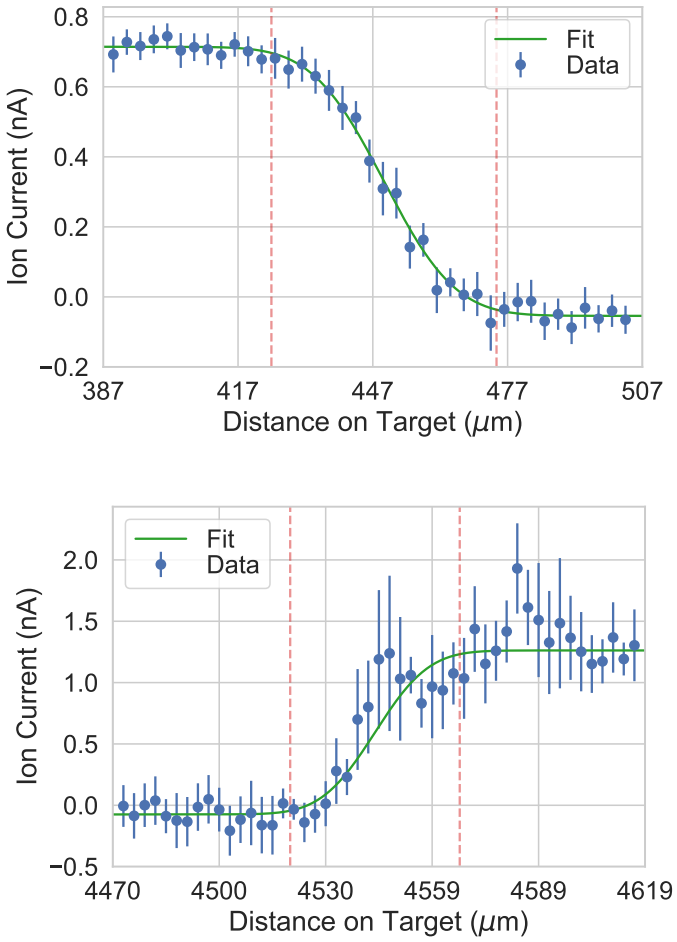

Figure 4.8 A representative scan of the transition between stainless steel and niobium (top), and silicon and gold foil (bottom). The profiles are fit with integrated gaussian functions from which the $1/e^2$ diameters are extracted as 50(3) μm and 47(7) μm respectively.

junction of silicon and gold foil was scanned, and the width extracted as D_t = 47(7) μm, with the laser beam energy measured as 42(1) μJ. These scans are displayed on the top and bottom of Fig. 4.8 for stainless steel-niobium and silicon-gold foil interfaces, respectively. Under the described experimental conditions no ablation was observed on the Al target.

Using Eqs. (4.3-4.5), the threshold fluence for stainless steel was estimated. With $D_a = 50(3)$ μm, $E_T = 33(1)$ μJ and $D_f = 113(7)$ μm, the single shot threshold fluence could be expressed as $F_{th}(1) = {}^{0.4}/_{N^{\zeta-1}}$ J/cm^2. Since the scan step size, Δs, was much smaller than the beam diameter, D_f, many of the scan points were overlapping and thus N was assumed to be the number of overlapping pulses. Using the laser repetition rate, f_r, and the measurement time, t_m, the number of overlapping pulses was estimated as $N \approx f_r \times t_m \times D_f/\Delta s \approx 1000 \times 0.25 \times 113/2 \approx 14000$, where D_f was assumed to be the maximum distance at which two scan points were considered to be overlapping. Thus the single-shot threshold fluence was calculated as $F_{th}(1) \sim 1.2$ J/cm^2, assuming an incubation coefficient of $\zeta = 0.9$ [97].

It could be argued that the choice of D_f as the overlap length to be divided by Δs is somewhat arbitrary, and that N falls within a range of values. However, the value of $F_{th}(1)$ is not strongly dependent on N, provided that $N \sim \mathcal{O}(1000)$ pulses. For example, if D_a had been chosen as the overlap length instead, then $N \approx 6250$ and $F_{th}(1) \sim 1.0$ J/cm^2. Taking a range of values for N from 6250 to 14000 results in an estimate for the single-shot threshold fluence of $F_{th}(1) \sim 1.0 - 1.2$ J/cm^2. This result is comparable to the results of a study where, for a comparable beam diameter, the threshold fluence after 100 pulses was found to be $F_{th}(100) \sim 0.8$ J/cm^2 for stainless steel [102]. Assuming the same incubation coefficient, this corresponds to a single-shot threshold fluence of $F_{th}(1) \sim 1.3$ J/cm^2.

4.4 Ion Transport Efficiency

The impact of the position of the laser spot on the ion transport efficiency has been studied. The ion transport efficiency, T_{eff}, is measured as the ratio of the ion current arriving at the

Faraday cup, I_{FC}, to the ion current leaving the target holder, I_{TH},

$$T_{eff} = \frac{I_{FC}}{I_{TH}}. \tag{4.6}$$

However, the process of laser ablation does not only release singly charged ions, but electrons, neutrals and multiply-charged ions as well [104]. Thus, Eq. (4.6) is only an accurate measurement of the ion transport efficiency if the electrons are re-captured by the target-holder, and the distribution of ionisation states in the ablated material is dominated by $+1$. To prevent electrons escaping the target holder, a positive DC bias of 32V was applied to the target holder. This increase in beam energy required an adjustment of the DC potentials on the quadrupole bender electrodes to increase the bending efficiency, with potentials of -200 V and 40 V applied to the quadrupole electrodes nearest to the Faraday cup.

The laser beam energy and DC biases applied to the ion source were adjusted to maximise the transport efficiency, while ensuring that the potential gradient between the target holder and the first extraction electrode was sufficient to re-capture electrons on the target holder. Replacing the diverging and converging lenses with the Thorlabs beam expander increased the diameter of laser beam as it enters the focusing lens from $3.9(1)$ mm to $9.6(1)$ mm, thus reducing the calculated spot diameter on the target to $D_f = 45(1)$ μm. The laser repetition rate was fixed at 500 Hz for the experiment and the laser beam energy measured as $18.1(1)$ μJ per pulse, which calculates to a peak fluence of 2.3 J/cm^2. The laser beam energy was measured by placing the energy meter at the target's location, but without the target in place. The Cu target was scanned with a step size of 109(2) μm in x and 75(1) μm in y. The current was measured simultaneously at the target holder and Faraday cup for 8 s at each point of the scan.

For 5741 scan points across the surface of the Cu target, the average current measured leaving the target holder was 121(17) nA with the uncertainty taken as the standard deviation. The average current measured arriving at the Faraday cup for the same scan points was 2.6(2) nA. From Eq. (4.6), the average ion transport efficiency across the target surface was calculated to be 2.2(7)%. A plot of the calculated efficiency for each scan point is shown in Fig. 4.9. The

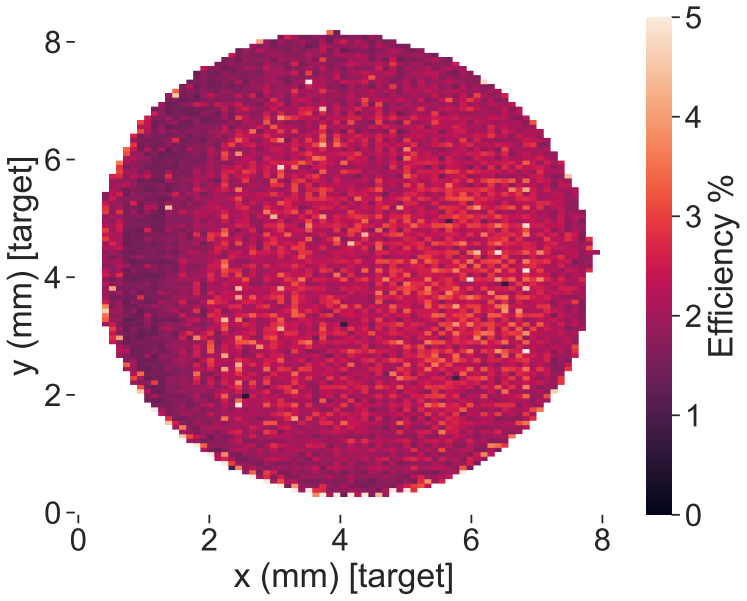

Figure 4.9 A 2D scan of the ion transport efficiency, calculated with Eq. (4.6), across the surface of a solid Cu target, with a step size of 109(2) μm in x and 75(1) μm in y.

efficiency is fairly homogeneous across the surface of the target, with the left side slightly less efficient than the right. This small gradient could be caused by the difference in proximity to the bending quadrupole electrodes.

4.5 Discussion

The use of high-precision motorized kinematic mirror mounts in laser ablation is a simple and cost-effective solution for positioning the laser beam on a target, without the need to move the target inside a vacuum chamber. A 2D scan of the ion current may be used to establish a coordinate system on the surface of the target, by a simple transformation of the mirror mount motor positions. Once a coordinate system is established, different target materials may be selected and the ablated ions may be guided to another device such as a mass spectrometer. Multi-element targets can be designed from 1 mm diameter stock materials and selectively ablated for mass spectrometer calibration. The establishment of a coordinate system also

allows for the monitoring and management of damage accumulation on the target surface.

The PI and Thorlabs mirror mounts are capable of laser spot displacements less than 4 μm on the target surface in a configuration like ours, where a focal lens of 750 mm was used and the distance between the deflecting mirror and the target was 350 mm. However, the spatial resolution of the presented LAS system is limited by the focused laser beam diameter on the target, which is one of the factors affecting the diameter of ablated craters. In principle, the diameter of an ablated crater is also dependent on the material and sensitive to the total optical energy deposited on the target. Systems may be designed to leverage this for a specific application. By measuring the transitions between metals, the ablation spot diameter was shown to be as low as 40-50 μm for this particular device. The calculated laser beam diameter on the target was reduced by $\approx 60\%$ by expanding the beam from 3.9(1) mm to 9.6(1) mm before focusing. The spatial resolution and resolving power of the LAS could be further improved by decreasing the focal length of the focusing lens.

The ion transport efficiency of the ion-source assembly and quadrupole bender was measured as 2.2(7)% for Cu, with a slight gradient in the observed in the x direction. This deviation from homogeneity is likely due to a difference in proximity between the ion trajectories and the quadrupole electrodes. For the ablation of Cu with a 308 nm laser spot at a fluence of 3 J/cm^2, a study has shown that the charge state distribution has a Cu^{1+}/Cu^{2+} ratio of 15.2 [105]. There, the average kinetic energy of ablated Cu ions was $\mathscr{O} \sim (100)$ eV and the angular distribution of ablated yield was found to have a Full Width at Half Maximum (FWHM) of 36°. This study had similar ablation conditions to the system presented in this work, thus singly charged Cu ions are expected to dominate the ablated ions, and ions are expected to have similar angular and kinetic energy distributions. In the system presented here, the aperture of the final electrode subtends an angle of $\sim 15°$. Assuming a Guassian angular distribution, $\sim$65% of ablated ions are expected to be lost due to collision with the extraction electrodes, primarily the first extraction electrode.

Further ion loss is expected to result from inefficient bending of the quadrupole bender. The ion transport efficiency has been investigated using SIMION simulations based on published ion distributions [105, 85, 89], and gave results comparable to the measured ion transport efficiency. Further simulations were conducted with ions leaving normal to the target surface with energies from 0 eV to 80 eV, with an increment of 1 eV between consecutive ions. Simulation results indicated that the widely spaced electrodes of the quadrupole bender, with the same potentials applied to the quadrupole electrodes as in the experiment, caused the bender to effectively act as a kinetic energy filter.

In simulations, the quadrupole bender was unable to sufficiently bend Cu^{1+} ions with a kinetic energy greater than $\sim$20 eV towards the Faraday cup for collection. This cut-off in kinetic energy was independent of the ion's origin on the target surface within a range of ~ 2 eV, and was significantly lower than the expected average kinetic energy of Cu^{1+} ions reported in literature. The combined effects of ion loss due to the acceptance of the ion source geometry and inefficient bending are thought to result in the observed low ion transport efficiency. However, it shall be noted that the focus of this work has been to demonstrate the feasibility of a LAS with a large ablation range of up to 50 mm. A bender with smaller inter-electrode spacing and a biased aperture will improve the ion transmission efficiency, but at the cost of a reduced scanning range.

Chapter 5

MRTOF Mass Spectrometry

The Multi-Reflection Time-of-Flight Mass Spectrometer (MR TOF), as first proposed by H. Wollnik et. al. [106], is becoming increasingly popular at radioactive ion beam facilities across the world [107–113]. This is in part due to its excellent performance as an isobar separator, as well as its ability to achieve a mass-resolving power (MRP) in excess of 10^5, with only milliseconds of measurement time and single ion sensitivity [114, 115]. In particular, the single ion sensitivity makes the MRTOF a device of choice for the Ba-tagging system. The presented design is based on the MRTOF used in the ISOLTRAP experiment at the ISOLDE facility [114]. This chapter explores the ways in which the MRTOF may be optimised and operated to achieve the MRP needed to separate ^{136}Ba and ^{136}Xe for Ba-tagging.

5.1 Operational Principles of the MRTOF

A non-relativistic ion being accelerated by a potential energy gradient ΔU has a kinetic energy

$$K = q\,\Delta U = \frac{1}{2}\,m\,v^2, \tag{5.1}$$

where q is the charge of the ion and m is its mass. Hence the ion has a velocity

$$v = \sqrt{\frac{2\,q\,\Delta U}{m}}\ . \tag{5.2}$$

This means that in principle, the time t it takes to traverse a path of length L is proportional to the square root of the mass-to-charge ratio, $t = L/v \propto \sqrt{m/q}$. Hence, the MRP power can be expressed as

$$R \equiv \frac{m}{\Delta m} = \frac{t}{2\Delta t}. \tag{5.3}$$

In reality however, the ions have an initial position and velocity distribution, which causes ions with the same m/q to have a distribution in TOF.

For extraction from the LPT, the ions are placed on a potential energy slope. At the time of extraction, ions traveling in the opposite direction to the exit will first have to reverse their momentum, then re-accelerate. This creates a fundamental lower limit to the peak width Δt_{ar}, which is called the turn-around time [116]. The difference in ion starting positions, when the potentials are switched to extraction, creates a spread in the kinetic energy, as ions are placed at different heights on the potential energy slope. Thus a steeper slope creates a smaller turn around time, but increases the spread in kinetic energy. The initial spread in kinetic energy gives the ion bunch what is known as a time focus. A time focus is a point in space at which ions of the same m/q will arrive at the same time, even though they have slightly different kinetic energies.

In general, the goal of the MRTOF is to shift the initial location of the time focus at the exit of the LPT to the position of the TOF detector, while greatly increasing the path length travelled by the ions. Thereby maximising the MRP power as expressed in Eq. (5.3). Ideally, Δt should be comparable to the turn around time Δt_{ar} and t should be as long as possible. There are multiple ways to extend the ion's flight path, as is discussed in [117]. For this work, ion bunches are trapped between two coaxial electrostatic mirrors, on either side of a central

drift-tube, and reflected between them for N reflections. A reflection through an electrostatic mirror can be used to shift the time focus position, by altering the path lengths of ions with slightly different kinetic energies [118]. Thus careful manipulation of the electric fields in the mirror allows the time focus to be shifted from the initial location to the TOF detector, as shall be discussed in the following sections.

5.2 Ion Optics

In this work, transfer matrix formalism will be used to describe the effect of ion optical elements on the trajectories of ions. The properties of an ion's trajectory can be described at any point in its flight with the vector

$$X = [x, a, y, b, \delta, t'] \tag{5.4}$$

where x and y are transverse displacements and $a = \frac{\partial x}{\partial z}$ and $b = \frac{\partial y}{\partial z}$ are the angular directions of motion, all of which are relative to a reference trajectory [119] which is usually referred to as the optical axis. The variable

$$\delta = \frac{K - K_0}{K_0} \tag{5.5}$$

is the deviation of an ion's kinetic energy K from the reference ion's kinetic energy K_0. Likewise, $t' = t - t_0$ is the difference in time-of-flight (TOF) of the considered ion from the reference ion. After passage through an ion optical element, the components of X can be calculated with

$$X_i = \sum_j Y_j \left[(X_i|Y_j) + \sum_k \frac{Y_k}{2} \left[(X_i|Y_j Y_k) + \sum_l \frac{Y_l}{3} \left[(X_i|Y_j Y_k Y_l) + ... \right] \right] \right], \tag{5.6}$$

where Y_i are the components of the initial vector and $(X_i|Y_j)$, $(X_i|Y_jY_k)$ and $(X_i|Y_jY_kY_l)$ are the first, second and third order transfer coefficients [120]. The ion trajectory can then be described using a matrix equation, where the matrix elements are the transfer coefficients

that map initial conditions to final conditions. The first, second and third order matrices are 6×6, 6×6^2 and 6×6^3, respectively.

The ion beam can be more formally characterized in terms of its emittance. The beam emittance is a conserved quantity along the trajectory of the ion bunch. It is a 6-dimensional phase-space volume, although it is typically projected onto a single position and momentum plane e.g. (x, p_x). Instead of the phase-space area, the trace-space area is often used for convenience since it is transverse to the direction of motion. The root mean squared (rms) trace-space emittance is defined for a distribution of particles in the (x, a) plane as

$$\varepsilon^x_{rms} = \sqrt{\langle x^2 \rangle \langle a^2 \rangle - \langle xa \rangle^2} \tag{5.7}$$

and is usually expressed in units of mm·mrad [121].

5.3 MRTOF Operation Mode

The MRTOF mirrors consist of 6 electrodes each, where the outer electrodes 1-4 are used to create a reflecting field, and the inner electrodes 5 and 6 create an accelerating einzel lens field. The accelerating field is used to steer ions so that stable trajectories form inside the analyzer. When ions are trapped between the mirrors, the steering electrodes are tuned such that their trajectories form a point-to-parallel and parallel-to-point configuration. If a parallel ion beam undergoes a reflection in an electrostatic mirror, the beam will focus to a point at the centre of the analyzer, and after undergoing another reflection, the beam will become parallel again, as shown at the top of Fig. 5.1. After a reflection in the MR TOF, ion properties can be expressed in terms of transfer coefficients as [122]

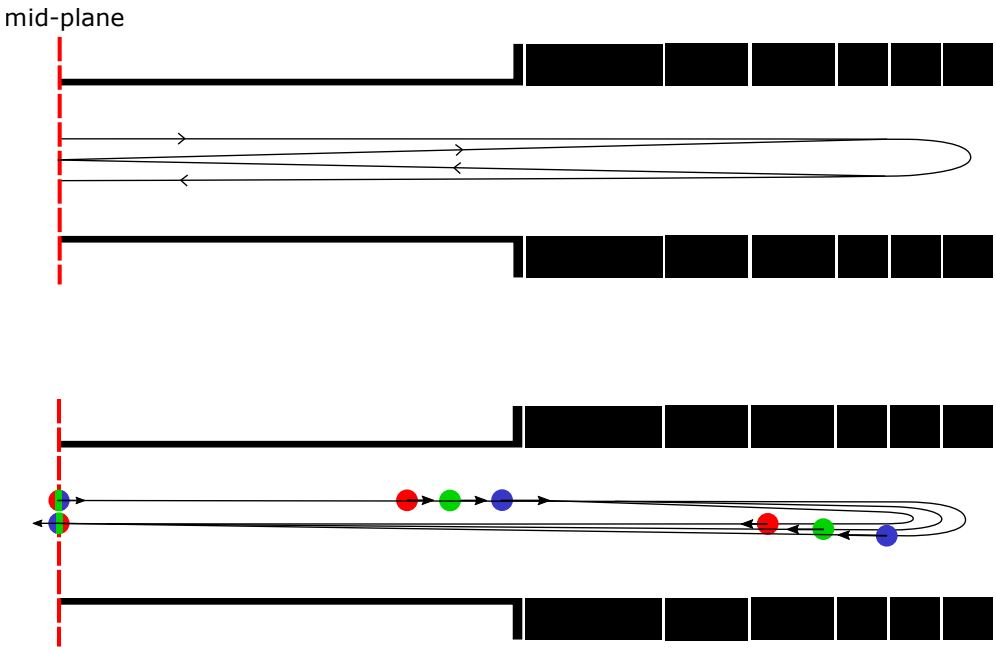

Figure 5.1 (top) Parallel-to-point ion trajectories for a single reflection in the MRTOF. (bottom) An isochronous reflection in the MRTOF, in which ions with the same m/q travel different path lengths through the mirror such that the time taken to complete a reflection for the ions is the same.

$$x = (x|x)x_0 + (x|a)a_0 + (x|x\delta)x_0\delta + (x|a\delta)a_0\delta + \ldots \tag{5.8}$$

$$a = (a|x)x_0 + (a|a)a_0 + (a|x\delta)x_0\delta + (a|a\delta)a_0\delta + \ldots \tag{5.9}$$

$$y = (y|y)y_0 + (y|b)b_0 + (y|y\delta)y_0\delta + (y|b\delta)b_0\delta + \ldots \tag{5.10}$$

$$b = (b|y)y_0 + (b|b)b_0 + (b|y\delta)y_0\delta + (b|b\delta)b_0\delta + \ldots \tag{5.11}$$

$$\begin{aligned} t' = {} & (t|\delta)\delta + (t|xx)x_0^2 + (t|xa)x_0a_0 + (t|aa)a_0^2 + (t|yy)y_0^2 + (t|yb)y_0b_0 \\ & + (t|bb)b_0^2 + (t|\delta\delta)\delta^2 + (t|\delta\delta\delta)\delta^3 + (t|\delta\delta\delta\delta)\delta^4 + (t|xx\delta)x_0^2\delta \\ & + (t|xa\delta)x_0a_0\delta + (t|aa\delta)a_0^2\delta + (t|yy\delta)y_0^2\delta + (t|yb\delta)y_0b_0\delta \\ & + (t|bb\delta)b_0^2\delta + \ldots, \end{aligned} \tag{5.12}$$

where the measurement point is taken to be the midplane between the coaxial mirrors. Optimization of the MR TOF can be achieved through precise manipulation of the coefficients

in Eqs. (5.8-5.12). For example, $(x|x)$, $(y|y)$ control the parallel-to-point behaviour of the ion bunch through a reflection. If $(x|x) = (y|y) = 0$, the final transverse displacement does not depend on initial transverse displacement, i.e., the ions are focused to a point in the $x-y$ plane as shown on the top in Fig. 5.1. Due to the MRTOF's symmetry, setting $(x|x) = (y|y) = 0$ for one reflection will automatically set [122]

$$(a|a) = (b|b) = 0. \tag{5.13}$$

The second order position and angular effects on the time focus can also be tuned simultaneously to

$$(t|xx) = (t|aa) = (t|yy) = (t|bb) = 0. \tag{5.14}$$

After one full turn in the analyzer there will be

$$(x|a) = (a|x) = (y|b) = (b|y) = 0, \tag{5.15}$$

which also fulfills

$$(t|xa) = (t|yb) = 0. \tag{5.16}$$

This automatically leads to the vanishing of

$$(x|\delta x) = (x|a\delta) = (a|x\delta) = (a|a\delta) = (y|y\delta) = (y|b\delta) = (b|y\delta) = (b|b\delta) = 0. \tag{5.17}$$

The LPT creates a time focus that is a few cm from the exit of the trap. In typical MR TOF operation, the time-focus is shifted onto the detector over the desired number of reflections N. Alternatively, $N-1$ reflections can be tuned to be isochronous with $(t|\delta)$=$(t|\delta\delta)$=$(t|\delta\delta\delta)$=0, and the last reflection can be used to shift the time-focus onto the detector in a method known as delayed bunching [123]. Thus the last reflection in the MRTOF is referred to as the time-focus shift (TFS) reflection. A diagram for an isochronous reflection is shown on the bottom of Fig. 5.1.

The method of delayed bunching can reduce space-charge effects, in which ions repel each other, by keeping ion bunches spread out in space until they arrive at the detector. Since the optimisation of the mirror fields is performed by calculating ion trajectories, delayed bunching offers an additional benefit in that the optimisation problem is reduced to the optimisation of a single isochronous reflection and time focus shift. Which is in contrast to the calculation of ion trajectories over hundreds of revolutions as in the conventional operation mode. Lastly, with delayed bunching the optimised fields are in principle de-coupled from a specific number of revolutions which makes operation of the MRTOF more versatile, and offers an increased MRP for lower revolution numbers [124].

As ion species are reflected between the electrostatic mirrors, the lighter and therefore quicker ions can in some cases overlap heavier ions. Thus it is possible to have peaks in the TOF spectra that have different revolution numbers, which can create ambiguity and possibly impede a particular mass measurement. To prevent this, it is possible to eject unwanted ions with a mass-selector, which is an electrode that is pulsed to destabilise unwanted ions as they pass by. In the presented MRTOF design, a mass-selector is positioned at the center of the drift-tube, and used to eject unwanted ions while the ions of interest are safely reflecting in the mirror.

Simulation of the MRTOF is used to optimize the electric fields in the electrostatic mirrors for the operation mode described above. Furthermore, simulation is also used to calculate the anticipated MRP, which will be discussed in the following section.

5.4 Simulation of the MRTOF with SIMION

SIMION [125] is a software program that calculates the trajectories of charged particles through electrostatic and magnetic fields. The software uses the Runge-Kutta method to solve the Laplace equation in 3D for a given electrode geometry. An electrode geometry can be specified by the user with constructive solid geometry primitives, or imported directly from CAD software. The electrode geometry and resulting potentials are stored in a 3D grid called a potential array. Since the MRTOF is comprised of cylindrical electrodes, cylindrical symmetry was used for the simulation, reducing the size of the potential array and thus allowing for a smaller grid unit size. The MR TOF has been optimized and simulated and with SIMION 8.1, using simulated $^{136}Ba^{+}$ ions from an LPT designed at TRIUMF [63].

5.4.1 Optimization

After ions are cooled and bunched in the RFQ buncher, they are accelerated by a DC potential slope out of the LPT and into the MRTOF. As explained earlier, this produces a slight spread in ion kinetic energy and creates a time focus near the exit of the trap. The Full Width Half Maximum (FWHM) of the first time focus is set by the turn around time of $\Delta t_{ar} \sim 7$ ns. The simulated ion bunch had a transverse emittance of 0.4 mm·mrad as shown in Fig. 5.2. The mean kinetic energy of the ions was 1163 eV with a FWHM of 23 eV. There are 6 potentials in the MR TOF mirrors that must be optimized in order to minimize the 6 coefficients in Eqs. (5.8-5.12). To optimize the mirror potentials, SIMION's native Nelder-Mead search algorithm was used. The algorithm takes in a scalar metric to minimize χ, which was calculated as a weighted sum of the coefficients to minimize [122]

$$\chi = \omega_1(x|x) + \omega_2(y|y) + \omega_3(t|\delta) + \omega_4(t|\delta\delta) + \omega_5(t|\delta\delta\delta) + \omega_6(t|xx) + \omega_7(t|yy), \quad (5.18)$$

where ω_i are user defined weights. Test ions were used to calculate the transfer coefficients of the MRTOF mirror for a given set of potentials. The test ions were flown for a single

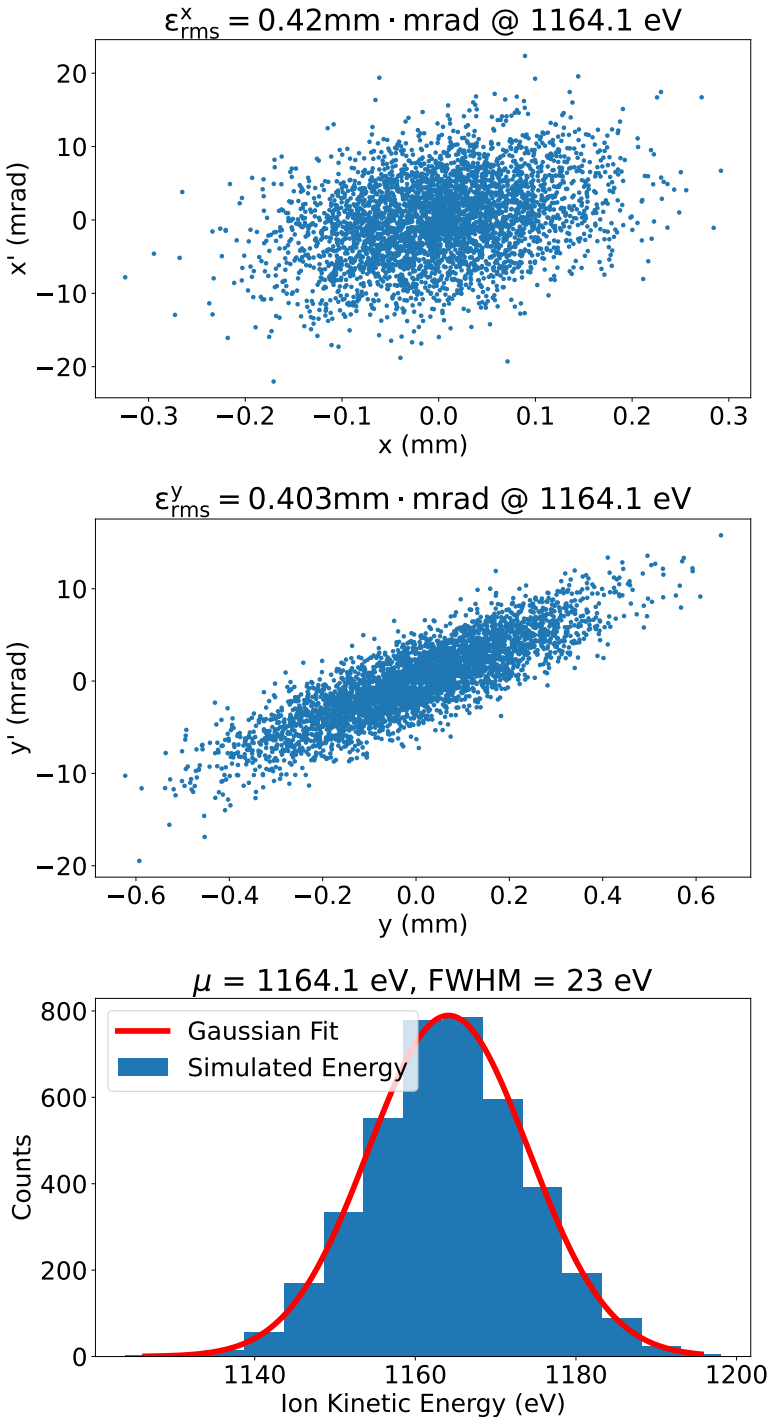

Figure 5.2 (top)(middle) Plots of the ion phase space in the x and y directions respectively from which the transverse emittance is calculated. (bottom) A plot of the kinetic energy distribution of ions ejected from the LPT with a Gaussian fit.

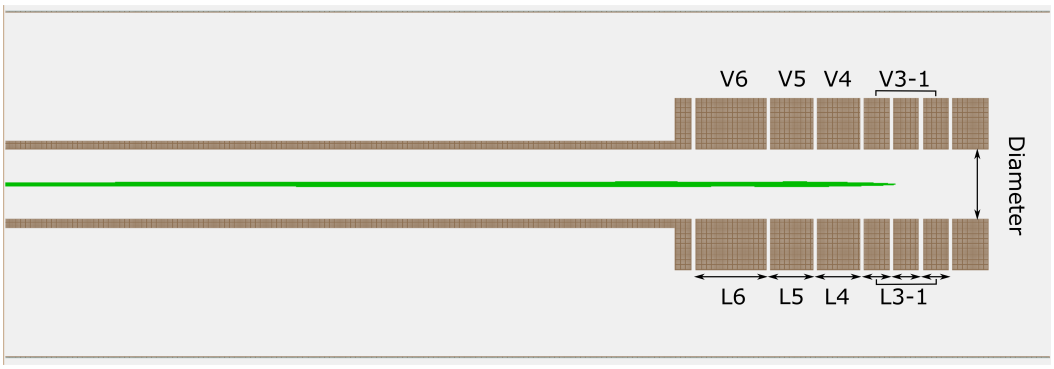

Figure 5.3 SIMION simulation for a single reflection in the MR TOF using simulated ions from a LPT. A reflection in the MR TOF is used to calculate the relevant coefficients in Eqs. (5.8-5.12), to optimize the mirror potentials. The parameters V1-6 refer to the applied voltages, and L1-6 refer to electrode length.

reflection from the mid-plane of the Analyzer to record their initial and final parameters, as shown in Fig. 5.3. The transfer coefficients were then extracted with polynomial fits between the final and initial parameters and used to calculate the metric χ.

Since the simplex optimizer could only yield a local minima within a small neighbourhood of the starting potentials, many starting potentials were generated randomly with a sobol sequence [126] and tested. The metric χ was calculated for each set of potentials and the 100 simulations with the smallest χ were selected for further optimization by the simplex optimizer. The resolution was then tested for the top performing candidate. Due to the large computing requirements, this was performed on the Compute Canada High Performance Computing clusters [127]. Besides electrode potentials, the MRTOF has several physical parameters that may be adjusted, namely the lengths of the electrodes and their diameter, which are referred to collectively as a geometry. Multiple mirror geometries were deployed and their potentials optimized, with the chosen mirror geometry given in Table 5.1. The optimal electrode potentials are given in Table 5.2, where the potentials V1-6 refer to the electrodes from furthest to nearest the drift-tube, respectively. With the addition of physical parameters, the optimization problem quickly became intractable, thus it is noted that the optimization of the electrode geometry is not exhaustive of the full parameter space available. However, the resulting optimization is able to successfully control TOF aberrations and

Electrode Dimensions (mm)						
L1	L2	L3	L4	L5	L6	Diameter
15	15	15	25	25	41	54

Table 5.1 The chosen electrode dimensions for the electrostatic mirrors.

	Entrance Mirror Potentials (V)					
	V1	V2	V3	V4	V5	V6
Injection	0	0	1106.54	1147.19	-304.05	-2893.38
Isochronous	1725.75	1662.25				
TFS	1441	1441				
	Exit Mirror Potentials (V)					
	V1	V2	V3	V4	V5	V6
Injection	1725.75	1662.25	1106.54	1147.19	-304.05	-2893.38
Isochronous	1725.75	1662.25				
Ejection	0	0				

Table 5.2 The optimized mirror potentials for both the entrance and exit mirrors. In each mirror, the outer two electrodes are switched to inject and eject ions. A third state for the switched electrodes in the entrance mirror is used to shift the time focus onto the detector with the final reflection.

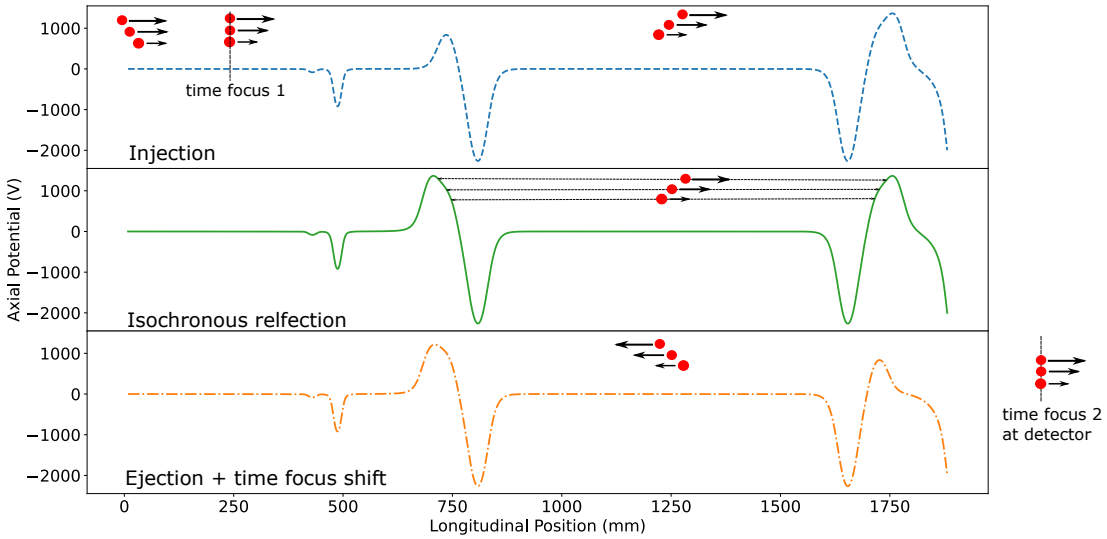

Figure 5.4 A plot of the simulated axial potential along the MRTOF's optical axis during different stages of the measurement cycle.

achieve a high MRP in excess of $m/\Delta m > 1 \times 10^5$ as required, which will be demonstrated in the following section.

5.4.2 Simulation Results

Simulated $^{136}Ba^{+}$ ions from the Radio Frequency Quadrupole (RFQ) buncher were flown from the location of the LPT exit and injected into the MRTOF. The MRTOF electrode biases were operated in the simulation in an identical manner to the physical setup. During the injection phase, the outer two electrodes in the entrance mirror, V1 and V2, were switched to 0 V to allow the ions to pass through the mirror. Once ions had reached the center of the drift-tube the electrodes were switched to their isochronous values. In the isochronous reflection phase, ions were trapped between the electrostatic mirrors for a specified number of revolutions. The optimized isochronous voltage settings were tuned to maintain the TOF dispersion of the ions, by taking faster and slower ions on longer and shorter paths through the electrostatic mirrors respectively. Thus the TOF for a full revolution was tuned to be the same for all ions, despite a difference in kinetic energy of up to $\pm 2\%$. Plots of the simulated axial

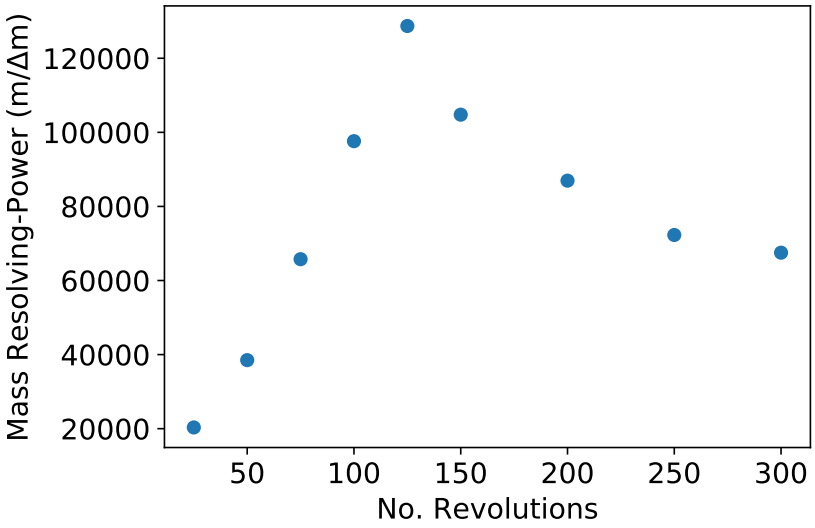

Figure 5.5 A plot of the simulated mass resolving-power as a function of the number of revolutions.

potential for each stage of the MRTOF's operation is shown in Fig. 5.4. Half a revolution before ejection, the V1 and V2 electrodes are switched to a third state for a final reflection that shifts the time-focus from its initial location near the LPT and onto the detector plane.

The TOF spectra for the $^{136}Ba^{+}$ ions was simulated for 25-300 revolutions in the MRTOF. Each spectrum was fit with an exponentially modified Gaussian function, to accommodate small asymmetries in the peak shapes [128]. The MRP was calculated as a function of the number of revolutions using Eq. (5.3), which is displayed in Fig. 5.5, where Δt was extracted as the FWHM of the fitted peak and t was the peak center. In the region of 25-125 revolutions, the MRP rapidly increases to $m/\Delta m = 1.2 \times 10^5$, after which it starts to decrease. The TOF spectrum at 125 revolutions is shown on the top of Fig. 5.6, where the FWHM was calculated as 27 ns for a flight time of ≈ 6.7 ms. Before the final reflection, the FWHM of the TOF peak was calculated as $\Delta t \approx 200$ ns, indicating that the delayed bunching was functioning as anticipated. However, the decrease in MRP after 125 revolutions suggests that the optimisation was not fully turn-independent.

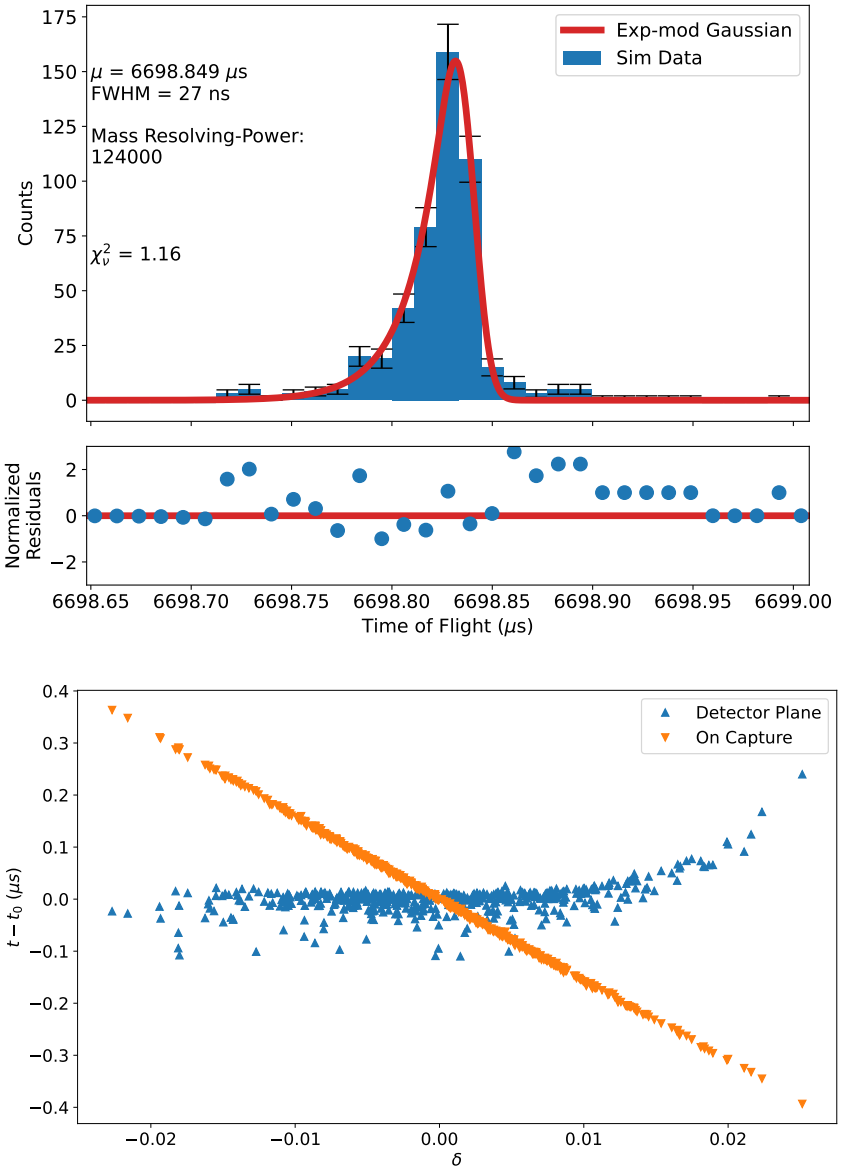

Figure 5.6 (top) Simulated TOF spectrum for $^{136}Ba^{+}$ ions at 125 revolutions. (bottom) The TOF dispersion as a function of $\delta = (K - K_0)/K_0$, showing the formation of a second time focus at the detector plane after 125 revolutions.

The difference in TOF for each ion from the average, $t - t_0$, is plotted as a function of δ as defined by Eq. (5.5) on the bottom of Fig. 5.6. This plot shows the TOF dispersion as a function of the fractional deviation in ion kinetic energy at two locations. First when the ions reach the center of the Analyzer and the entrance mirror is closed, and again when ions reach the detector plane after the TFS reflection to form the second time focus. The TOF dispersion at the second time focus shows contributions from $(t|\delta\delta\delta)$ that become significant for $\delta > 0.02$, suggesting that the MRP can benefit from reducing the ion kinetic energy spread.

5.5 The MRTOF Design

A 3D model for the MRTOF was created with the Computer Aided Design (CAD) software SolidWorks. The MRTOF model consists of two primary sub-assemblies, which are the Ion Optics and Analyzer assemblies shown in Fig. 5.7. Both assemblies are mounted on either side of an DN160CF double-faced flange, which is labeled 'base-flange' in the same figure. The Ion Optics sub-assembly contains two sets of X-Y steerers that serve to align the ion beam with the optical axis, as well as two einzel lens assemblies that control the focus and diameter of the beam. Each X-Y steerer is formed by four 25.4 mm long plates machined from 304 stainless steel, mounted onto polyether ether ketone (PEEK) rods to create a square cross-section. The distance between opposite steerer plates is 21.65 mm and there is a 10.6 mm longitudinal gap between the steerer sets. The PEEK rods are mounted onto the last electrode of the einzel lenses, where grooves maintain the correct orientation of the steerer plates. Each einzel lens assembly is formed by a set of three concentric cylindrical electrodes, machined from 304 stainless steel, with an inner diameter of 20 mm and length of 15 mm. The electrodes in the einzel lenses are insulated from each other electrically with threaded ceramic standoffs, that create a distance of 1.7 mm between each electrode.

The X-Y steerers and einzel lenses are mounted onto a 120 mm diameter stainless steel plate, referred to hereafter as the Ion Optics support plate, with an electrically isolated 2 mm

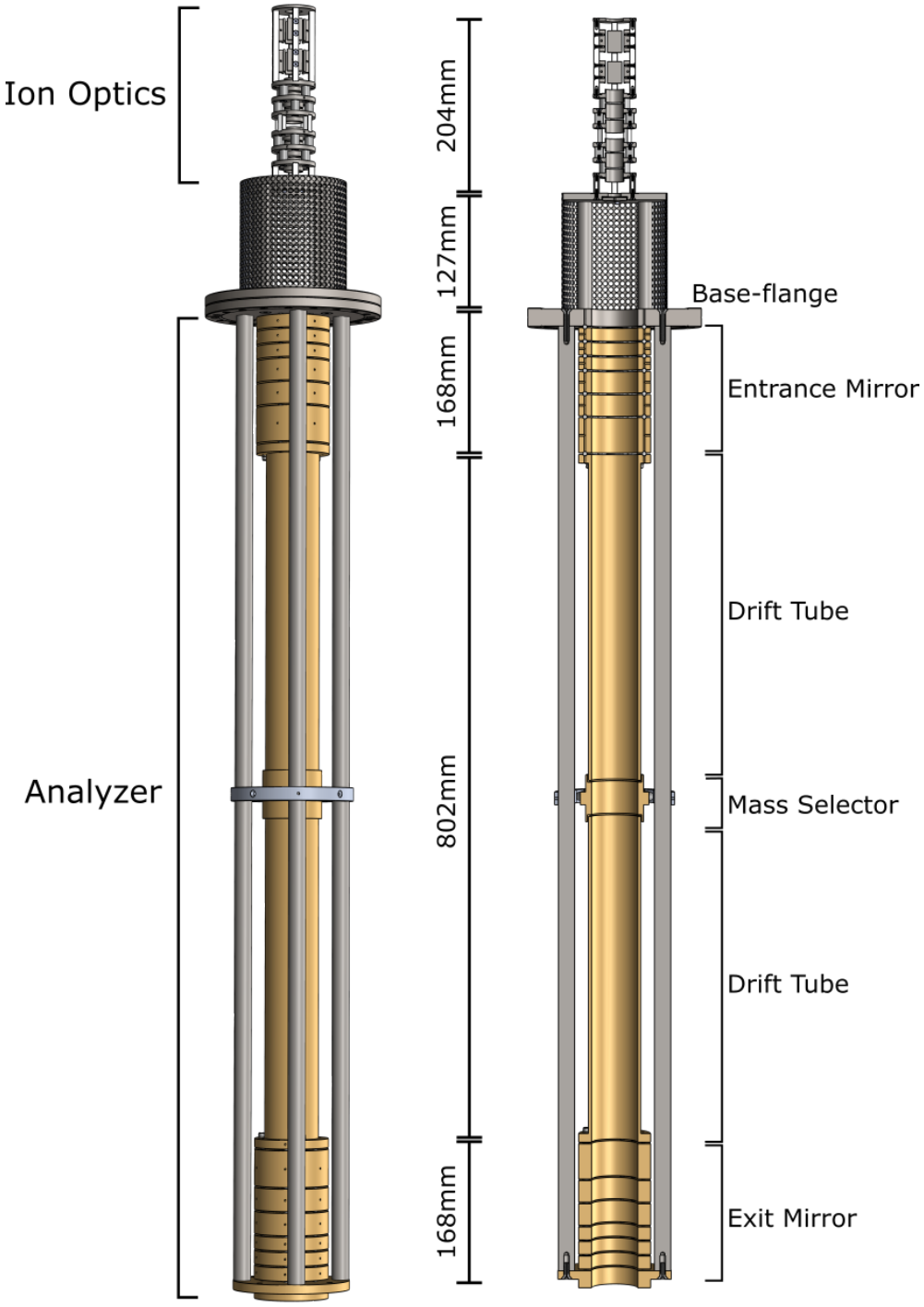

Figure 5.7 3D model of the MRTOF Ion Optics and Analyzer assembly. The assembly is shown on the left and a sectioned view is shown on the right.

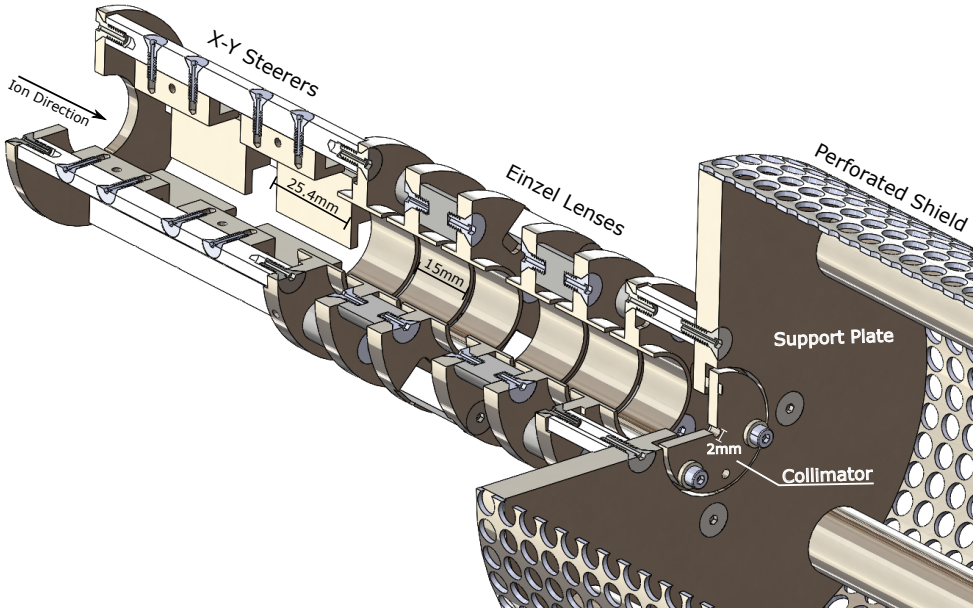

Figure 5.8 Cross-sectional view of the MRTOF's Ion Optics. X-Y steerers are used to steer the ion beam onto the MRTOF's optical axis, with the einzel lenses used to focus the beam.

diameter aperture in the center called the collimator. There is a 127 mm gap between the Ion Optics support plate and the double-faced flange, to allow a Faraday cup to be inserted into and retracted from the optical axis. A perforated stainless steel mesh is used to shield ions from electric fields created by bare wires that supply HV to the Ion Optics electrodes, as they travel from the collimator to the MRTOF entrance mirror. The Faraday cup consists of a stainless steel cup, which is used to catch ions and measure the resulting current. The cup lies within and is electrically insulated from a grounded cylindrical shield. There is a 2.5 mm diameter aperture in the shield to let ions into the cup. A diagram of the Ion Optics is shown in Fig. 5.8 with ions entering the X-Y steerers from the left. The MRTOF mirror electrodes are not shown but are on the right.

The Analyzer sub-assembly consists of two electrostatic mirrors on either side of a central drift-tube, as well as a mass-selector at the center of the drift tube. Each electrostatic mirror assembly consists of 6 electrodes, which are spaced 2 mm apart by 5 mm diameter alumina oxide balls. The ceramic balls are cupped on each side by chamfered holes in the adjacent electrode faces, as shown in a cross-section of the entrance mirror in Fig. 5.9. There are 6

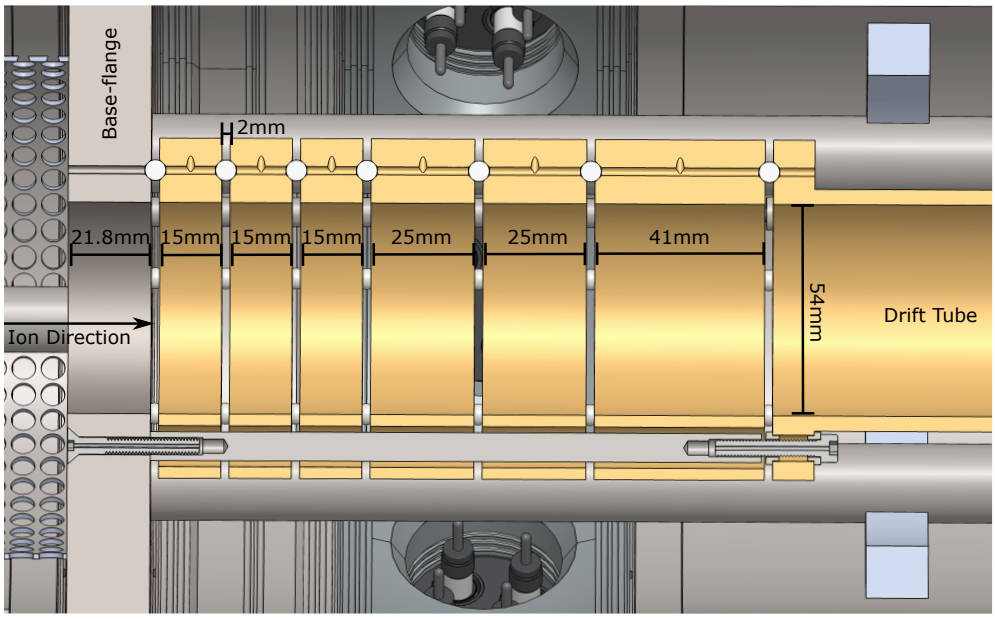

Figure 5.9 Cross-sectional view of the MRTOF's electrostatic entrance mirror. The two electrodes adjacent to the drift-tube are used to steer ions in a point-to-parallel configuration, with the remaining four electrodes used to reflect ions.

alumina oxide balls between each of the electrodes, and the electrode stack is clamped on both sides by fasteners that thread into 3 stainless steel rods which run through the electrodes. One half of the drift-tube is attached to each mirror stack, and the drift-tube segments are electrically insulated from the vacuum chamber with ceramic hat washers.

The mass selector is formed by a 37 mm long cylindrical segment at the center of the drift-tube, with two electrically isolated halves that can be switched to a bias to destabilize ions other than the ions of interest during their passage. The electrodes of the mass selector are connected to an aluminium ring with ceramic standoffs. Set screws in the aluminium ring are used to position the mass selector along four 111 cm long stainless steel rods. The exit mirror assembly is mounted on the 111 cm stainless steel rods such that it faces the entrance mirror assembly. The electrodes in both mirror assemblies, the mass selector, and the drift tube are machined from 6061 aluminium to reduce the weight and plated in gold to avoid patch-potentials.

The vacuum chamber for the MRTOF is formed by three DN160CF 6-way crosses from Kurt J Lesker [1], that house the LAS, Ion Optics and TOF detector. The LAS cross is similar to the original LAS layout discussed in Chapter 4, containing a 90° quadrupole bender and an ion source with a multi-element target. Another 6-way cross is attached to the LAS cross to house the Ion Optics sub-assembly. This cross contains the Faraday cup, which is mounted onto a push-pull linear actuator with 50 cm travel range. The linear actuator is positioned to push the Faraday cup into a small gap between the wall of the cross and the Ion Optics support plate. Attached to the other end of the Ion Optics cross is the MRTOF base-flange. A Kimball spherical octagon [2] is connected to the base-flange, that supports up to 8 DN40CF flange connections. SHV-5 feedthrus with 4 conductors are attached to each DN40CF flange, to support up to 32 electrode connections for the Analyzer and Ion Optics. Since both the base-flange and spherical octagon are threaded, a Kimball close-coupler [3] is needed to couple them.

The MRTOF Analyzer is housed in a 940 mm long full nipple, which is attached to the spherical octagon. The other end of the full nipple is attached to a 6-way DN160CF cross that houses the TOF detector. The 3D model of the MRTOF in the vacuum chamber is shown in Fig. 5.10.

1. Model number: C6-0800.
2. Model number: MCF800-SphOct-G2C8.
3. Model number: MCF800-ClsCplr-G1r1.

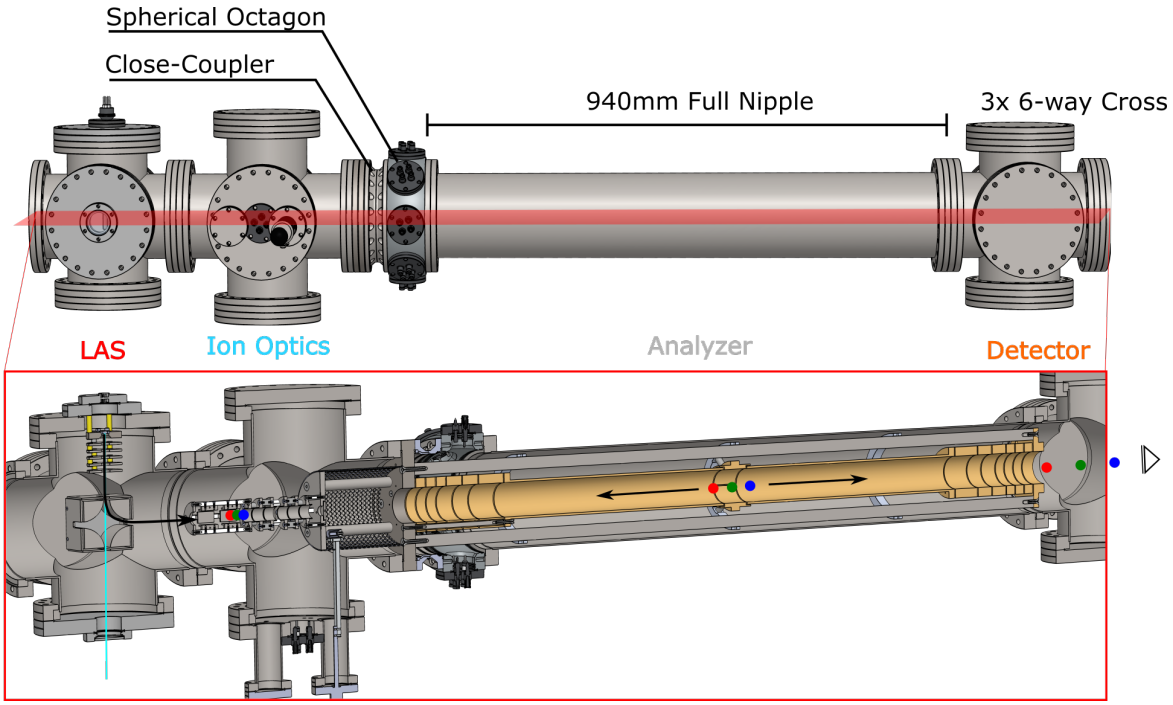

Figure 5.10 MRTOF installed in the vacuum chamber (turbo pumps are not shown). The vacuum chamber assembly is shown on the top while a sectioned view is shown at the bottom. The top view is sectioned along the plane indicated in red.

Chapter 6

MRTOF Assembly

After a few revisions of the technical drawings, the MRTOF optics were machined through the machine-shop at Université de Montréal (UdeM) during the winter of 2019. Technical drawings for all components of the MRTOF Ion Optics and Analyzer are given in Appendix B.

The assembly of the MRTOF took place over a few months during the Summer and Fall of 2020. By December 2020, all major components of the system had been installed and the vacuum chamber was sealed for the first pump down. Commissioning of the MRTOF was paused during the Winter of 2021 to finalise the publication of the LAS manuscript. Once the LAS manuscript was submitted in Fall 2021, the original LAS system was decommissioned and the Spectra Physics UV laser was incorporated into a new LAS system for the MRTOF that was used to commission the system.

6.1 Clean Assembly

All components inside the vacuum chamber were cleaned for UHV, first by a light scrubbing with a soap solution (simple-green) followed by rinsing with water, then a 30 min sonicator bath in acetone, followed by another 30 min bath in isopropanol.

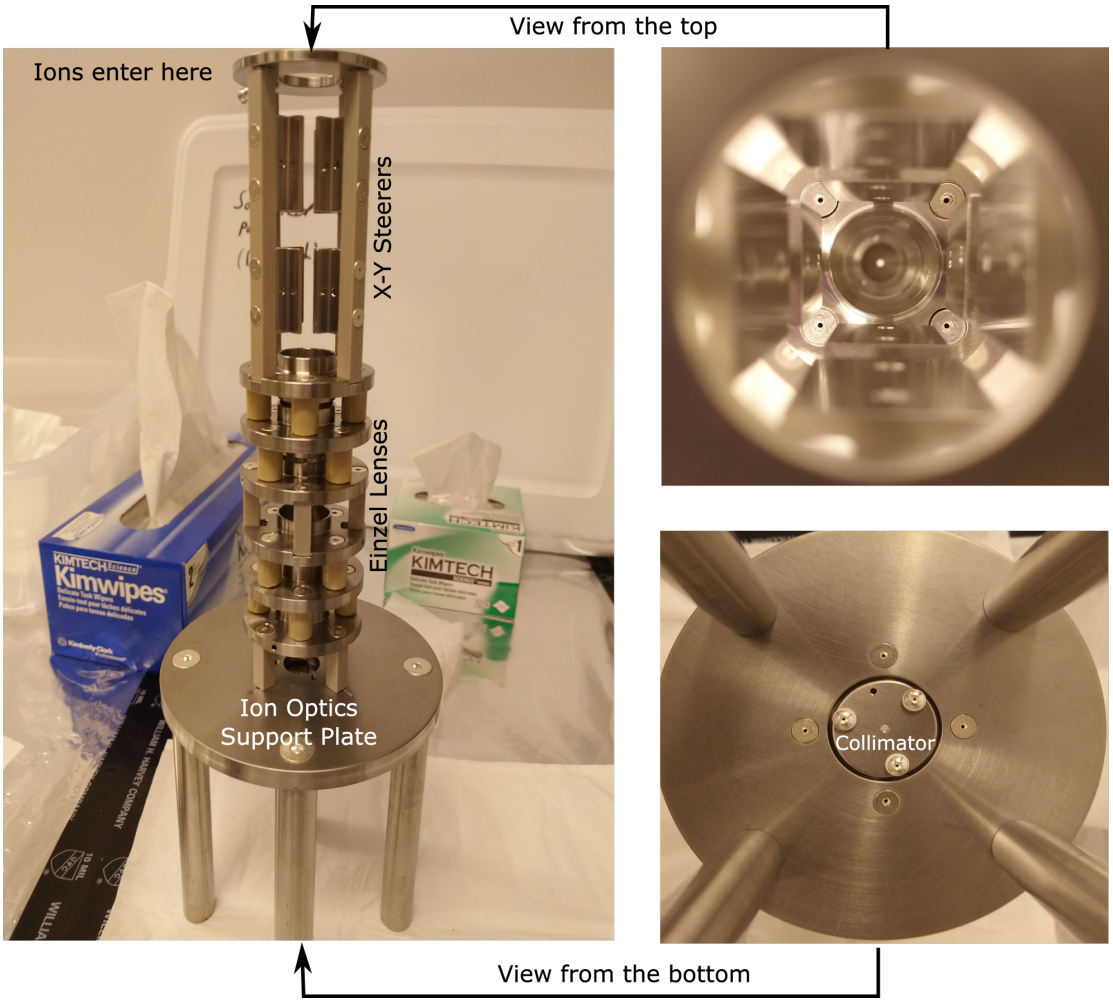

Figure 6.1 Pictures of the Ion Optics clean assembly, where ions enter from the top of the assembly near the X-Y steerers and exit through the collimator aperture.

To assemble the Ion Optics, for which the 3D model was shown in Fig. 5.8, the stainless steel support rods and collimator plate were mounted onto the optics support plate. Then the Ion Optics were assembled as a stack, starting with the einzel lenses, which were mounted lens by lens onto the support plate followed by the x-y steerers. The full clean assembly of the Ion Optics is shown in Fig. 6.1.

Each electrostatic mirror set of the MRTOF Analyzer was assembled separately by stacking electrodes on the base-flange, in the case of the entrance mirror, and on the end-cap electrode, in the case of the exit mirror. One half of the drift tube was fastened to each electrostatic

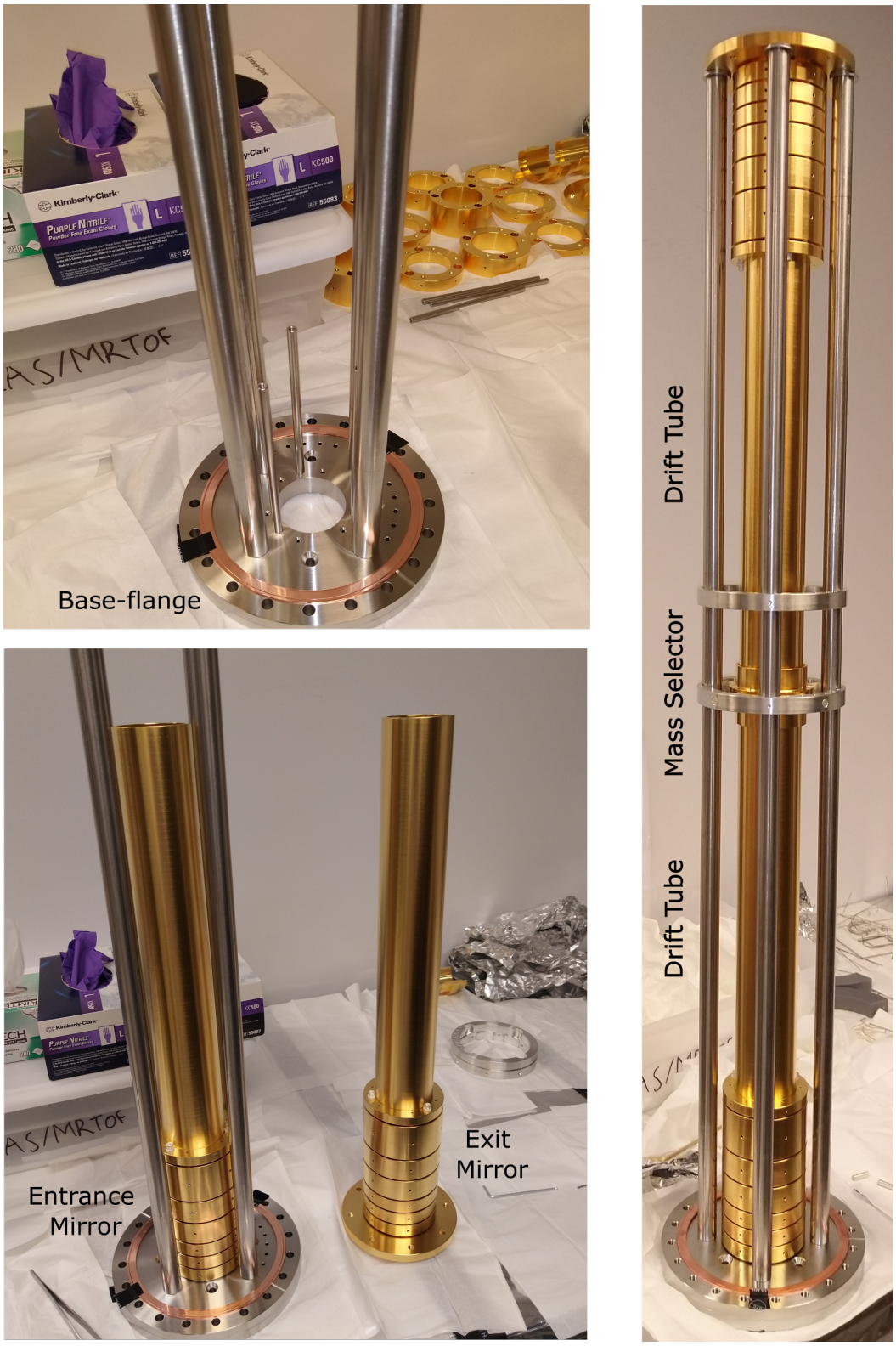

Figure 6.2 Pictures of the assembly of the MRTOF Analyzer. (top left) Support rods are attached to the base-flange to begin stacking the mirror electrodes. (bottom left) The entrance and exit mirror assemblies are assembled separately. (right) The fully assembled MRTOF Analyzer.

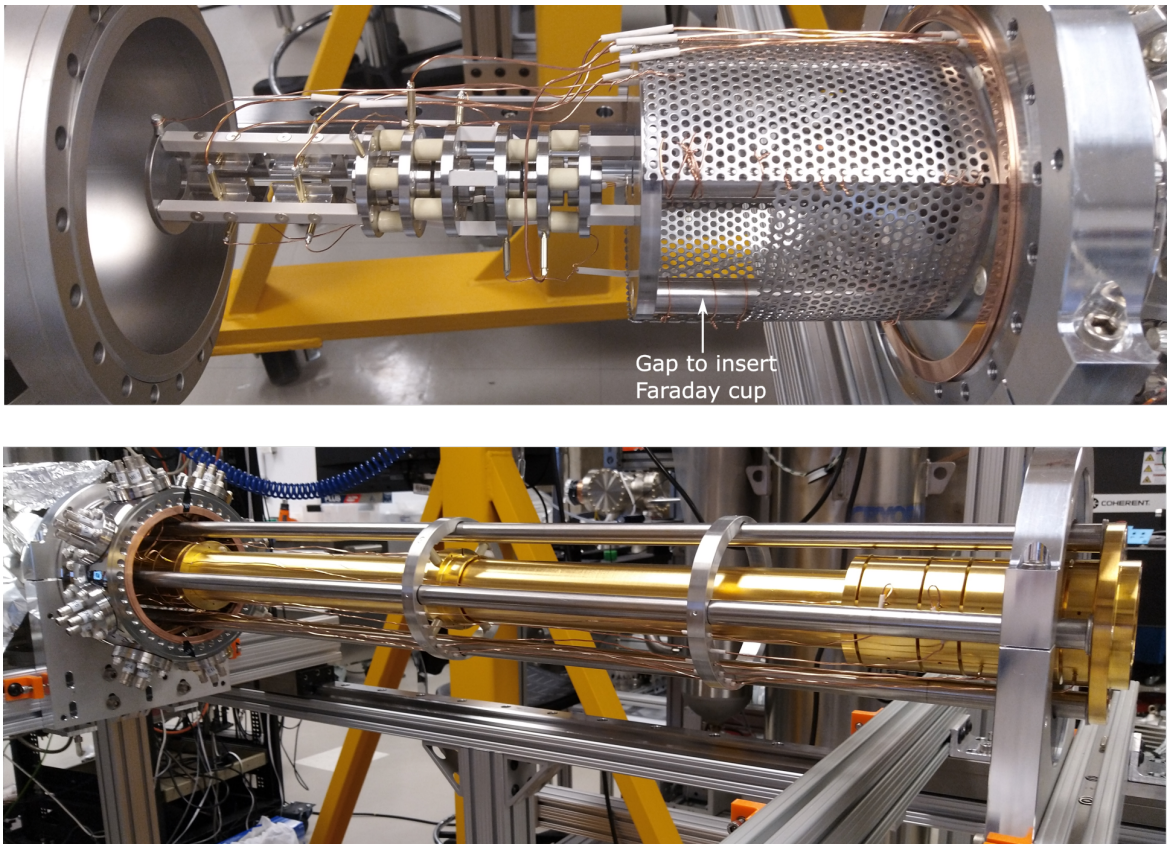

Figure 6.3 (top) Picture of the MRTOF Ion Optics, where a stainless steel mesh shields ions from electric fields created by the copper wires connecting the electrodes. A gap was cut into the mesh to allow a Faraday cup on a linear motion actuator to be temporarily moved into the ion beam path as a diagnostics tool. (bottom) Picture of the Analyzer mounted onto the rail system, with the exit mirror assembly supported by a 3D printed collet.

mirror, as shown on the bottom left in Fig. 6.2. With both halves of the Analyzer assembled, the mass selector was then assembled and slid into place, followed by the aluminium wire guide. Finally, the exit mirror assembly was mounted onto the support rods, completing the assembly of the Analyzer. A picture of the completed analyzer assembly is shown on the right in Fig. 6.2.

The MRTOF Analyzer was then mounted onto the rail system, by clamping the base-flange in an aluminium flange clamp, with the exit mirror supported in a 3D printed collet which was also held by a custom flange clamp. The Ion Optics assembly was then mounted onto the reverse side of the base plate flange. With the Ion Optics attached, the Kimball DN160CF

close-coupler and spherical octagon were mounted onto the Analyzer side of the base-flange. The electrodes of the Analyzer and optics were connected to 4-pin SHV-5 feedthrus mounted onto the spherical octagon with 1.3 mm diameter oxygen-free high thermal conductivity (OFHC) bare copper wire. The wires were connected to the electrodes with 2 mm gold-plated banana jacks, and connected to the vacuum side of the SHV feedthrus with beryllium copper push-on contacts from Accu-Glass [1]. Nonporous alumina ceramic tubes, with an ID of 1.6 mm, were cut into $\sim$ 25 mm long segments with a Dremel tool equipped with a diamond coated cutting wheel. The ceramic tube segments were used to isolate the bare wires from the vacuum chamber and wire-guides.

With all electrodes wired and checked for short-circuits between each other and the vacuum chamber, a DN160CF 6-way cross was attached to house the Ion Optics assembly. Then the 3D printed collet supporting the exit mirror was removed from the flange clamp. After which the 99 cm long full nipple was slid into position over the Analyzer and attached to the spherical octagon. With the 99 cm nipple attached, the MRTOF was ready for alignment with a visible laser as outlined in section 6.2.

After the alignment process, a 6-way DN160CF cross was connected to the 99 cm nipple to house a channeltron ion detector [2]. The base of the channeltron was mounted onto 3 stainless steel rods which were 88.9 mm in length and connected to a DN63CF flange. The channeltron assembly was connected to a DN160CF to DN63CF zero length reducer (ZLR) flange directly opposite the MRTOF's exit mirror, as shown in Fig. 6.4. Another 6-way DN160CF cross was connected to the Ion Optics cross housing a vacuum LAS to provide ions for the MRTOF consisting of an ion source and 90° quadrupole bender. The quadrupole bender assembly was mounted onto the underside of a DN160CF to DN40CF ZLR flange, which during assembly was clamped horizontally in a flange clamp mounted onto an optical table, as shown on the left in Fig. 6.5. The quadrupole electrodes and box are connected to

1. Model number: POC94-5.
2. Detech model number: 402A-H3.

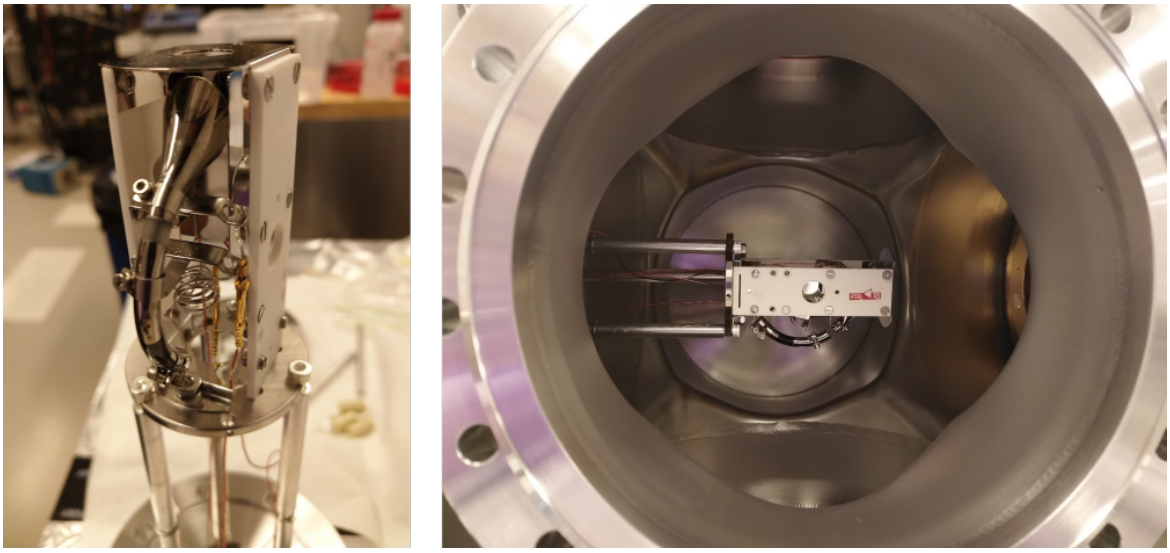

Figure 6.4 (left) Assembly of the channeltron. (right) Picture of the channeltron installed in the cross. The golden reflection of the exit mirror is visible on the right side. Ions will hit the channeltron detector from the right.

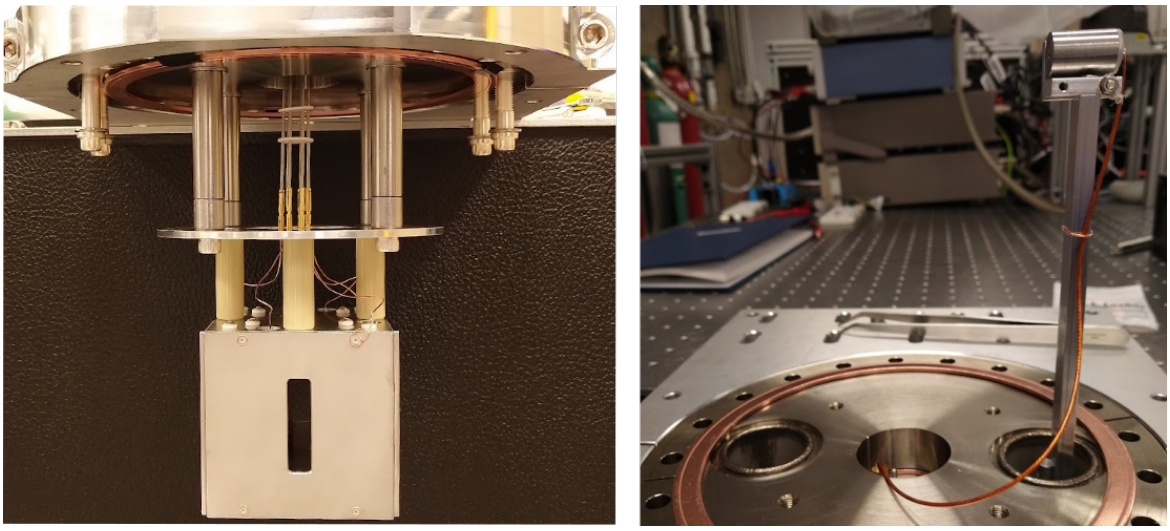

Figure 6.5 (left) Picture of the quadrupole bender mounted in a flange clamp during the assembly process. (right) Picture of the Faraday cup during the assembly process.

a 6-pin feedthru from Lesker [3] with bare OFHC copper wire and beryllium copper socket contacts from Accu-Glass [4]. The quadrupole bender was installed on a rotatable flange of the LAS cross, to allow for adjustment of the angle between the bender and the ion source.

The Faraday cup assembly was mounted onto a DN40CF push-pull linear feedthru with a 50 cm travel range from Accu-Glass, and is shown on the right in Fig. 6.5. The cup was connected to a DN40CF 4-pin SHV feedthru with Kapton insulated stranded core wire. The Faraday cup was then slid carefully into place, through the gap in the mesh shield as shown on the top in Fig. 6.3.

6.2 Laser-based electrode alignment

Despite the fact that aluminium electrodes were used for the analyzer electrodes, the weight of the assembled electrode stack caused the free hanging end of the Analyzer to sag. To correct this, the free hanging end of the Analyzer was supported with aluminium as well as sheets of 0.25 mm thick stainless steel shim material, which was placed between the end-cap electrode and the inner wall of the 99 cm nipple. A laser alignment system was used to determine the optimal height of supporting material for alignment of the exit mirror with the MRTOF's optical axis.

The laser alignment system was deployed on a 152×152 mm aluminium optical breadboard, which was mounted onto the wall opposite the MRTOF's exit mirror. A PL202 635 nm 0.9 mW continuous wave laser from Thorlabs defined the optical axis for the MRTOF. A 1 mm diameter aperture [5] was used to reduce the laser beam diameter, after which the laser path was adjusted using a two-mirror [6], mirror walk configuration as shown in Fig. 6.6. Two black PLA 3D printed inserts were used to create 2 mm diameter apertures in entrance and exit mirrors. The inserts were designed such that the 2 mm apertures were concentric with

3. Model number: TFT3EP00003.
4. Model number: BECUGS-056-5.
5. Thorlabs model number: P1000D.
6. Knight Optical square mirrors, model number: MGM2502.

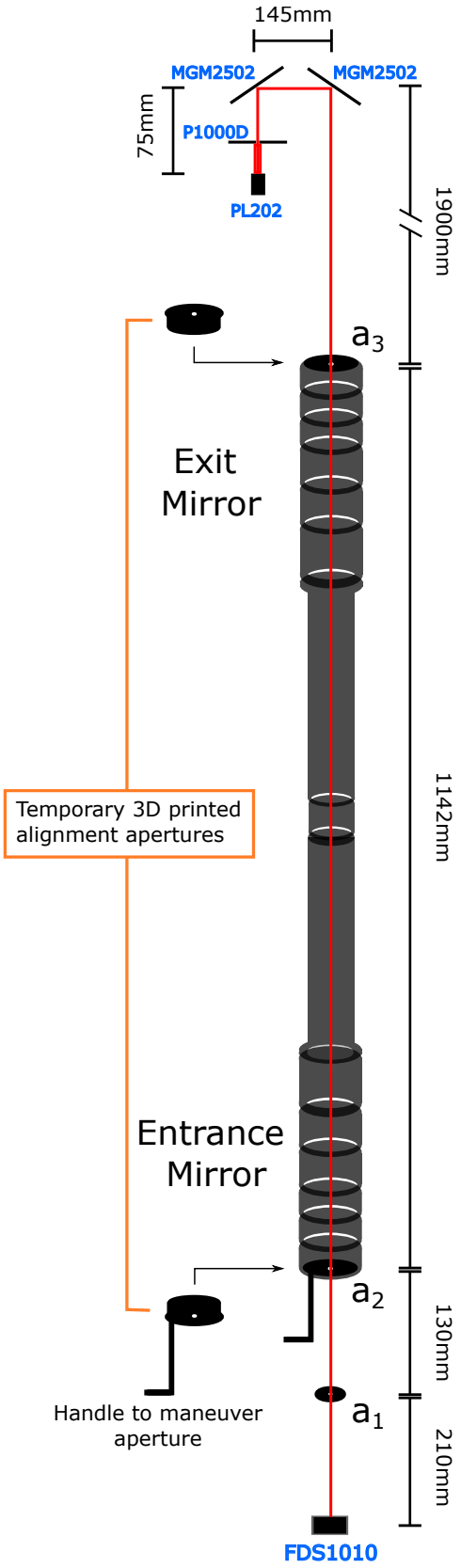

Figure 6.6 Schematic of the laser alignment system for the MRTOF, with which the height of the exit mirror was adjusted for coaxial alignment with the entrance mirror. The PL202 laser emitted a red beam, indicated by a red line.

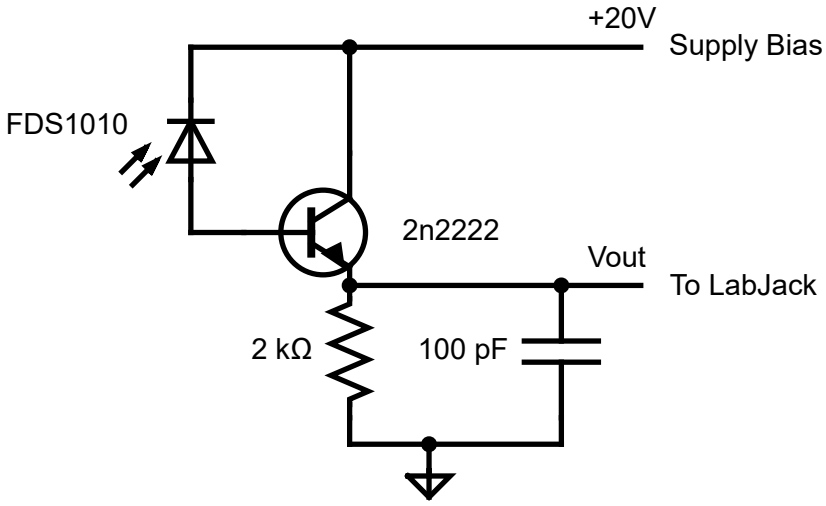

Figure 6.7 A BJT amplification circuit for the FDS1010 photodiode, where the voltage output was measured with a Labjack T7.

the electrodes of the mirror assemblies and also so that they could be removed after the alignment process. The 3D printed inserts for the entrance and exit mirrors were labelled a_2 and a_3 respectively. A third 2 mm diameter aperture, labelled a_1, was created by the collimator plate which was inset into the Ion Optics support plate, which can be seen on the bottom right of Fig. 6.1. The intensity of laser light was measured with a Thorlabs FDS1010 photodiode, which had an active area of 10×10 mm. The responsivity of a photodiode is defined as the ratio of photocurrent, I_P, to incident optical power, P, following

$$R_\lambda = \frac{I_P}{P}. \tag{6.1}$$

The responsivity of the FDS1010 at 635 nm is $R_\lambda = 0.37$ A/W, thus the PL202 laser could produce a maximum photocurrent of $I_P \approx 0.3$ mA. The photodiode was connected in reverse bias, with the anode connected to the base of a 2n2222 bipolar junction transistor (BJT) for amplification of the photocurrent. The photodiode response was measured as an output voltage across a 2 kΩ resistor, as shown in Fig. 6.7, which was recorded with a T7 LabJack.

The height of the exit mirror was adjusted to maximize the photodiode response with all three targets in place. For the best alignment configuration, measurements of the signal

Table 6.1 Measurements of the photodiode response for the best alignment configuration, for all possible combinations of removable apertures.

Apertures in place	Photodiode response (V)
a1	3.17(1)
a1 + a2	2.91(1)
a1 + a3	3.45(1)
a1 + a2 + a3	3.20(1)

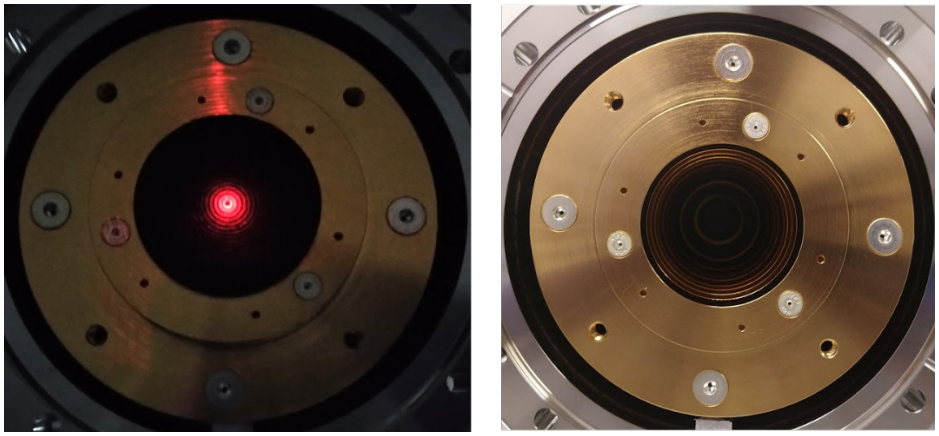

Figure 6.8 (left) Picture of the MRTOF's exit mirror during alignment, where diffraction rings can be seen when the 3D printed aperture was in place. (right) Picture of the exit mirror after the alignment.

response were taken for different combinations of apertures, displayed in Table 6.1, although the collimating plate could not be removed. The photodiode response increased unexpectedly when inserting a_3, the exit mirror aperture. One possibility is that this could be due to the blocking of diffraction rings that would otherwise reflect off of the inner walls and cause destructive interference. The diffraction rings can be seen on the left of Fig. 6.8, and are most likely created by the diffraction of laser light through the 1 mm diameter aperture placed after the laser. For all combinations of apertures, the photodiode response was within 10% of the response when only the collimating aperture was in place.

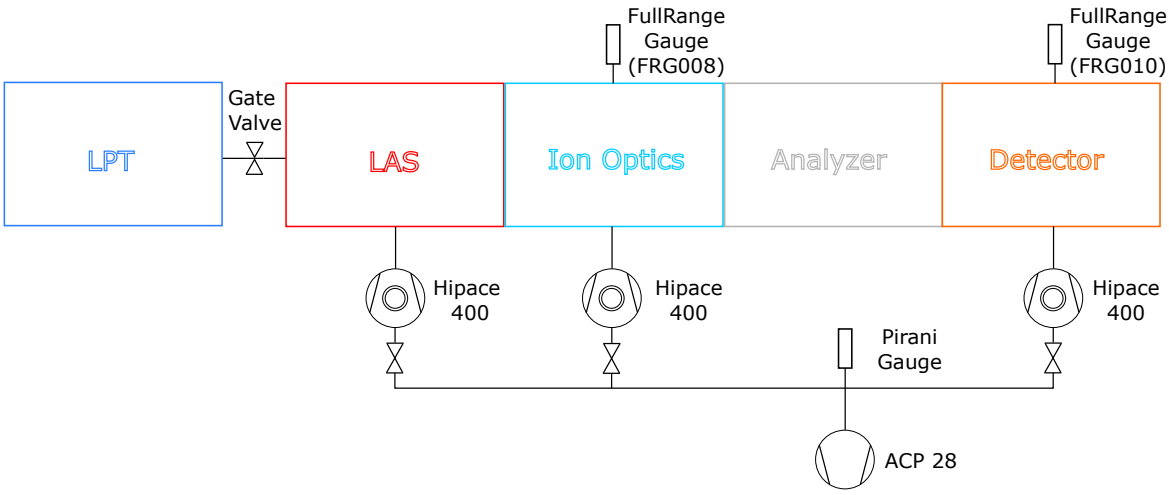

Figure 6.9 Schematic of the vacuum system, where 3 TMPs are used to reach UHV.

6.3 Vacuum system and initial pump down

All flanges in the MRTOF vacuum chamber are CF UHV, which create a metal-to-metal seal using knife-edges that make an annular groove on either side of a soft copper gasket. Using a torque wrench, all DN160CF and DN63CF flanges were tightened to 20 N-m and DN40CF flanges to 16 N-m. A Pfeiffer ACP 28 roughing pump was used to create a fore-vacuum and UHV was achieved using 3 Hipace 400 turbomolecular pumps (TMPs) mounted on the LAS cross, the Ion Optics cross and the channeltron cross as shown in Fig. 6.9. A pirani gauge was used to monitor the pressure in the lines between the ACP and the TMPs, after which the valves between the ACP and TMPs were slowly opened.

The pressure inside the vacuum chamber was monitored with 2 Pfeiffer PKR360 full range gauges, which were connected to the Ion Optics cross and the channeltron cross. Measurements from the full range gauges were read out using a TPG366 gauge controller which was accessed over ethernet by a custom LabVIEW program to save pressure data during the pumpdown. With the valves between the ACP and TMPs open, the system reached a fore-vacuum of 1×10^{-1} Torr, as shown in Fig. 6.10. Once the TMPs were turned on, the system reached a pressure of 1×10^{-6} Torr within the first few minutes and 1×10^{-8} Torr

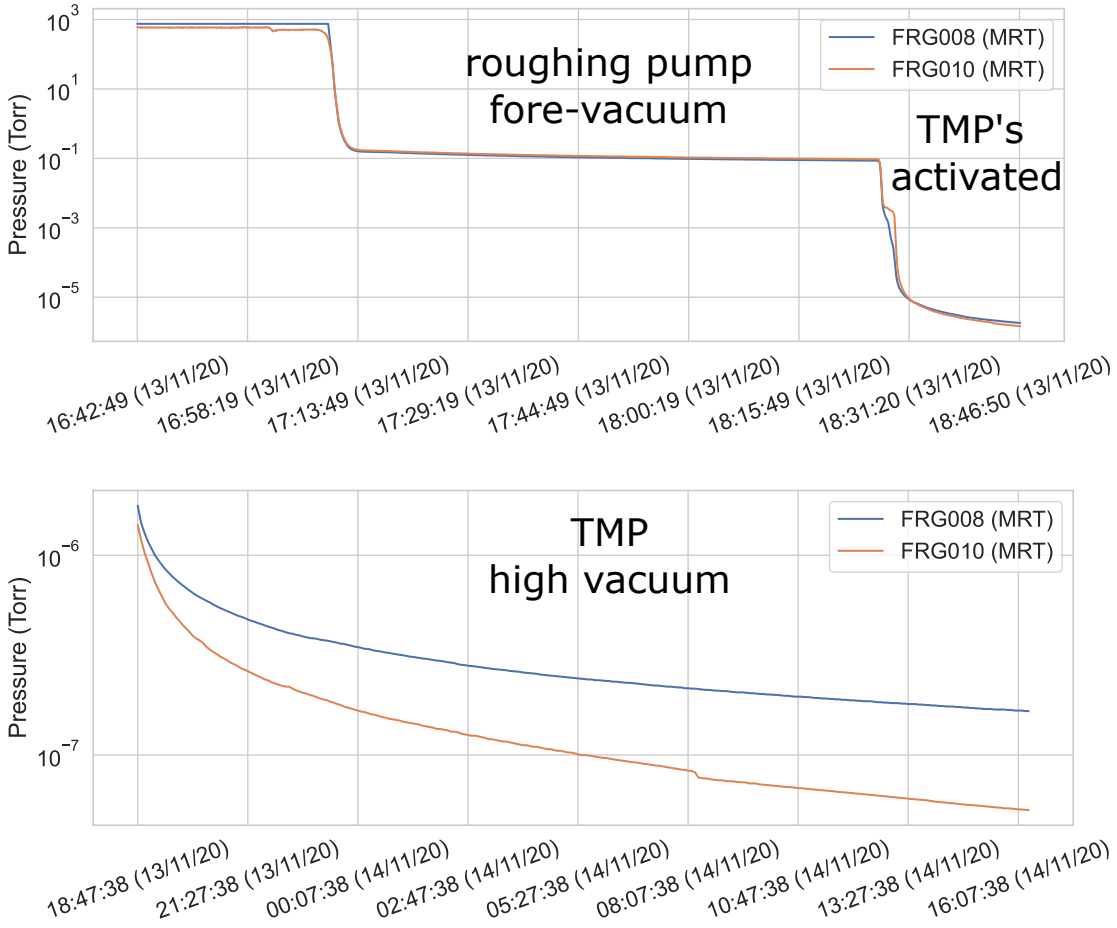

Figure 6.10 Plot of system pressure during pumpdown, with high vacuum reached within hours and ultra-high vacuum reached after ≈ 2 weeks.

after a few days. The typical system pressure, if the gate valve to the LPT was closed, was $< 1 \times 10^{-9}$ Torr measured at both gauges.

Chapter 7

Commissioning of the MRTOF

After the MRTOF system had been assembled, aligned, and pumped down to UHV, the commissioning process began. A new LAS, based on the design discussed in Chapter 4, was created to supply bunched ions to the MRTOF while the LPT was being commissioned. The work to follow will discuss the commissioning of the MRTOF with ions produced by the LAS.

In a typical measurement cycle of the MRTOF, the ion start time was set by the laser pulse signal, which was used to start a timing sequence controlled by a field programmable gate array (FPGA). The FPGA then sent TTL signals to High-Voltage (HV) switches, which were used to raise and lower the electric fields of the electrostatic mirrors to let ions in and out of the MRTOF Analyzer. After ions were ejected from the Analyzer, a TTL signal was sent by the FPGA to a digitizer, to record the channeltron signal within an acquisition window. In Section 7.1, the testing of the FPGA, HV switches, and digitizer will be discussed. The layout of the fully assembled MRTOF system is given in Fig. 7.1, showing the locations of the relevant subsystems.

A custom LabVIEW program was developed and used to operate the LAS, HV supplies, FPGA, digitizer, and to record TOF data. The commissioning of the new LAS for the MRTOF with the program will be discussed in Section 7.2. After the electronics and the LAS were commissioned, the MRTOF was used to trap Cu^+ ions from the LAS for up to 15 ms. The

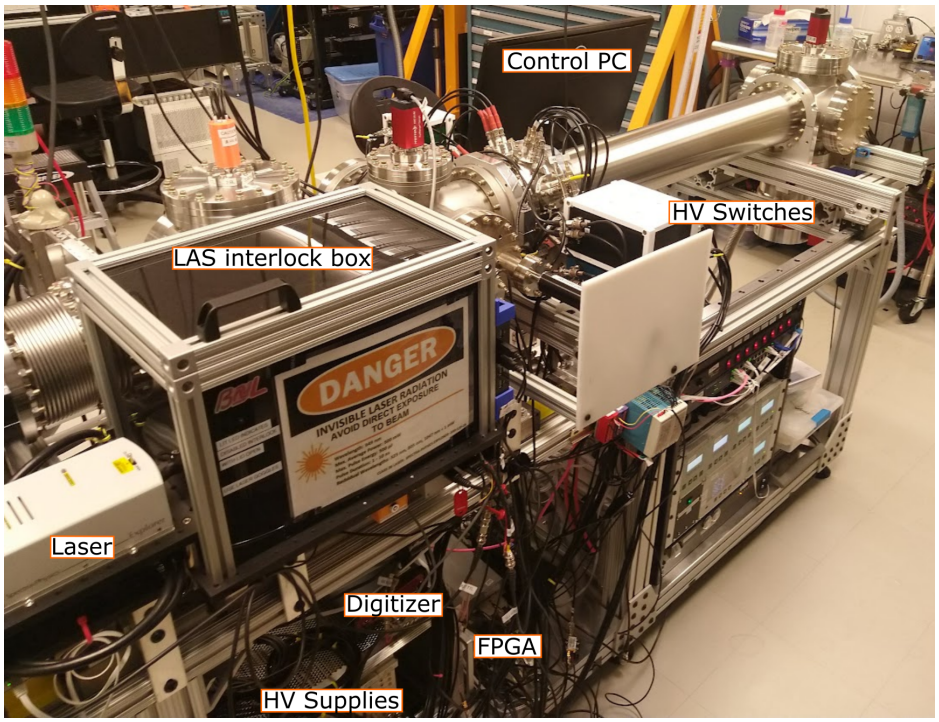

Figure 7.1 Picture of the fully assembled MRTOF system, showing the layout of the electronics used to trap ions and record their TOF during the commissioning.

stable isotopes ^{63}Cu and ^{65}Cu were observed as distinct TOF peaks after 3 revolutions in the MRTOF, which will be discussed in Section 7.4.

7.1 MRTOF Electronics

The timing system is necessary to trigger the HV switches as well as the digitizer, thus it was the first subsystem to be commissioned. Jitter inherent to the timing system was investigated in order to characterize potential sources of uncertainty for ion TOF measurements. The performance of the HV switches was subsequently evaluated, to ensure that the switches were operating within the specifications of the manufacturer.

7.1.1 FPGA timing system

The timing system for the MRTOF is controlled by a FAB-3226 USB-to-FPGA interface, connecting 16 bi-directional IO ports to user defined FPGA logic on a Cyclone IV FPGA

[129]. A C++ program is used to read/write data over a 16 bit data bus from a control PC to the FAB-3226. The FPGA logic, written in verilog, is loaded onto the FPGA as a raw binary file and controls the output bit-pattern according to the user's settings.

A verilog program was written that allows for up to 10 TTL signals to be sent out to the consituents of the MRTOF system, that repeat with a period set by the user. The program increments a timer variable by 1 at a rate of 30 MHz, which is the effective clock speed of the FPGA. Once the timer reaches the given period, it will reset to 0. The program also takes in 10 different start and stop times, in which it will set 10 different bits to high, if the timer is between the two times, or low if it is not. Thus creating 10 configurable TTL signals within the given period. Since the read/write bus can only transfer a maximum of 16 bits, each start and stop time is split into two 16 bit numbers, so that the period and configurable TTL signals are allowed to be 32 bit.

The jitter of TTL signals from the FPGA was measured with an oscilloscope, by measuring the time difference between two pulses over the length of a typical MRTOF measurment cycle of 2-20 ms. The oscilloscope was set to trigger on the first pulse and save the waveform of the second pulse with a time resolution of 40 ps, so that the arrival time of the rising edge of the second pulse could be compared with the expected user-controlled value. The arrival time of the second pulse, t_{p2}, is defined as the midway point between the times at which the TTL signal is at 5% and 95% of its peak value.

A plot of of the time difference between the measured and expected pulse time, t_{p2}-t_{exp}, is shown in Fig. 7.2 as a function of the expected pulse time. Each data point was calculated using the measured t_{p2} values from 20 waveforms, and plotting the mean of those values with the standard deviation as the measurement uncertainty. There was an increasing offset of up to 6 ns over a 20 ms delay, with an increasing jitter of up to 400 ps. The magnitude of the jitter is small by comparison to the FWHM of a typical TOF peak, which is $\sim$100 ns and thus is negligible. In the case of the MRTOF's operation with the LAS, there is a jitter on the

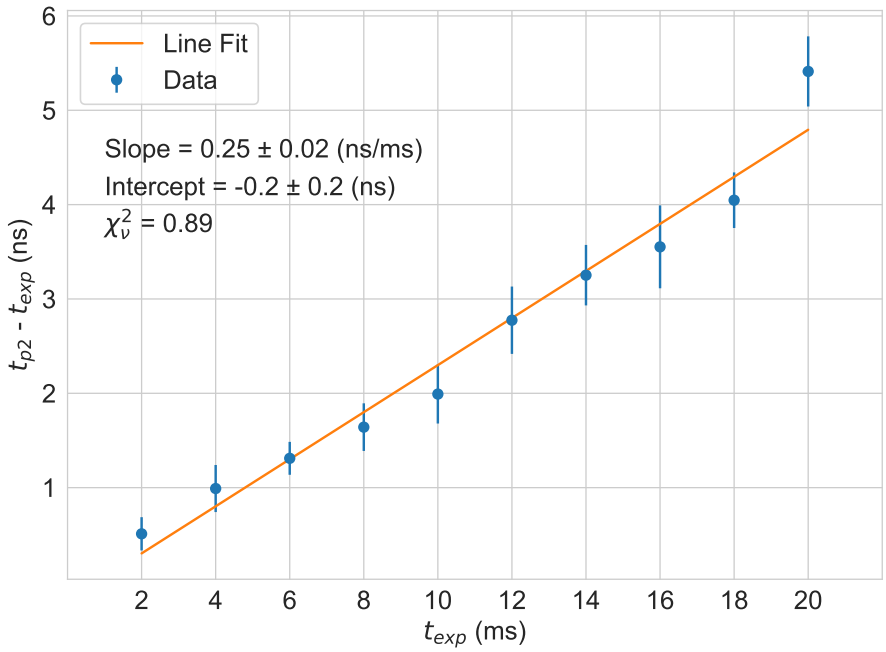

Figure 7.2 A plot of the difference in time between a TTL signal from FPGA and the expected value set by the user.

scale of ∼200 ns [90]. However, the Spectra Physics laser has an OptoSync output which is synchronised with the laser output with a jitter of < 0.5 ns. For this reason the FPGA was configured to allow for an external TTL signal to reset the timer variable and allow $t = 0$ to correspond to the OptoSync pulse. The time resolution with which the FPGA can receive the OptoSync pulse is limited by the inverse of the clock speed at 33 ns, which becomes the dominant source of timing jitter.

Since ion TOF is referenced from an FPGA TTL signal, the linearly increasing offset shown in Fig. 7.2 has the potential to create an offset between the TOF of the analyte ions, t_{an}, and the TOF of calibrant ions, t_{cal}, introducing measurement uncertainty. In principle this effect can be calibrated, however it shall be demonstrated that it is negligible. Suppose that there is an offset between t_{an} and t_{cal}

$$t_{\text{cal}} = k\sqrt{\frac{m_{\text{cal}}}{q}} \tag{7.1}$$

$$t_{\text{an}} = k\sqrt{\frac{m_{\text{an}}}{q}} + \delta t, \tag{7.2}$$

where m_{cal} is the mass of the calibrant ion, and m_{an} is the mass of the analyte ion. After some algebraic manipulation, and assuming that the ions have the same charge, the fractional difference of the measured mass m_{an} can be expressed as a function of δt as

$$\frac{m_{\text{an}}(\delta t) - m_{\text{an}}(\delta t = 0)}{m_{\text{an}}(\delta t = 0)} = \left| \frac{(t_{\text{an}} - \delta t)^2}{t_{\text{an}}^2} - 1 \right|. \tag{7.3}$$

If $t_{\text{an}} \sim$1 ms and $\delta t \sim$1 ns then

$$\frac{m_{\text{an}}(\delta t = 1\ ns) - m_{\text{an}}(\delta t = 0)}{m_{\text{an}}(\delta t = 0)} \approx 1 \times 10^{-6}, \tag{7.4}$$

which is an order of magnitude lower than the MRTOF's anticipated mass resolution.

7.1.2 Power Supplies & Electrode Connections

The MRTOF electrodes were connected to ISEG High Voltage modules installed in an MPOD W-IE-NE-R crate, allowing the bias of each electrode to be controlled over ethernet with proprietary software as well as with custom labVIEW programs. For the analyzer electrodes, ISEG-EHS high precision series modules were used which had a specified voltage ripple < 5 $\text{mV}_{\text{p-p}}$. For the Ion Optics electrodes, ISEG-EBS bipolar modules were used that allowed for up to a 3 kV difference between channels and had a specified voltage ripple < 20 $\text{mV}_{\text{p-p}}$. A list of all high voltage modules used is given in Table 7.1.

On the atmospheric side if the vacuum system, the electrodes were connected to the high voltage modules with SHV RG-58 coaxial cable assemblies, with the exception of the quadrupole bender, which used 0.056" beryllium copper socket contacts on the feedthru end

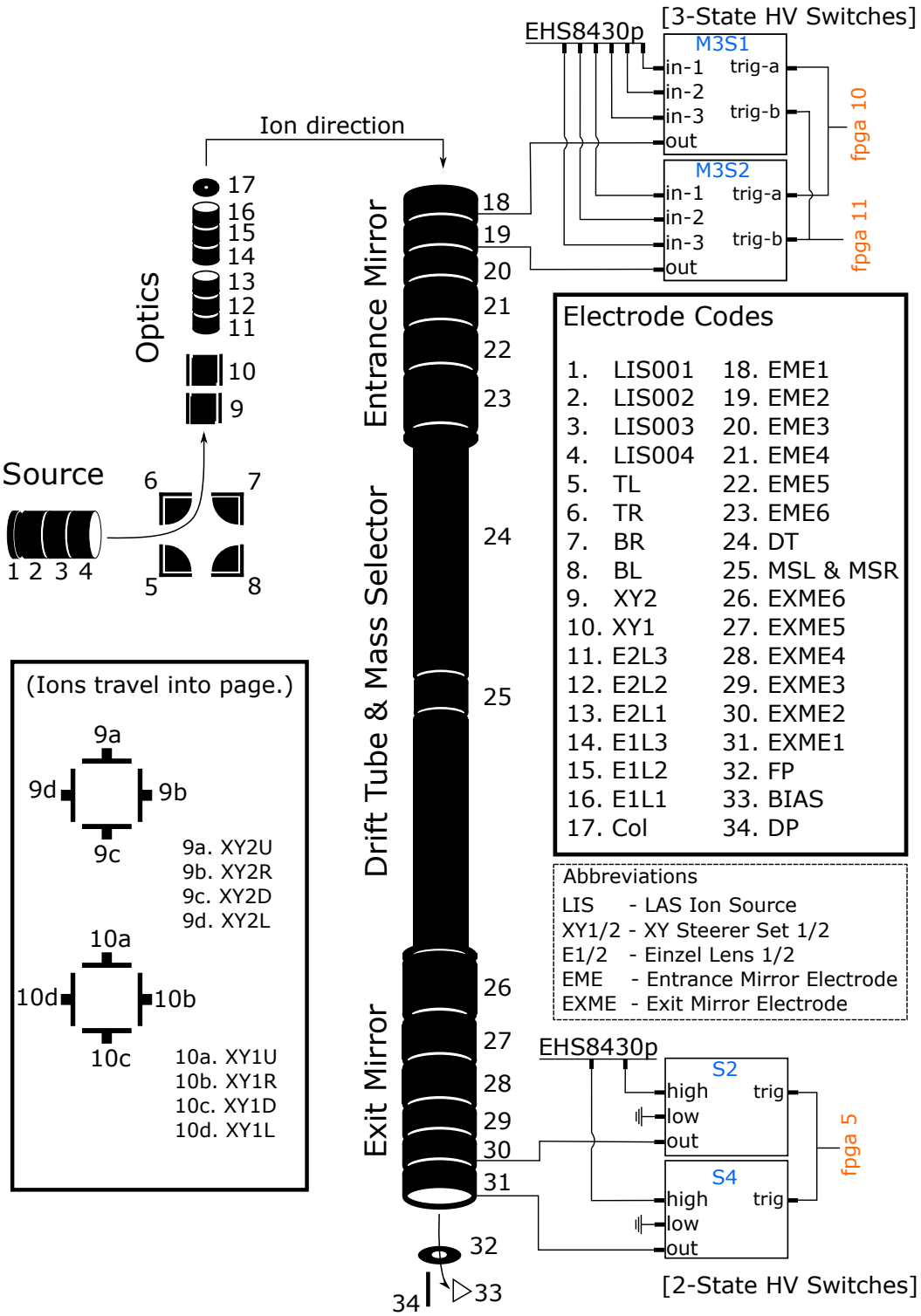

Figure 7.3 Schematic of the MRTOF and LAS, showing all electrodes and their codes. The MRTOF system is all in-line, but is folded in the diagram due to space constraints.

Table 7.1 HV DC power supplies used for the MRTOF mounted in an MPOD W-IE-NE-R crate.

Code	Model	Bias (kV)	Channels	Polarity	Ripple (mV_{p-p})
HVS000	EHS8420p	2	8	pos	5
HVS001	EHS8430p	3	8	pos	5
HVS002	EHS8430n	3	8	neg	5
HVS003	EBSC030	3	12	bipolar	20
HVS004	EBSC030	3	12	bipolar	20

of the cable assemblies. A 3D printed PLA shield was used to cover the exposed pin-to-cable connections of the feedthru for the quadrupole bender. With the exception of the quadrupole bender, all feedthrus used were SHV-5 kV. A full schematic of all the electrodes in the MRTOF and LAS is shown in Fig. 7.3. Each X-Y steerer had 2 adjacent electrodes connected to outputs of a bipolar power supply, while the remaining 2 electrodes were held at ground potential. For each einzel lens assembly, only the middle electrode was biased and the two outer electrodes were also kept at ground potential.

7.1.3 Ion Trapping & HV Switching

The HV switches allow for the biases applied to the outer two electrodes of the entrance and exit mirror assemblies to be switched on an extremely short timescale $\sim$ 100 ns. Two types of HV switch were used that allowed for two or three possible biases for the connected electrode, referred to hereafter as 2-state or 3-state switches respectively. The switching is achieved by using 2 back-to-back 2SK3745LS-1E HV MOSFETs that can block up to 3kV until the switch is opened. The 2-state switches are controlled by a single active-low trigger, while the 3-state switches are controlled by two triggers, referred to as Trig-A and Trig-B. The 3-state switches have 3 valid trigger states (A,B) which are (0,0), (0,1) and (1,0).

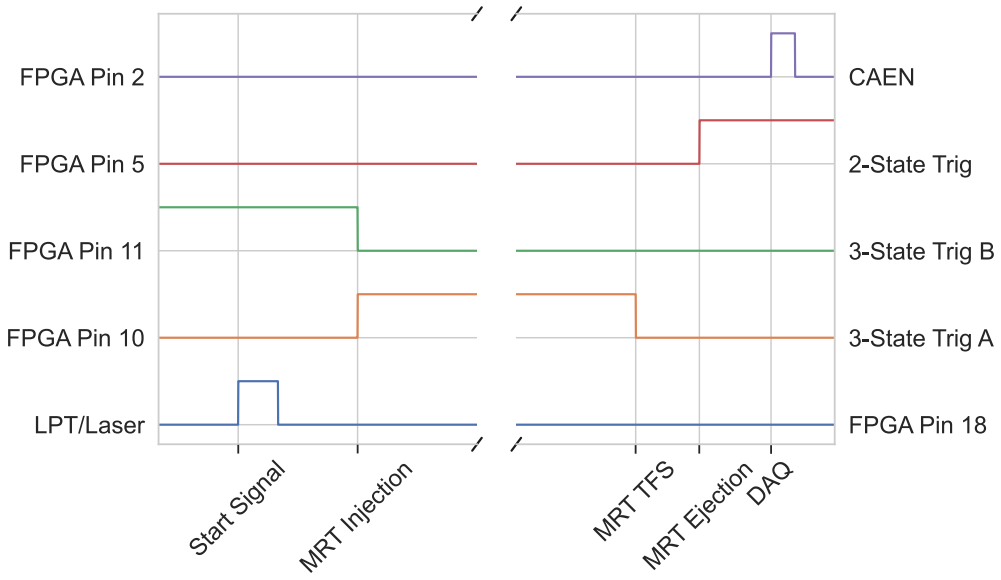

Figure 7.4 Timing diagram of the TTL signals used to operate the HV switches and trigger the digitizer for data acquisition.

In a typical measurement cycle in the MRTOF, the start time is set by an external TTL signal with a jitter of 33 ns. Ions are then trapped within the MRTOF analyzer by the switching of the 3-state HV switches from a low potential to the isochronous reflection setting. Ions are trapped inside the analyzer for $n \times t_{rev}$, where n is the number of revolutions and t_{rev} is the revolution time. Half a revolution before the ejection of ions, the 3-state switches are switched to the TFS setting for the final reflection, in order to shift the time focus onto the detector. At the time of ejection, the 2-state switches are switched to a low potential so that ions may exit the analyzer. After ejection from the analyzer, a TTL signal is sent to a CAEN digitizer [1] to record the TOF of the ions. The sequence of TTL signals used to trap ions and record TOF data for a typical measurement cycle is shown in Fig. 7.4.

The HV switches were tested with input from the EHS8430p ISEG module, where the trigger states were controlled by the FPGA. The HV switching for each switch was measured with a PR2000B BK precision 100:1 probe, between the switch output and the mirror electrode. A second PR2000B probe was used to simultaneously monitor the HV input to the switch. It

1. Model number: DT5751.

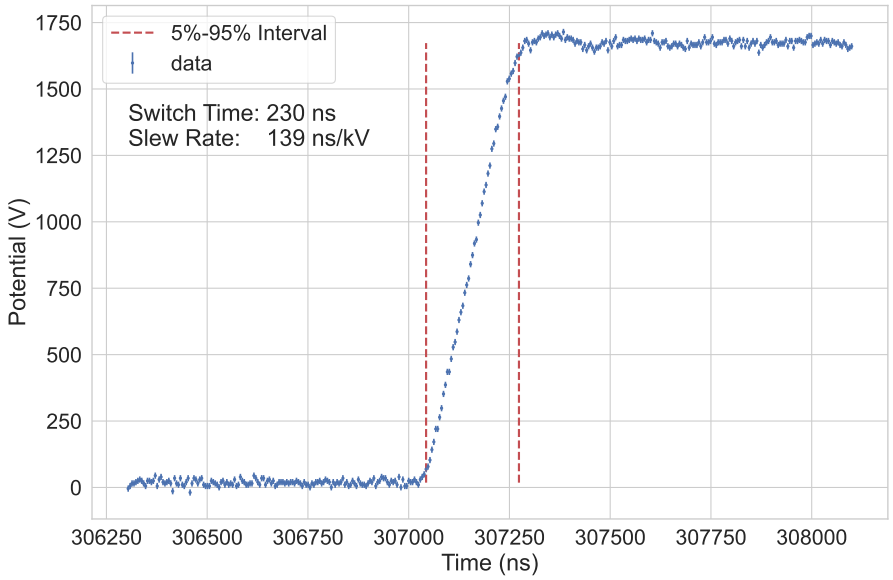

Figure 7.5 Measurement of the slew-rate for a 2-State HV switch, which was consistent with the manufacturer specifications.

was apparent that the buffer capacitors in the HV module were not large enough to support the capacitive load of the mirror electrodes, which resulted in a dip of the input voltage of $\sim 100-200$ V and a 're-charging' effect over a few 100 μs. The timescale of this 're-charging' effect was long enough that ions would see a changing electric field in the entrance mirror for the initial reflections. To resolve this, as suggested by the switch manufacturer, low pass RC filters were added to the switch inputs. The RC filters consisted of a 1 MΩ resistor and a 1 μF polypropylene capacitor rated to 3 kV DC.

The switch transition time was measured as the interval in which the signal was between 5% and 95% of the maximum signal value. For the 2-state switch the transition time was measured as 139 ns/kV and for the 3-state switch it was 392 ns/kV, which is within the expected 70-200 ns range for the 2-state switch and $<$ 500 ns as specified for the 3-state switch. These measurements are shown in Fig. 7.5 and 7.6, for typical switch transitions during injection and ejection of ions.

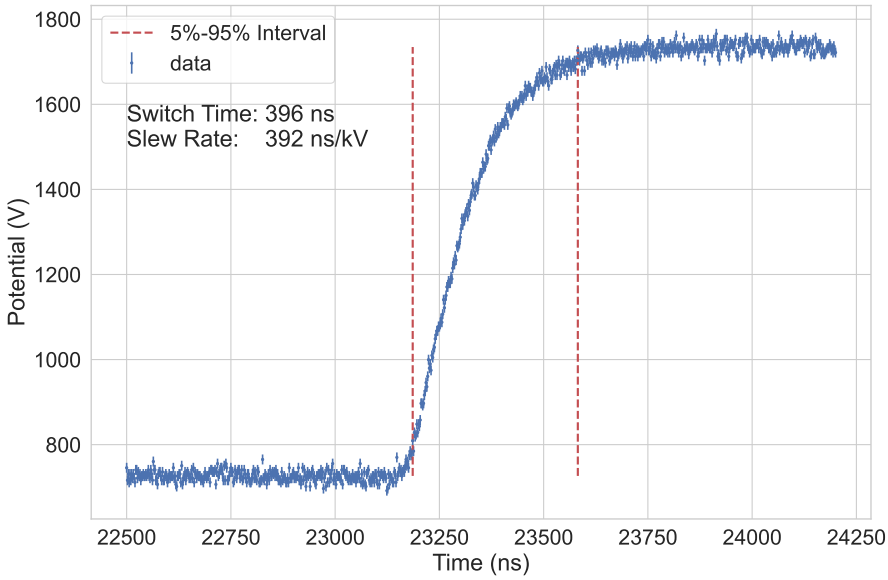

Figure 7.6 Measurement of the slew-rate for a 3-State HV switch which was slower than the 2-state switch, since there is an extra state available, but still consistent with the manufacturer specifications.

7.1.4 TOF Data Acquisition

A channeltron TOF detector was used for the detection of ions during the commissioning of the MRTOF. A channeltron is a horn-shaped funnel of glass, coated in a thin film of semi-conducting material [130]. A negative bias of $\sim$-2 kV is applied to the opening aperture of the channeltron, that accelerates secondary electrons produced by impinging ions to the tail end of the funnel which is held at ground potential. The accelerated electrons have enough kinetic energy to create more secondary electrons upon impact with the funnel walls, thus a cascade effect is achieved. The gain of a channeltron is defined as the ratio of the output current to the input current, which was $\times 10^7$ for the model used. A channeltron can detect single ions with a detection efficiency of up to 90% [131].

The channeltron signal was amplified by a ZX60-100VH +15dB amplifier and subsequently digitized by a CAEN DT5751 10 bit 1 GS/s digitizer. The digitizer was triggered by an external TTL signal from the FPGA, and set to record ion signals in an acquisition window after the ejection of ions from the analyzer. The TTL signal that triggered the CAEN was also

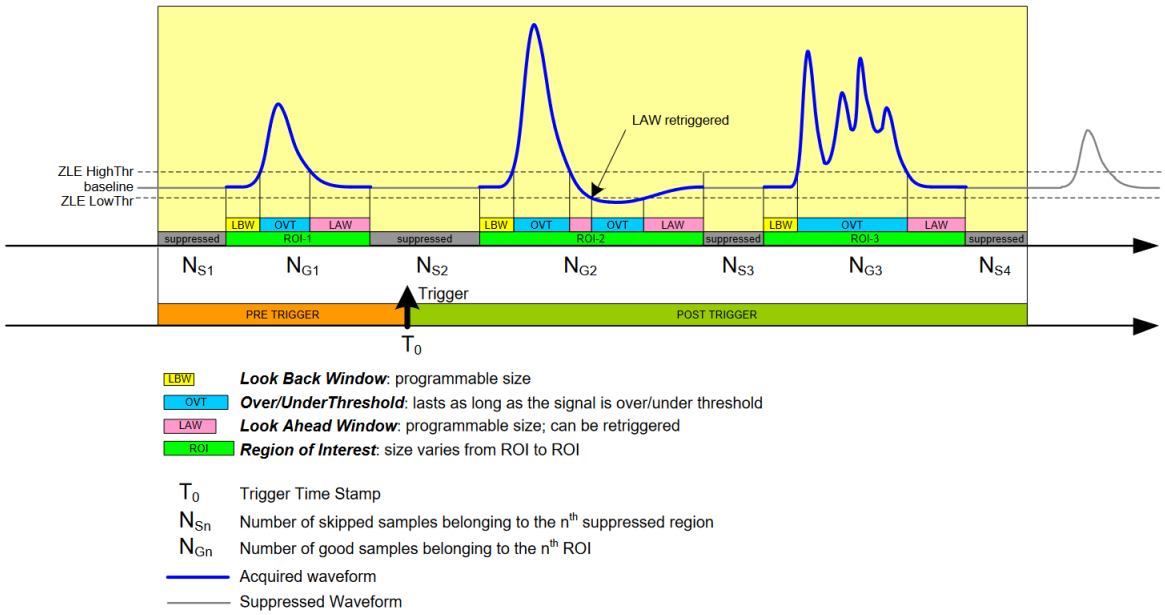

Figure 7.7 A schematic of the CAEN DPP-ZLE algorithm, which automatically discards segments of the waveform that lie in a small band around the baseline, reproduced from [132].

digitized, to provide a reference time for ion signals occurring within the acquisition window and eliminate the ∼20 ns external trigger jitter. The length of the acquisition window is adjustable, and typically set to a length in the range of 30-100 μs. Since a typical TOF peak is <1 μs, only a very small fraction of the waveform contains useful ion data. For this reason the DT5751 was upgraded with Digital Pulse Processing for Zero Length Encoding (DPP-ZLE) firmware, that compresses the data and automatically discards sections of the waveform that lie within an adjustable band around the baseline as shown in Fig. 7.7. With the firmware upgrade, the digitizer was configured to produce a compressed waveform containing multiple regions of interest with ion TOF information.

An example acquisition window is given in Fig. 7.8, showing the compressed waveforms of the TTL trigger signal and the channeltron signal. To measure the ion TOF, the time difference between the ion peak and the rising edge of the TTL signal is calculated and added to the time at which the FPGA sent the TTL signal. The waveforms for a particular measurement are saved in compressed form as individual files. A TOF histogram is created

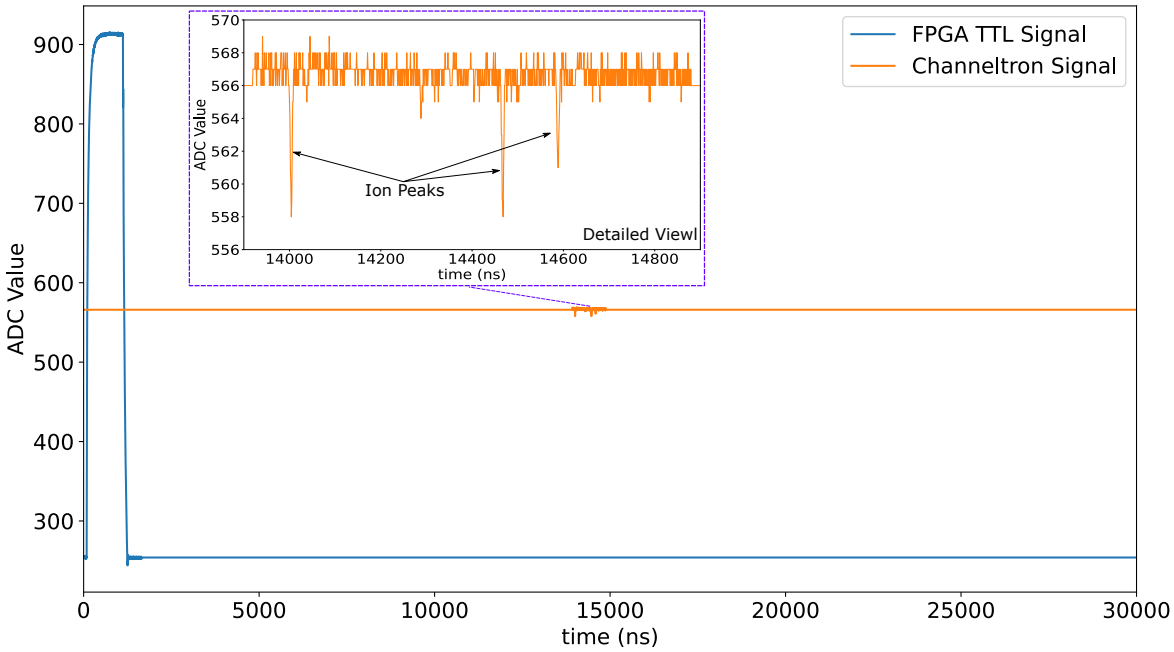

Figure 7.8 An example acquisition window showing the digitized TTL and channeltron signals, which have been compressed with the DPP-ZLE firmware. (inset) Detailed view of a segment of the channeltron signal which was kept by the DPP-ZLE algorithm, showing ion peaks.

by aggregating ion counts across all of the waveforms saved for the measurement as discussed in Section 7.4.

7.2 The MRTOF LAS

After decommissioning the LAS setup discussed in Chapter 4, many of the optical components used in the original experiment were used to create a new LAS for the MRTOF. The optical components were arranged on an 46×30 cm optical board and housed in a 43×28 cm enclosure. The enclosure was constructed with 25 mm 80/20 aluminium profile and 5 mm thick black Delrin plastic to form the walls, which were 28 cm tall.

A separate 30×15 cm optical board was used to mount the 349 nm Spectra Physics laser externally to the enclosure. The height of the laser's optical board was raised by 50 mm with optical posts, and a small 3D printed black PLA tube was used to shield the laser beam

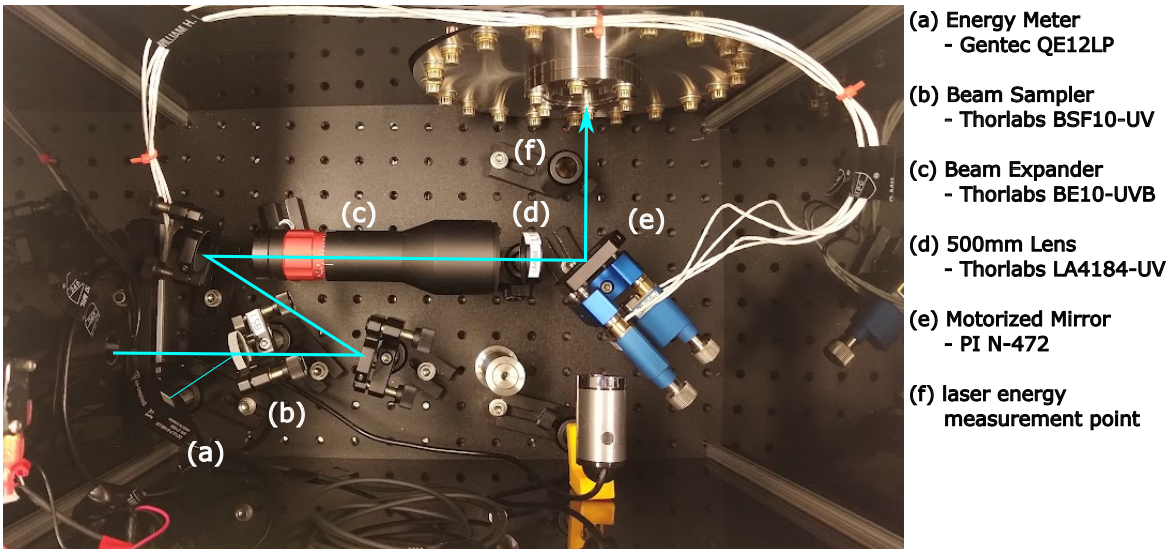

Figure 7.9 A picture of the MRTOF LAS interlock box. Optical elements are indicated by (a)-(f) with the elements detailed on the right.

between the laser's aperture and the wall of the enclosure. The enclosure was mounted onto the Ba-tagging rail system adjacent to the MRTOF's optics cross, such that the face of the DN160CF to DN40CF reducer flange with a DN40CF viewport lay within the enclosure. Black optical tape was used to seal the gaps between the hole in the wall of the enclosure and the DN160CF flange. A switch that was activated by the lid of the enclosure, was used to create an interlock to shut down the laser if the lid was opened.

After the laser beam entered the optics enclosure, a Thorlabs BSF10-UV beam sampler was used to reflect a small percentage of the laser beam energy. The laser energy was measured with a Gentec QE12LP energy meter which was connected to an S-Link 2 pc interface. After passing through the beam sampler, the laser beam was reflected by 2 UV enhanced mirrors installed in kinematic mirror mounts into a Thorlabs BE10-UVB beam expander. The beam expander had a fixed magnification of 10$\times$ the input beam diameter. After the beam was expanded it was focused by a 500 mm fused silica plano-convex lens which was mounted onto a dovetail optical rail, for final focusing of the laser spot on the target surface. A photograph of the optical setup is show in Fig. 7.9.

The fraction of reflected to transmitted laser beam energy was measured as 8(1) %, where the transmitted beam energy was measured consecutively at location (f), and the reflected energy of the beam splitter at (a) in Fig. 7.9. The diameter of the laser beam waist was calculated using eq. (4.2) as $D_f = 31(2)\ \mu m$, where $f = 500$ mm and $M^2 = 1.32(7)$. Due to space constraints, the diameter of the beam before it enters the focusing lens could not be measured, thus the value measured previously with the original LAS of $D = 9.6(1)$ mm (see Chapter 4) was assumed since the laser and beam expander were the same.

7.3 Ion Current Measurements

Initial measurements of the ion current were taken by measuring the current on the collimating aperture, labeled 'col' in Fig. 7.3, with an Agilent 34465A digital multimeter. The potentials of the ion source, quadrupole bender and Ion Optics were set to initial values determined by SIMION simulations. The electrode potentials and the position of the 500 mm focusing lens were adjusted to maximize the ion current from the target. The ion current was measured at 18 locations on the Cu region of the target with the 34465A digital multimeter for 0.25 s at each location. For these measurements, the laser repetition rate was 500 Hz with a beam energy of 41.3(5) μJ per pulse. The mean and standard deviation of the ion current across all scan locations was measured as 4.9(5) nA at the collimating aperture. The procedure was repeated with ion current measurements from the Faraday Cup (FC) as a function of the push/pull actuator position, as shown in 7.10, with a maximum ion current of 0.33(1) nA.

7.3.1 X-Y Steerer tests

After optimmizing the position of the FC, the quadrupole electrodes and the steerer electrodes were tuned to maximise the ion current through the aperture. Steering in the X direction was first optimized by tuning the biases applied to the two quadrupole electrodes nearest to the Ion Optics, labelled 'TR' and 'BR' in Fig. 7.3. The first steerer set that ions enter after

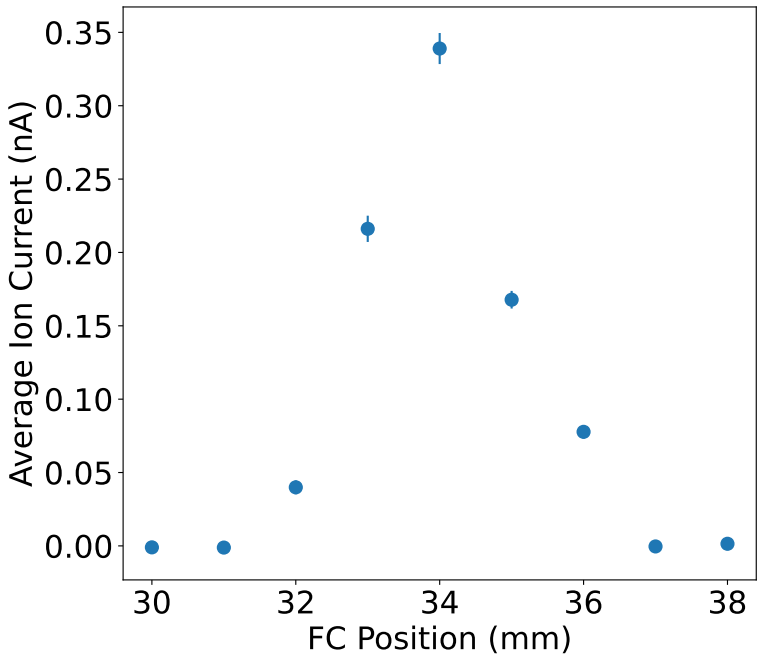

Figure 7.10 The ion current measured with the FC as a function of the FC position.

leaving the quadrupole was then scanned in X and Y, as shown on the top of Fig. 7.11. The laser repetition rate had been lowered to 100 Hz, to be closer to the anticipated repetition rate range that would be used for TOF measurements, thus the measured ion current was generally lower than what was measured when optimizing the FC position. The ion current was found to be optimal when 0 V was applied to 'XY2R', indicating that the quadrupole tuning was sufficient for steering in the X direction. However from the scan it was evident that a correction in the Y direction was needed, with a negative bias applied to 'XY2U'. Since two steerer sets are needed to align the ion beam with the optical axis, the Y direction was scanned with both sets of steerers simultaneously as shown on the bottom in Fig. 7.11. The scan showed that there were two optimal configurations, with either 'XY2U' at a positive value of 30 V and 'XY1U' at a negative value of -40 V or 'XY2U' at a negative value of -30 V and 'XY1U' at a postive value of 10 V. The latter combination was chosen since the previous scan of XY2 only showed that 'XY2U' required a negative bias and therefore a positive bias on 'XY1U' to align the ion beam with the optical axis.

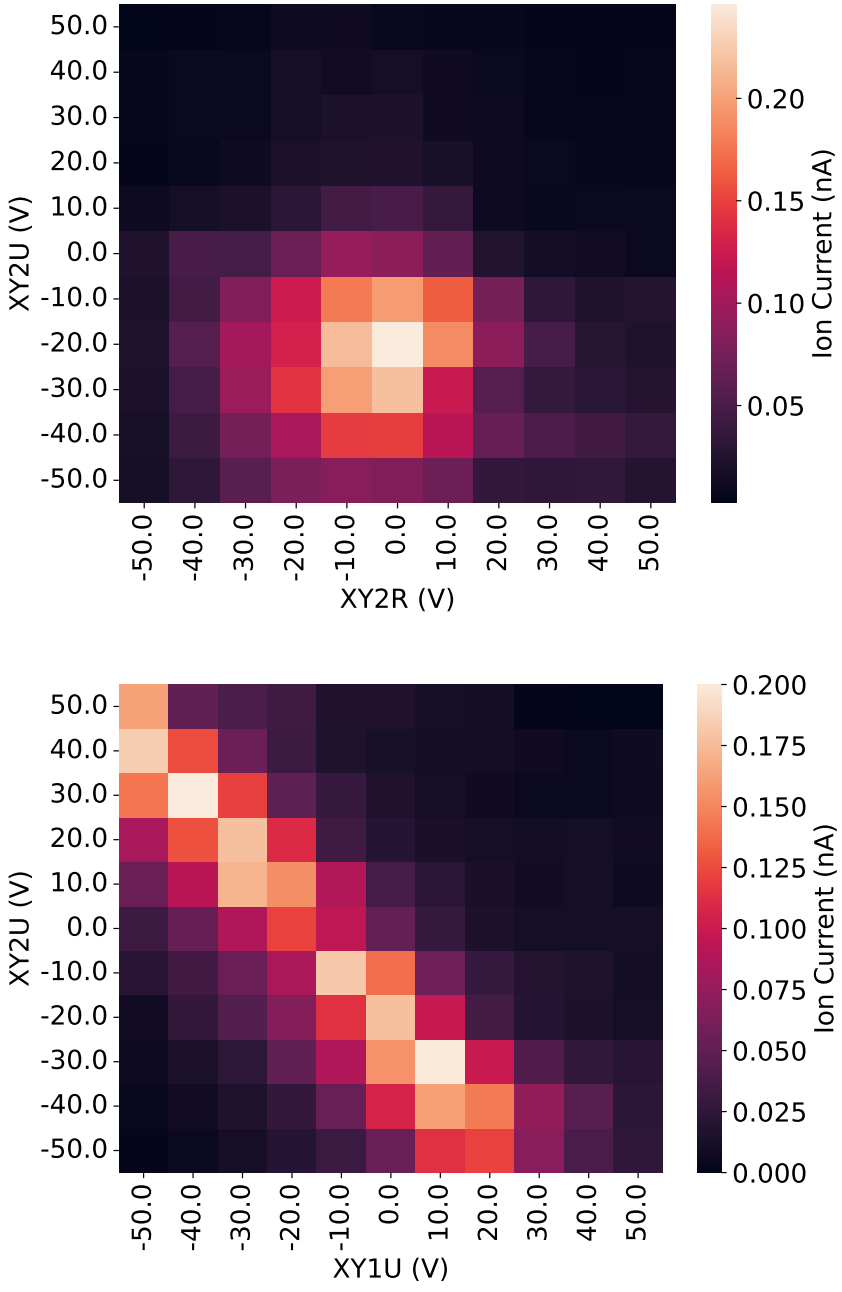

Figure 7.11 (top) Scanning the voltages of a single X-Y steerer set, showing that adjustment in Y was needed but that ions were sufficiently steered in X. (bottom) Scanning the voltages in the Y direction for both steerer sets simultaneously. In both plots the ion current was measured with the FC.

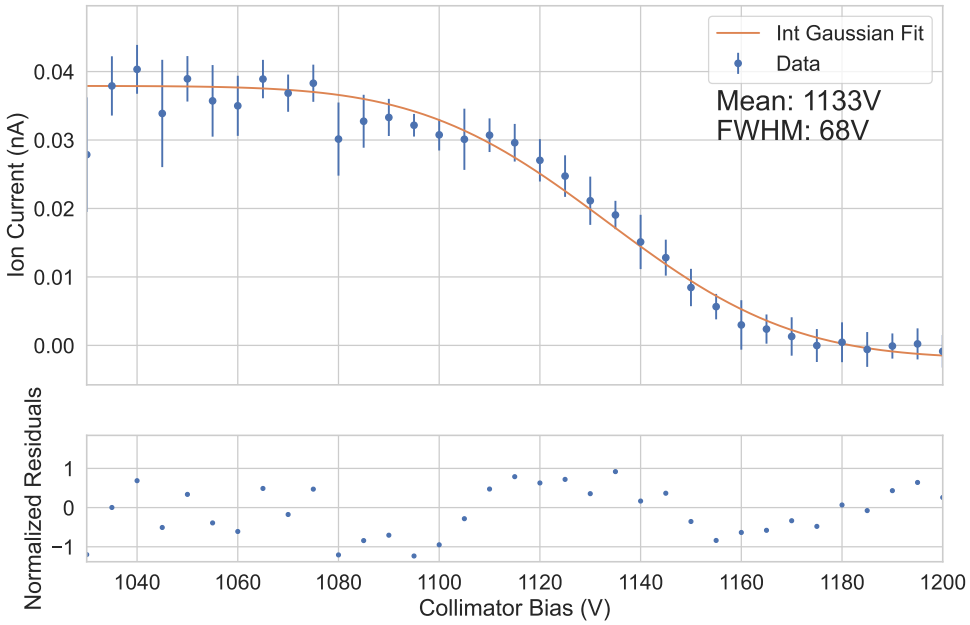

Figure 7.12 A plot of the ion current measured with the FC as a function of the bias applied to the collimator electrode.

7.3.2 Retarding Field Analyzer Measurements

The collimating aperture was used as a retarding field analyzer to estimate the kinetic energy distribution of ions passing through the aperture. With the FC positioned at 34 mm on the actuator scale, the ion current was measured as a function of the bias applied to the collimating aperture. The ion current was measured with the FC from a single laser spot location in the Cu region of the target, with a laser repetition rate of 100 Hz and beam energy of 34.5(3) μJ per pulse. The voltage bias applied to the aperture was increased from 1000 V to 1200 V in increments of 5 V, with the ion current measured over a 5 s window for each data point. A plot of the ion current vs. Collimator Bias is shown in Fig. 7.12, where the mean and FWHM of the kinetic energy distribution was measured by fitting an integrated Gaussian function. The mean kinetic energy of Cu^+ ions from the LAS was inferred as 1133 eV with a FWHM of 68 eV. A FWHM of this magnitude is consistent with previously measured ion kinetic energy distributions, in which the spread is typically >50 eV [133, 105].

Thus the ion kinetic energy spread from the LAS was estimated to be a factor of ∼3 higher than the kinetic energy spread of cooled ions from the LPT, with the parameter δ in excess of 0.03 for $\sim$ 24% of ions.

7.4 TOF Measurements with Cu^+

For initial trapping tests, the time that Cu ions reached the entrance mirror was estimated by adjusting the time at which the switched electrodes were switched to their trapping values, and observing the switch time that corresponded to the disappearance of the ion signal. The same procedure was repeated for the exit mirror through adjustment of the ejection time. The capture time was set to 25 μs, which was the midpoint between the entrance and exit mirror ion arrival times. A rough estimate for the revolution time was assumed as ≈ 40 μs, which was double the time taken for ions to travel from the entrance mirror to the exit mirror. The ejection time was then adjusted in multiples of the estimated revolution time, to trap ions for an increasing number of revolutions. A trigger signal was sent to the digitizer 10 μs after ejection, to capture the channeltron waveform within an acquisition window with a length of 32 μs. The TOF spectra for each revolution number was constructed by combining 100 waveforms and counting the ion signal peaks within them to form a histogram. The TOF spectra for 1-5 revolutions are plotted on the top of Fig. 7.13, where it was seen that at 3 revolutions the Cu^+ peak splits into the stable isotopes of $^{63}Cu^+$ and $^{65}Cu^+$. The TOF value for the peak of $^{63}Cu^+$ was plotted as a function of the revolution number, as shown on the bottom of Fig. 7.13, from which the revolution time for $^{63}Cu^+$ was extracted as 36.29 μs.

After the initial trapping tests, the ejection time was parameterised as

$$t_{\text{eject}} = t_{\text{cap}} + N \times t_{\text{rev}}, \tag{7.5}$$

where t_{cap} was the time at which the analyzer was closed, t_{rev} was the revolution time and N the number of revolutions. With the measured revolution time, the number of revolutions was then increased into the hundreds, reaching a TOF up to 15 ms as shown in Fig. 7.14.

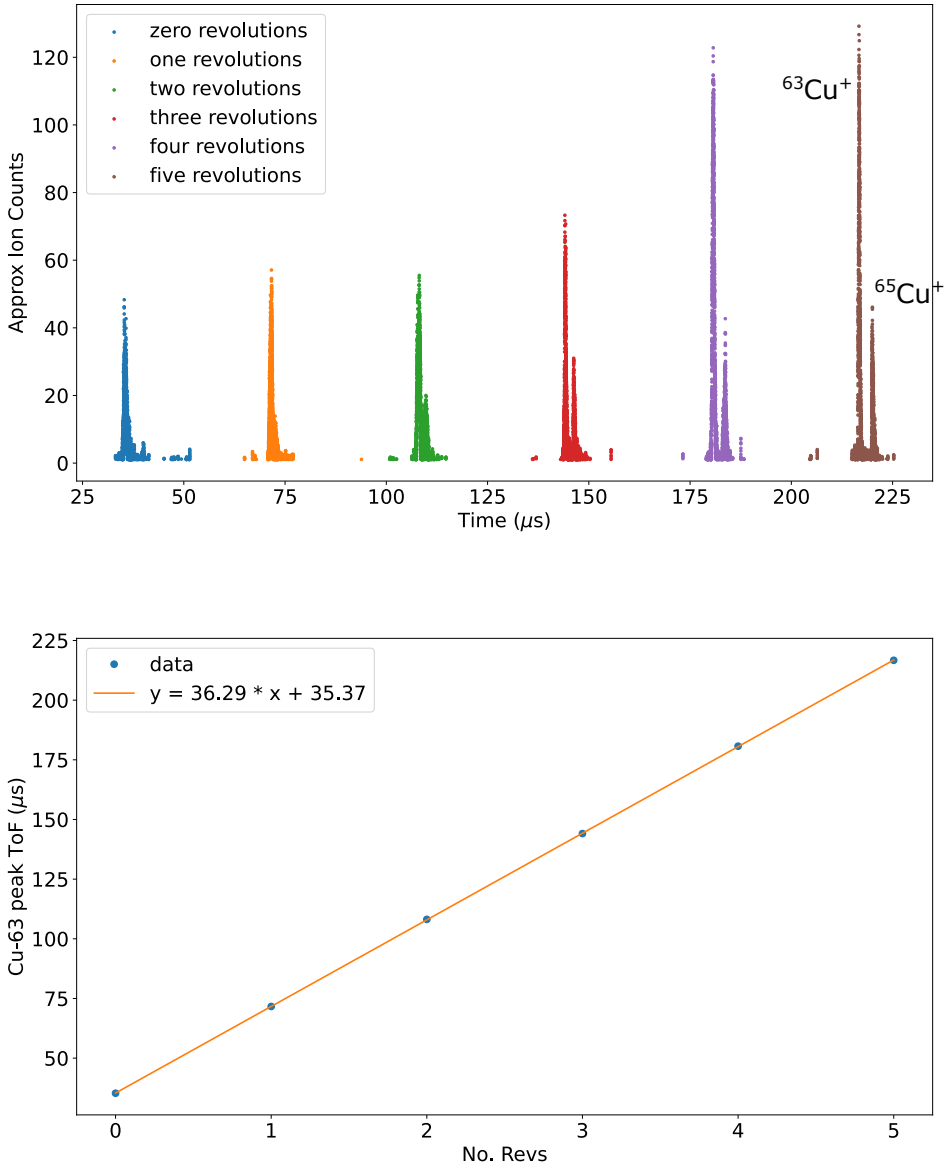

Figure 7.13 (top) Plots of TOF histograms for increasing revolution numbers, which shows the splitting of the Cu peak into the stable isotopes ^{63}Cu and ^{65}Cu at 3 revolutions. (bottom) Plot of the ^{63}Cu TOF peak vs. the number of revolutions, with which the revolution time was extracted as 36.29 μs from the slope.

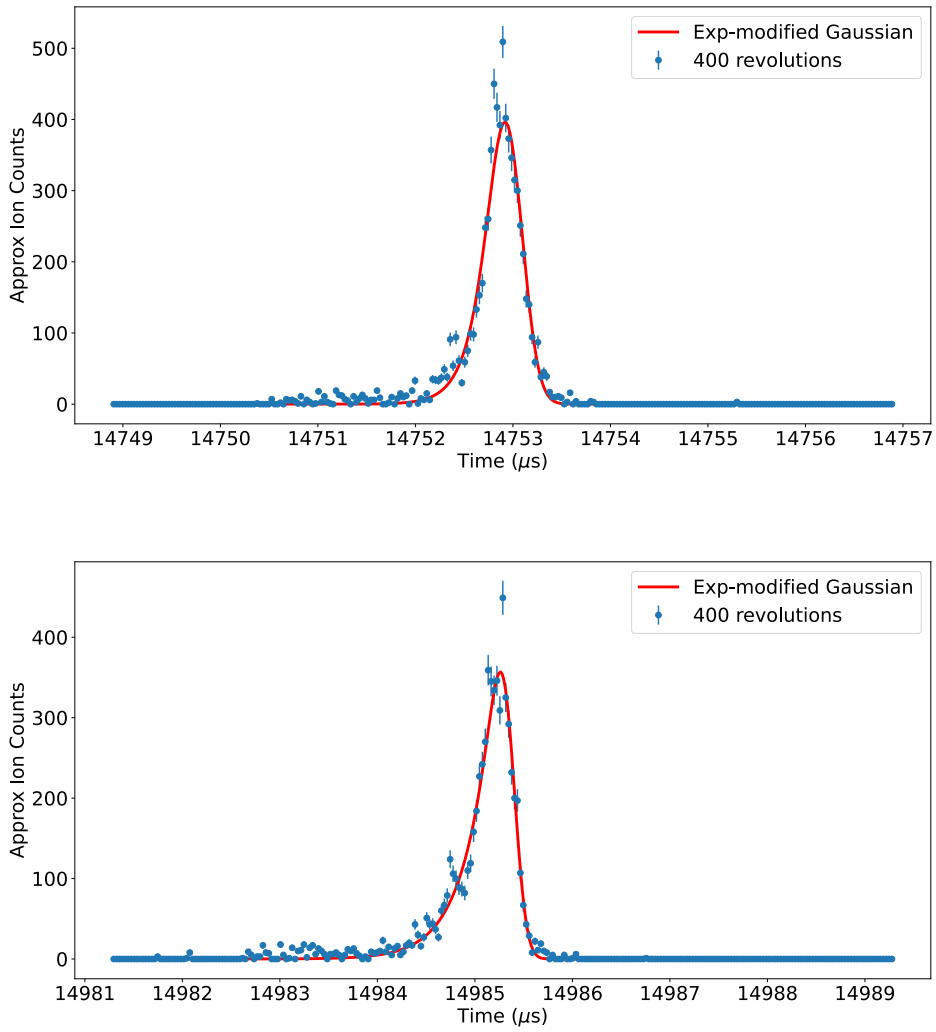

Figure 7.14 (top) TOF histogram for ^{63}Cu at 400 revolutions and ∼15 ms of flight time. (bottom) TOF histogram for ^{65}Cu at 400 revolutions which occurs at ∼200 μs later. The fitted peak centers and FWHMs are displayed in Table 7.2.

Table 7.2 TOF meausurements for Cu isotopes at 400 revolutions, atomic mass and relative abundance figures are taken from [134].

Isotope	Center (μs)	FWHM (μs)	t_{rev} (μs)	Atomic Mass	Abundance (%)
$^{63}Cu^{+}$	14753.442	0.331	36.793	62.92959772(56)	69.15(15)
$^{65}Cu^{+}$	14985.467	0.290	37.373	64.92778970(71)	30.85(15)

The TOF spectra for $^{63}Cu^+$ and $^{65}Cu^+$ were measured for 400 revolutions and fit with exponentially-modified Gaussian functions. The measured TOF peak centers and FWHM are displayed in Table 7.2, with the NIST measurements of the atomic mass and relative abundance. The TOF peak for $^{63}Cu^+$ was used as a known calibrant species to measure the mass of $^{65}Cu^+$ for comparison with the literature value. From the TOF data the mass of $^{65}Cu^+$ was measured as 64.9245 +- 0.0039 u, which was in agreement with the literature value, and the MRP was calculated using eq. (5.3) as $R = 22000$. The laser repetition rate was lowered to 50 Hz to allow for a TOF up to 20 ms, with an estimated laser fluence of 5.9 J/cm^2 per pulse. A list of the bias settings used for the 400 revolution measurements is given in the appendix in Tables A.1 and A.2.

The retarding field analyzer measurement showed that the kinetic energy spread of ions produced by the LAS was larger than that of the ions produced by the LPT, which was consistent with the literature [105]. Thus it was expected that the MRP of the MRTOF when operated with the LAS would be lower than the simulated maximum, since simulations showed that $(t|\delta\delta\delta)$ and higher order coefficients will create TOF dispersion in the MRTOF mirrors for ions with a $|\delta| > 0.02$.

Chapter 8

Conclusions

The observation of $0\nu\beta\beta$ would demonstrate the Majorana nature of the neutrino. This has potentially far-reaching implications, from the development of massive neutrino theories that go beyond the Standard Model, to providing a measurement of the effective Majorana neutrino mass. It is clear that the next generation of experiments will have to employ advanced methods of background reduction, in order to boost their sensitivity and discovery potential. In this regard, the prospect of Ba-tagging remains a promising potential upgrade for the planned nEXO experiment.

The Canadian Ba-tagging system has and will continue to benefit from the development of the spatially-resolved multi-element LAS, which was discussed in Chapter 4. The LAS demonstrated that the different materials of a multi-element could be selectively ablated, with a spatial resolution of ~ 50 μm and without the addition of moving parts inside the vacuum chamber. Beyond the Ba-tagging system, the LAS can serve as a powerful calibration tool in the field of mass spectrometry, by producing diverse ion species in vacuum or in the presence of an ambient gas. Moreover, the LAS has proven to be vital as an independent ion source for commissioning the MRTOF. Allowing for the demonstration of ion trapping in advance of the commissioning of the LPT, and facilitating the development of software and electronics for the system. The coupling of the MRTOF to the scanning LAS also allows for the unique possibility of mass spectroscopy with an MRTOF. Hence the LAS/MRTOF combination

could be an avenue of interest for future investigations.

The MRTOF was designed and commissioned for the Ba-tagging system, to perform systematic studies of the ion extraction technique, as well as provide confirmation of the mass of the Ba isotope. Simulations showed that the MRTOF could achieve an MRP in excess of $m/\Delta m > 100000$ with simulated ions from the LPT RFQ buncher. With the anticipated resolving-power the MR TOF will be able to separate the ^{136}Xe and ^{136}Ba isotopes, which requires a minimum MRP of $m/\Delta m > 50000$, and provide confirmation of the Ba ion's atomic mass. The MRTOF operation mode employed the method of delayed bunching by optimising $N-1$ reflections to be isochronous relative to the mid-plane of the analyzer, and shifting the time focus onto the detector with the final reflection. Using this technique had the added benefits of reducing space-charge effects and streamlining the optimisation process. Delayed bunching was realised practically through the use of 3-state HV switches in the entrance mirror, that provided a third bias state for the final reflection.

The assembled MRTOF was tested with ion bunches from the LAS and has so far demonstrated the trapping of ions for up to 15 ms, with an available MRP of $m/\Delta m \approx 20000$. With cooled ions from the LPT, the MRTOF is anticipated to reach the design MRP as shown with the simulations. It was found that the FPGA timing system performed adequately, with a low timing self-jitter of < 0.5 ns. An additional jitter of 33 ns was incurred due to the requirement that the FPGA start its timing sequence relative to an external TTL signal from the laser. The 33 ns jitter is relatively negligible by comparison with the FWHMs of the measured Cu^+ TOF spectra. However, the TOF spectra expected from operation with the LPT will be potentially comparable in width, with a FWHM ~ 30 ns. Therefore it is recommended that a single FPGA is used to operate both the LPT and MRTOF, so that only the self-jitter is relevant.

Bibliography

[1] S Fukuda, Y Fukuda, M Ishitsuka, Y Itow, T Kajita, J Kameda, K Kaneyuki, K Kobayashi, Y Koshio, M Miura, et al. Constraints on neutrino oscillations using 1258 days of Super-Kamiokande solar neutrino data. *Phys. Rev. Lett.*, 86(25):5656, 2001.

[2] Q. R. et al. Ahmad. Direct evidence for neutrino flavor transformation from neutral-current interactions in the Sudbury Neutrino Observatory. *Phys. Rev. Lett.*, 89:011301, Jun 2002.

[3] E Majorana. Nuovo Cim. 9, 335 (1932). *Nuovo Cim*, 14:171, 1937.

[4] JD Vergados, H Ejiri, and F Šimkovic. Theory of neutrinoless double-beta decay. *Reports on Progress in Physics*, 75(10):106301, 2012.

[5] S Al Kharusi, A Alamre, JB Albert, M Alfaris, G Anton, IJ Arnquist, I Badhrees, PS Barbeau, D Beck, V Belov, et al. nEXO pre-conceptual design report. *arXiv:1805.11142*, 2018.

[6] Govinda Adhikari, S Al Kharusi, E Angelico, G Anton, IJ Arnquist, I Badhrees, J Bane, V Belov, EP Bernard, T Bhatta, et al. nEXO: neutrinoless double beta decay search beyond 10^{28} year half-life sensitivity. *Journal of Physics G: Nuclear and Particle Physics*, 49(1):015104, 2021.

[7] Samuel Ayet San Andrés, Christine Hornung, Jens Ebert, Wolfgang R Plaß, Timo Dickel, Hans Geissel, Christoph Scheidenberger, Julian Bergmann, Florian Greiner, Emma Haettner, et al. High-resolution, accurate multiple-reflection time-of-flight mass spectrometry for short-lived, exotic nuclei of a few events in their ground and low-lying isomeric states. *Phys. Rev. C*, 99(6):064313, 2019.

[8] K Murray, J Dilling, R Gornea, Y Ito, Thomas Koffas, AA Kwiatkowski, Y Lan, MP Reiter, V Varentsov, and T Brunner. Design of a multiple-reflection time-of-flight mass spectrometer for barium-tagging. *Hyperfine Interactions*, 240(1):1–9, 2019.

[9] K Murray, C Chambers, D Chen, Z Feng, J Fraser, Y Ito, Y Lan, S Mendez, M Medina Peregrina, H Rasiwala, et al. Characterization of a spatially resolved multi-element laser ablation ion source. *International Journal of Mass Spectrometry*, 472:116763, 2022.

[10] Wolfgang Pauli. Dear radioactive ladies and gentlemen. *Physics Today*, page 27, 1930.

[11] Enrico Fermi. An attempt of a theory of beta radiation. 1. *Z. phys*, 88(161):19, 1934.

[12] Clyde L Cowan Jr, Frederick Reines, FB Harrison, HW Kruse, and AD McGuire. Detection of the free neutrino: a confirmation. *Science*, 124(3212):103–104, 1956.

[13] B. Pontecorvo. Electron and muon neutrinos. *Zh. Eksp. Teor. Fiz.*, 37:1751–1757, 1959.

[14] Gaillard Danby, Jean Maurice Gaillard, Konstantin Goulianos, Leon M Lederman, Nariman Mistry, Melvin Schwartz, and Jack Steinberger. Observation of high-energy neutrino reactions and the existence of two kinds of neutrinos. *Phys. Rev. Lett.*, 9(1):36, 1962.

[15] Kai Zuber. *Neutrino physics*. Taylor & Francis, 2020.

[16] M. L. Perl et al. Evidence for anomalous lepton production in $e^+ - e^-$ annihilation. *Phys. Rev. Lett.*, 35:1489, 1975.

[17] K Kodama et al. Observation of tau neutrino interactions. *Phys. Lett. B*, 504(3):218, 2001.

[18] Raymond Davis Jr, Don S Harmer, and Kenneth C Hoffman. Search for neutrinos from the sun. *Phys. Rev. Lett.*, 20(21):1205, 1968.

[19] WC Haxton. The solar neutrino problem. *Annual Review of Astronomy and Astrophysics*, 33(1):459–503, 1995.

[20] B Pontecorvo. J. exp. theor. phys. 1958.

[21] V. Gribov and B. Pontecorvo. Neutrino astronomy and lepton charge. *Phys. Lett. B*, 28(7):493–496, 1969.

[22] Ziro Maki, Masami Nakagawa, and Shoichi Sakata. Remarks on the Unified Model of Elementary Particles. *Progress of Theoretical Physics*, 28(5):870–880, 11 1962.

[23] R.Jeffrey Wilkes. Results on neutrino oscillations from Super-Kamiokande. *Advances in Space Research*, 26(11):1813–1822, 2000.

[24] Q Retal Ahmad, RC Allen, TC Andersen, JD Anglin, JC Barton, EW Beier, M Bercovitch, J Bigu, SD Biller, RA Black, et al. Direct evidence for neutrino flavor transformation from neutral-current interactions in the Sudbury Neutrino Observatory. *Phys. Rev. Lett.*, 89(1):011301, 2002.

[25] Claudio Giganti, Stéphane Lavignac, and Marco Zito. Neutrino oscillations: the rise of the PMNS paradigm. *Progress in Particle and Nuclear Physics*, 98:1–54, 2018.

[26] X Qian and P Vogel. Neutrino mass hierarchy. *Progress in Particle and Nuclear Physics*, 83:1–30, 2015.

[27] R. L. Workman and Others. Review of Particle Physics. *PTEP*, 2022:083C01, 2022.

[28] Ma Concepción Gonzalez-Garcia, Michele Maltoni, and Thomas Schwetz. Global analyses of neutrino oscillation experiments. *Nuclear Physics B*, 908:199–217, 2016.

[29] Samoil Bilenky. *Introduction to the physics of massive and mixed neutrinos*, volume 947. Springer, 2018.

[30] The KATRIN Collaboration. Direct neutrino-mass measurement with sub-electronvolt sensitivity. *Nature Physics*, 18(2):160–166, 2022.

[31] Manfred Lindner, Tommy Ohlsson, and Gerhart Seidl. Seesaw mechanisms for dirac and majorana neutrino masses. *Phys. Rev. D*, 65(5):053014, 2002.

[32] SM Bilenky and Carlo Giunti. Neutrinoless double-beta decay: A brief review. *Modern Phys. Lett. A*, 27(13):1230015, 2012.

[33] M. Goeppert-Mayer. Double beta-disintegration. *Phys. Rev.*, 48:512–516, Sep 1935.

[34] Ruben Saakyan. Two-neutrino double-beta decay. *Annual Review of Nuclear and Particle Science*, 63:503–529, 2013.

[35] Stefano Dell'Oro, Simone Marcocci, Matteo Viel, and Francesco Vissani. Neutrinoless double beta decay: 2015 review. *Advances in High Energy Physics*, 2016, 2016.

[36] Michelle J Dolinski, Alan WP Poon, and Werner Rodejohann. Neutrinoless double-beta decay: status and prospects. *arXiv:1902.04097*, 2019.

[37] I Nutini, DQ Adams, C Alduino, K Alfonso, FT Avignone III, O Azzolini, G Bari, F Bellini, G Benato, M Beretta, et al. New results from the CUORE experiment. *International Journal of Modern Physics A*, 37(07):2240014, 2022.

[38] E Armengaud, C Augier, AS Barabash, F Bellini, G Benato, Alain Benoit, M Beretta, L Bergé, J Billard, Yu A Borovlev, et al. New limit for neutrinoless double-beta decay of Mo 100 from the CUPID-Mo experiment. *Phys. Rev. Lett.*, 126(18):181802, 2021.

[39] A Armatol, E Armengaud, W Armstrong, C Augier, FT Avignone, O Azzolini, A Barabash, G Bari, A Barresi, D Baudin, et al. Characterization of cubic $Li_2^{100}MoO_4$ crystals for the CUPID experiment. *The European Physical Journal C*, 81(2):1–10, 2021.

[40] M. et al. Agostini. Final results of GERDA on the search for neutrinoless double-β decay. *Phys. Rev. Lett.*, 125:252502, Dec 2020.

[41] S.R. Elliott et al. Initial results from the majorana demonstrator. *Journal of Physics: Conference Series*, 888(1):012035, sep 2017.

[42] N Abgrall, I Abt, M Agostini, A Alexander, C Andreoiu, GR Araujo, FT Avignone III, W Bae, A Bakalyarov, M Balata, et al. LEGEND-1000 preconceptual design report. *arXiv:2107.11462*, 2021.

[43] Mario Schwarz, Patrick Krause, Andreas Leonhardt, Laszlo Papp, Stefan Schönert, Christoph Wiesinger, Maria Fomina, Konstantin Gusev, Nadezda Rumyantseva, Egor Shevchik, et al. Liquid argon instrumentation and monitoring in LEGEND-200. In *EPJ Web of Conferences*, volume 253, page 11014. EDP Sciences, 2021.

[44] D. Akimov, G. Bower, M. Breidenbach, R. Conley, E. Conti, M. Danilov, R. DeVoe, Z. Djurcic, A. Dolgolenko, W. Fairbank, G. Gratta, C. Hall, T. Koffas, M. Moe, A. Odian, A. Piepke, C.Y. Prescott, P.C. Rowson, K. Skarpaas, P. Vogel, J-L. Vuilleumier, S. Waldman, K. Wamba, J. Wodin, and O. Zeldovich. EXO: an advanced Enriched Xenon double-beta decay Observatory. *Nuclear Physics B - Proceedings Supplements*, 138:224–226, 2005. Proceedings of the Eighth International Workshop on Topics in Astroparticle and Undeground Physics.

[45] E Aprile and T Doke. Liquid xenon detectors for particle physics and astrophysics. *Reviews of Modern Physics*, 82(3):2053, 2010.

[46] E. Conti et al. Correlated fluctuations between luminescence and ionization in liquid xenon. *Phys. Rev. B*, 68:054201, 2003.

[47] NIST. https://www.nist.gov/pml/xcom-photon-cross-sections-database , visited 2022-11.

[48] M Auger et al. The EXO-200 detector, part I: detector design and construction. *Journal of Instrumentation*, 7(05):P05010, 2012.

[49] G. et al. Anton. Search for neutrinoless double-β decay with the complete EXO-200 dataset. *Phys. Rev. Lett.*, 123:161802, Oct 2019.

[50] JB Albert, DJ Auty, PS Barbeau, D Beck, V Belov, M Breidenbach, T Brunner, A Burenkov, GF Cao, C Chambers, et al. Cosmogenic backgrounds to $0\nu\beta\beta$ in EXO-200. *Journal of Cosmology and Astroparticle Physics*, 2016(04):029, 2016.

[51] JB Albert, M Auger, DJ Auty, PS Barbeau, E Beauchamp, D Beck, V Belov, C Benitez-Medina, J Bonatt, M Breidenbach, et al. Improved measurement of the $2\nu\beta\beta$ half-life of 136 Xe with the EXO-200 detector. *Phys. Rev. C*, 89(1):015502, 2014.

[52] Matthew Redshaw, Elizabeth Wingfield, Joseph McDaniel, and Edmund G. Myers. Mass and double-beta-decay Q value of ^{136}Xe. *Phys. Rev. Lett.*, 98:053003, Feb 2007.

[53] JB Albert, G Anton, IJ Arnquist, I Badhrees, P Barbeau, D Beck, V Belov, F Bourque, JP Brodsky, E Brown, et al. Sensitivity and discovery potential of the proposed nEXO experiment to neutrinoless double-β decay. *Phys. Rev. C*, 97(6):065503, 2018.

[54] GC Carlson, WC Schick Jr, WL Talbert Jr, and Fo K Wohn. Half-lives of some short-lived mass-separated gaseous fission products and their daughters. *Nuclear Physics A*, 125(2):267–275, 1969.

[55] Ivan Esteban, Maria Conceptión González-García, Michele Maltoni, Thomas Schwetz, and Albert Zhou. The fate of hints: updated global analysis of three-flavor neutrino oscillations. *Journal of High Energy Physics*, 2020(9):1–22, 2020.

[56] nEXO Collaboration. Imaging individual barium atoms in solid xenon for barium tagging in nEXO. *Nature*, 569(7755):203–207, 2019.

[57] K Twelker, S Kravitz, M Montero Díez, G Gratta, W Fairbank Jr, JB Albert, DJ Auty, PS Barbeau, D Beck, C Benitez-Medina, et al. An apparatus to manipulate and identify individual Ba ions from bulk liquid Xe. *Review of Scientific Instruments*, 85(9):095114, 2014.

[58] NK Byrnes, AA Denisenko, FW Foss Jr, BJP Jones, AD McDonald, DR Nygren, P Thapa, and K Woodruff. Barium tagging with selective, dry-functional, single molecule sensitive on-off fluorophores for the NEXT experiment. *arXiv:1909.04677*, 2019.

[59] NEXT collaboration et al. Sensitivity of NEXT-100 to neutrinoless double beta decay. *Journal of High Energy Physics*, 2016(5):159, 2016.

[60] N Byrnes, FW Foss, BJP Jones, AD McDonald, DR Nygren, P Thapa, A Trinidad, the NEXT collaboration, et al. Progress toward barium tagging in high pressure xenon gas with single molecule fluorescence imaging. In *Journal of Physics: Conference Series*, volume 1312, page 012001. IOP Publishing, 2019.

[61] JB Albert, DJ Auty, PS Barbeau, D Beck, V Belov, M Breidenbach, T Brunner, A Burenkov, GF Cao, C Chambers, et al. Measurements of the ion fraction and mobility of α- and β-decay products in liquid xenon using the EXO-200 detector. *Phys. Rev. C*, 92(4):045504, 2015.

[62] Thomas Brunner, Daniel Fudenberg, Victor Varentsov, Amanda Sabourov, Giorgio Gratta, Jens Dilling, Ralph DeVoe, David Sinclair, William Fairbank Jr, Joshua B Albert, et al. An RF-only ion-funnel for extraction from high-pressure gases. *International Journal of Mass Spectrometry*, 379:110–120, 2015.

[63] Yang Lan. *A linear Paul trap for barium tagging of neutrinoless double beta decay in nEXO*. PhD thesis, University of British Columbia, 2020.

[64] Samuel J Waldman. *Single ion trapping for the Enriched Xenon Observatory*. Stanford University, 2005.

[65] Ryan Scott Killick. *Observation of Singly Charged Barium Ions in a Buffer Gas: Towards a Functional Barium-Tagging System for Use in the Enriched Xenon Observatory*. PhD thesis, Carleton University, 2015.

[66] R Harkewicz, J Stacy, J Greene, and RC Pardo. Solid material evaporation into an electron cyclotron resonance source by laser ablation. *Review of Scientific Instruments*, 65(4):1104–1106, 1994.

[67] Shang Rencheng, Xu Sida, Zhang Wei, Yi Rong, Zhang Shuming, Ye Zipiao, Zhao Zhizheng, and Luo Yixiao. Laser ion source via direct ionization at the outlet of a helium jet. *Review of Scientific Instruments*, 68(8):3027–3030, 1997.

[68] S Gammino, L Torrisi, L Andò, G Ciavola, L Celona, L Laska, J Krasa, M Pfeifer, K Rohlena, E Woryna, et al. Production of low energy, high intensity metal ion beams by means of a laser ion source. *Review of Scientific Instruments*, 73(2):650–653, 2002.

[69] Boris N Chichkov et al. Femtosecond, picosecond and nanosecond laser ablation of solids. *Applied Physics A*, 63(2):109–115, 1996.

[70] Masahiro Okamura, Megumi Sekine, Kazumasa Takahashi, Kotaro Kondo, and Takeshi Kanesue. Laser ablation ion source for heavy ion inertial fusion. *Nuclear Instruments and Methods in Physics Research Section A: Accelerators, Spectrometers, Detectors and Associated Equipment*, 733:97–102, 2014.

[71] Ahmed Asaad I Khalil, Ashraf I Hafez, Mahmoud E Elgohary, and Mohamed A Morsy. Tungsten ion source under double-pulse laser ablation system. *Chinese Physics B*, 26(9):095201, 2017.

[72] GQ Saquilayan, S Ikeda, T Kanesue, M Wada, and M Okamura. Production of oxygen ions through the laser ablation of alumina. In *AIP Conference Proceedings*, volume 2011, page 020013. AIP Publishing LLC, 2018.

[73] Naoya Munemoto, Ken Takayama, Susumu Takano, Masahiro Okamura, and Masahumi Kumaki. Development of the C6+ laser ablation ion source for the KEK digital accelerator. *Review of Scientific Instruments*, 85(2):02B922, 2014.

[74] Ahmed M Elsied et al. Nanosecond laser-metal ablation at different ambient conditions. *Spectrochimica Acta Part B: Atomic Spectroscopy*, 143:26–31, 2018.

[75] High power single-shot laser ablation of silicon with nanosecond 355nm. *Applied Surface Science*, 252(22):7823 – 7825, 2006.

[76] Müller, Wolfgang and others. Initial performance metrics of a new custom-designed ArF excimer LA-ICPMS system coupled to a two-volume laser-ablation cell. *Journal of Analytical Atomic Spectrometry*, 24(2):209–214, 2009.

[77] Andreas Riedo et al. Coupling of LMS with a fs-laser ablation ion source: elemental and isotope composition measurements. *Journal of Analytical Atomic Spectrometry*, 28(8):1256–1269, 2013.

[78] Martin Koestler et al. A high-resolution scanning microprobe matrix-assisted laser desorption/ionization ion source for imaging analysis on an ion trap/fourier transform ion cyclotron resonance mass spectrometer. *Rapid Communications in Mass Spectrometry*, 22(20):3275–3285, 2008.

[79] Tyler Green et al. Characterization of extreme ultraviolet laser ablation mass spectrometry for actinide trace analysis and nanoscale isotopic imaging. *Journal of Analytical Atomic Spectrometry*, 32(6):1092–1100, 2017.

[80] Reto Wiesendanger et al. Improved detection sensitivity for heavy trace elements using a miniature laser ablation ionisation mass spectrometer. *Journal of Analytical Atomic Spectrometry*, 32(11):2182–2188, 2017.

[81] Yang Cui et al. Depth profiling and imaging capabilities of an ultrashort pulse laser ablation time of flight mass spectrometer. *Review of Scientific Instruments*, 83(9):093702, 2012.

[82] Franziska Bauer, Andreas Michalowski, Thomas Kiedrowski, and Stefan Nolte. Heat accumulation in ultra-short pulsed scanning laser ablation of metals. *Optics Express*, 23(2):1035–1043, 2015.

[83] M Tajima, A Takamine, M Wada, and H Ueno. Offline ion source for laser spectroscopy of RI at the SLOWRI. *Nuclear Instruments and Methods in Physics Research Section B: Beam Interactions with Materials and Atoms*, 486:48–54.

[84] Seung H Ko, Yeonho Choi, David J Hwang, Costas P Grigoropoulos, Jaewon Chung, and Dimos Poulikakos. Nanosecond laser ablation of gold nanoparticle films. *Applied Phys. Lett.*, 89(14):141126, 2006.

[85] R Jordan, D Cole, JG Lunney, K Mackay, and D Givord. Pulsed laser ablation of copper. *Applied Surface Science*, 86(1-4):24–28, 1995.

[86] Jaewon Chung, Sewoon Han, Daeho Lee, Sanghoon Ahn, Costas P Grigoropoulos, Jooho Moon, and Seung Hwan Ko. Nanosecond laser ablation of silver nanoparticle film. *Optical Engineering*, 52(2):024302, 2013.

[87] M Hashida, A.F Semerok, O Gobert, G Petite, Y Izawa, and J.F-Wagner. Ablation threshold dependence on pulse duration for copper. *Applied Surface Science*, 197-198:862–867, 2002. COLA'01 SI.

[88] LM Cabalin and JJ Laserna. Experimental determination of laser induced breakdown thresholds of metals under nanosecond Q-switched laser operation. *Spectrochimica Acta Part B: Atomic Spectroscopy*, 53(5):723–730, 1998.

[89] G Baraldi, A Perea, and Carmen N Afonso. Dynamics of ions produced by laser ablation of several metals at 193 nm. *Journal of Applied Physics*, 109(4):043302–043302, 2011.

[90] Spectra-Physics. *Explorer OEM User's Manual*. Newport Corporation.

[91] Sidney A Self. Focusing of spherical gaussian beams. *Applied Optics*, 22(5):658–661, 1983.

[92] Anthony E Siegman. How to (maybe) measure laser beam quality. In *Diode Pumped Solid State Lasers: Applications and Issues*, page MQ1. Optical Society of America, 1998.

[93] JM Liu. Simple technique for measurements of pulsed Gaussian-beam spot sizes. *Optics Letters*, 7(5):196–198, 1982.

[94] Alexandre F Semerok, Beatrice Salle, Jean-Luc Lacour, J-F Wagner, Guillaume Petite, Olivier Gobert, Pierre Meynadier, and Michel Perdrix. Femtosecond, picosecond, and nanosecond laser microablation: Laser plasma and crater investigation. In *ECLIM 2000: 26th European Conference on Laser Interaction with Matter*, volume 4424, pages 574–579. International Society for Optics and Photonics, 2001.

[95] Mihai Stafe, Aurelian Marcu, and Niculae N Puscas. *Pulsed laser ablation of solids: basics, theory and applications*, volume 53. Springer Science & Business Media, 2013.

[96] Yong Jee, Michael F Becker, and Rodger M Walser. Laser-induced damage on single-crystal metal surfaces. *JOSA B*, 5(3):648–659, 1988.

[97] Gediminas Raciukaitis, Marijus Brikas, Paulius Gecys, and Mindaugas Gedvilas. Accumulation effects in laser ablation of metals with high-repetition-rate lasers. In *High-Power Laser Ablation VII*, volume 7005, page 70052L. International Society for Optics and Photonics, 2008.

[98] M Shane Hutson, Borislav Ivanov, Aroshan Jayasinghe, Gilma Adunas, Yaowu Xiao, Mingsheng Guo, and John Kozub. Interplay of wavelength, fluence and spot-size in free-electron laser ablation of cornea. *Optics Express*, 17(12):9840–9850, 2009.

[99] Jean-Yves Natoli, Jeremie Capoulade, Hervé Piombini, and Bertrand Bertussi. Influence of laser beam size and wavelength in the determination of LIDT and associated laser damage precursor densities in KH2PO4. In *Laser-Induced Damage in Optical Materials: 2007*, volume 6720, page 672016. International Society for Optics and Photonics, 2007.

[100] CW Carr, HB Radousky, and SG Demos. Wavelength dependence of laser-induced damage: determining the damage initiation mechanisms. *Phys. Rev. Lett.*, 91(12):127402, 2003.

[101] Francois Brygo, Ch Dutouquet, F Le Guern, R Oltra, A Semerok, and JM Weulersse. Laser fluence, repetition rate and pulse duration effects on paint ablation. *Applied Surface Science*, 252(6):2131–2138, 2006.

[102] Aida Naghilou, Oskar Armbruster, and Wolfgang Kautek. Femto-and nanosecond pulse laser ablation dependence on irradiation area: The role of defects in metals and semiconductors. *Applied Surface Science*, 418:487–490, 2017.

[103] Oskar Armbruster, Aida Naghilou, Markus Kitzler, and Wolfgang Kautek. Spot size and pulse number dependence of femtosecond laser ablation thresholds of silicon and stainless steel. *Applied Surface Science*, 396:1736–1740, 2017.

[104] N Farid, SS Harilal, H Ding, and A Hassanein. Emission features and expansion dynamics of nanosecond laser ablation plumes at different ambient pressures. *Journal of Applied Physics*, 115(3):033107, 2014.

[105] L Torrisi, S Gammino, L Andò, V Nassisi, D Doria, and A Pedone. Comparison of nanosecond laser ablation at 1064 and 308 nm wavelength. *Applied Surface Science*, 210(3-4):262–273, 2003.

[106] H. Wollnik and M. Przewloka. Time-of-flight mass spectrometers with multiply reflected ion trajectories. *International Journal of Mass Spectrometry and Ion Processes*, 96(3):267 – 274, 1990.

[107] Tsviki Y Hirsh, Nancy Paul, Mary Burkey, Ani Aprahamian, Fritz Buchinger, Shane Caldwell, Jason A Clark, Anthony F Levand, Lin Ling Ying, Scott T Marley, et al. First operation and mass separation with the CARIBU MR-TOF. *Nuclear Instruments and Methods in Physics Research Section B: Beam Interactions with Materials and Atoms*, 376:229–232, 2016.

[108] Christian Jesch, Timo Dickel, Wolfgang R Plaß, Devin Short, Samuel Ayet San Andres, Jens Dilling, Hans Geissel, Florian Greiner, Johannes Lang, Kyle G Leach, et al. The MR-TOF-MS isobar separator for the TITAN facility at TRIUMF. In *TCP 2014*, pages 175–184. Springer, 2017.

[109] P Chauveau, P Delahaye, G De France, S El Abir, J Lory, Y Merrer, M Rosenbusch, L Schweikhard, and RN Wolf. PILGRIM, a multi-reflection time-of-flight mass spectrometer for Spiral2-S3 at GANIL. *Nuclear Instruments and Methods in Physics Research Section B*, 376:211–215, 2016.

[110] P Schury, M Wada, Y Ito, D Kaji, F Arai, M MacCormick, I Murray, H Haba, S Jeong, S Kimura, et al. First online multireflection time-of-flight mass measurements of isobar chains produced by fusion-evaporation reactions: Toward identification of superheavy elements via mass spectroscopy. *Phys. Rev. C*, 95(1):011305, 2017.

[111] F Wienholtz, D Beck, K Blaum, Ch Borgmann, Martin Breitenfeldt, R Burcu Cakirli, S George, F Herfurth, JD Holt, M Kowalska, et al. Masses of exotic calcium isotopes pin down nuclear forces. *Nature*, 498(7454):346, 2013.

[112] Y. Ito, P. Schury, M. Wada, F. Arai, H. Haba, Y. Hirayama, S. Ishizawa, D. Kaji, S. Kimura, H. Koura, M. MacCormick, H. Miyatake, J. Y. Moon, K. Morimoto, K. Morita, M. Mukai, I. Murray, T. Niwase, K. Okada, A. Ozawa, M. Rosenbusch, A. Takamine, T. Tanaka, Y. X. Watanabe, H. Wollnik, and S. Yamaki. First direct mass measurements of nuclides around $Z = 100$ with a multireflection time-of-flight mass spectrograph. *Phys. Rev. Lett.*, 120:152501, Apr 2018.

[113] E Leistenschneider, MP Reiter, S Ayet San Andrés, B Kootte, JD Holt, P Navrátil, C Babcock, Carlo Barbieri, BR Barquest, J Bergmann, et al. Dawning of the N= 32 shell closure seen through precision mass measurements of neutron-rich titanium isotopes. *Phys. Rev. Lett.*, 120(6):062503, 2018.

[114] RN Wolf, F Wienholtz, D Atanasov, D Beck, K Blaum, Ch Borgmann, F Herfurth, M Kowalska, Susanne Kreim, Yu A Litvinov, et al. ISOLTRAP's multi-reflection time-of-flight mass separator/spectrometer. *International Journal of Mass Spectrometry*, 349:123–133, 2013.

[115] T Dickel, WR Plaß, A Becker, U Czok, H Geissel, E Haettner, C Jesch, W Kinsel, M Petrick, C Scheidenberger, et al. A high-performance multiple-reflection time-of-flight mass spectrometer and isobar separator for the research with exotic nuclei. *Nuclear Instruments and Methods in Physics Research Section A*, 777:172–188, 2015.

[116] Christian Jesch. *The multiple-reflection time-of-flight isobar separator for TITAN and direct mass measurements at the FRS Ion Catcher*. PhD thesis, Universitätsbibliothek Giessen, 2016.

[117] Wolfgang R Plaß et al. Multiple-reflection time-of-flight mass spectrometry. *International Journal of Mass Spectrometry*, 349:134, 2013.

[118] D. Ioanoviciu. The application of ion optics in time-of-flight mass spectrometry. *International Journal of Mass Spectrometry and Ion Processes*, 131(Supplement C):43, 1994.

[119] Mikhail Yavor. Chapter 8 time-of-flight mass analyzers. In *Optics of Charged Particle Analyzers*, volume 157 of *Advances in Imaging and Electron Physics*, page 283. Elsevier, 2009.

[120] T Kalvas. Beam extraction and transport. *arXiv:1401.3951*, 2014.

[121] Klaus Floettmann. Some basic features of the beam emittance. *Phys. Rev. Special Topics-Accelerators and Beams*, 6(3):034202, 2003.

[122] Mikhail I Yavor, Wolfgang R Plaß, Timo Dickel, Hans Geissel, and Christoph Scheidenberger. Ion-optical design of a high-performance multiple-reflection time-of-flight mass spectrometer and isobar separator. *International Journal of Mass Spectrometry*, 381:1–9, 2015.

[123] M Rosenbusch, P Chauveau, P Delahaye, G Marx, L Schweikhard, F Wienholtz, and RN Wolf. Delayed bunching for multi-reflection time-of-flight mass separation. In *AIP Conference Proceedings*, volume 1668, page 050001. AIP Publishing LLC, 2015.

[124] Timo Dickel, Mikhail I Yavor, Johannes Lang, Wolfgang R Plaß, Wayne Lippert, Hans Geissel, and Christoph Scheidenberger. Dynamical time focus shift in multiple-reflection time-of-flight mass spectrometers. *International Journal of Mass Spectrometry*, 412:1–7, 2017.

[125] D. Manura and D. Dahl. *SIMION v8.1*. Scientific Instrument Services Inc., 2012.

[126] P Bratley and BL Fox. Implementing sobols quasirandom sequence generator (algorithm 659). *ACM Transactions on Mathematical Software*, 29(1):49–57, 2003.

[127] Susan Baldwin. Compute canada: Advancing computational research. *Journal of Physics: Conference Series*, 341(1):012001, 2012.

[128] S Purushothaman, S Ayet San Andrés, J Bergmann, T Dickel, J Ebert, H Geissel, C Hornung, WR Plaß, C Rappold, C Scheidenberger, et al. Hyper-emg: A new probability distribution function composed of exponentially modified gaussian distributions to analyze asymmetric peak shapes in high-resolution time-of-flight mass spectrometry. *International Journal of Mass Spectrometry*, 421:245–254, 2017.

[129] Ines Inc. Fab-3226 data sheet, 2022-08-16. https://www.inesinc.com/products/fab-3226-bit-pattern-generator.html.

[130] Burle. Channeltron electron multiplier handbook for mass spectrometry applications. 2001.

[131] M Krems, J Zirbel, M Thomason, and Robert D DuBois. Channel electron multiplier and channelplate efficiencies for detecting positive ions. *Review of Scientific Instruments*, 76(9):093305, 2005.

[132] CAEN. *DPP-ZLEplus User Manual*. 2014.

[133] Jon I Apinaniz, Borja Sierra, Roberto Martinez, Asier Longarte, Carolina Redondo, and Fernando Castano. Ion kinetic energy distributions and mechanisms of pulsed laser ablation on Al. *The Journal of Physical Chemistry C*, 112(42):16556–16560, 2008.

[134] J.S. Coursey, D.J. Schwab, J.J. Tsai, and R.A. Dragoset. NIST atomic weights and isotopic compositions (version 4.1), 2015. http://physics.nist.gov/Comp Access Date: [2022, 09, 19].

Appendix A

MRTOF Power Supply Connections

Table A.1 Electrode connections and typical operational voltages used for the MRTOF

Ion Optics		
Electrode	HV Supply	Bias (V)
LIS001	HVS004-CH0	1163
LIS002	HVS004-CH1	1140
LIS003	HVS004-CH2	600
LIS004	HVS004-CH3	200
TL	HVS004-CH4	550
TR	HVS004-CH5	-620
BR	HVS004-CH6	660
BL	HVS004-CH7	-550
XY2U	HVS004-CH8	-30
XY2R	HVS004-CH9	0
XY1U	HVS004-CH10	15
XY1R	HVS004-CH11	0
E2L2	HVS002-CH0	-1500
E1L2	HVS002-CH1	0

Table A.2 Electrode connections and operational voltages used for 400 revolution measurements of Cu.

Ion Optics		
Electrode	HV Supply	Bias (V)
LIS001	HVS004-CH0	1200
LIS002	HVS004-CH1	1160
LIS003	HVS004-CH2	800
LIS004	HVS004-CH3	200
TL	HVS004-CH4	550
TR	HVS004-CH5	-680
BR	HVS004-CH6	650
BL	HVS004-CH7	-550
XY2U	HVS004-CH8	-12.5
XY2R	HVS004-CH9	0
XY1U	HVS004-CH10	5
XY1R	HVS004-CH11	0
E2L2	HVS002-CH0	-1100
E1L2	HVS002-CH1	0
CEM Bias	HVS002-CH5	-2200
CEM FP	HVS000-CH5	1000

.

Analyzer		
Electrode	HV Supply	Voltage (V)
EME3	HVS000-CH0	1006.5
EXME3	HVS000-CH0	1006.5
EME4	HVS000-CH1	1147.2
EXME4	HVS000-CH1	1147.2
EME5	HVS000-CH2	-305.5
EXME5	HVS000-CH2	-305.5
EME6	HVS000-CH3	-2883.34
EXME6	HVS000-CH3	-2883.34

Switched Electrodes				
Electrode	Switch Code	HV Supply	Input	Voltage (V)
EME1	M3S1	terminated	in-1	GND
		HVS001-CH1	in-2	1704.0
		HVS001-CH2	in-3	1600.5
EME2	M3S2	terminated	in-1	GND
		HVS001-CH4	in-2	1650.3
		HVS001-CH3	in-3	1600.5
EXME1	S4	terminated	Low	GND
		HVS001-CH4	High	1712.0
EXME2	S2	terminated	Low	GND
		HVS001-CH4	High	1650.7

Appendix B

MRTOF Optics and Analyzer Drawings

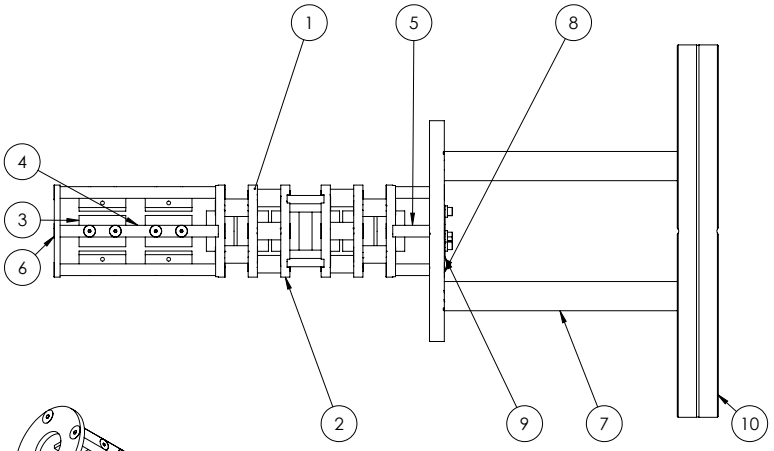

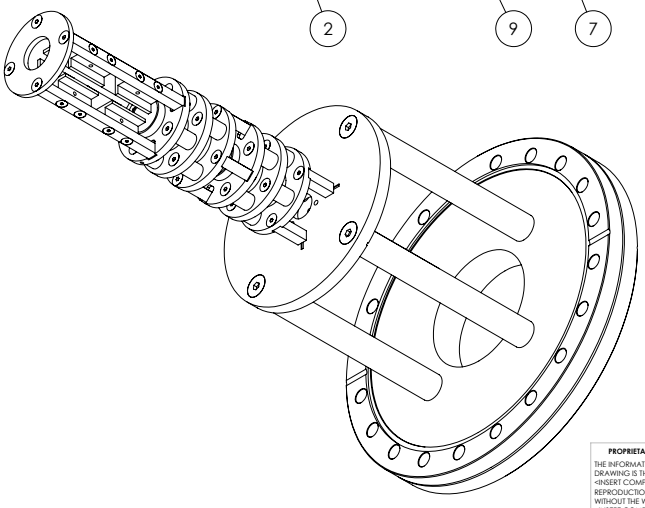

Assembly No.	Qty
MRT_assm_010s	1

ITEM NO.	PART NUMBER	DESCRIPTION	QTY.
1	MRT012s_0319	Einzel Lens 1	2
2	MRT011s_0319	Einzel Lens 2	4
3	MRT014s_0319	X-Y Deflector	8
4	MRT013s_0319	X-Y Rod	4
5	MRT016s_0319	Einzel Standoff	8
6	MRT021_0319	Optics End Cap	1
7	MRT017s_0319	Support Rod	4
8	MRT018s_0319	Optics Mounting Plate	1
9	MRT020s_0319	Collimator	1
10	dff800x000	F0800X000NT	1
11	FA-605-A_0319		32
12	94335A125		16
13	FA-606-As_0319		20
14	FA-608-As_0319		4
15	FA-2012-As_0319		4
16	nBend_4_40_hat_0319		6
17	C-405-A		3
18	FA-406-A		16
19	T-2016-A		4
20	WFV-25-A	NOT SPECIFIED	4

UNLESS OTHERWISE SPECIFIED:

DIMENSIONS ARE IN INCHES
TOLERANCES:
FRACTIONAL ±
ANGULAR: MACH ± BEND ±
TWO PLACE DECIMAL ±
THREE PLACE DECIMAL ±

INTERPRET GEOMETRIC TOLERANCING PER:

MATERIAL

FINISH

NEXT ASSY | USED ON

APPLICATION | DO NOT SCALE DRAWING

	NAME	DATE
DRAWN		
CHECKED		
ENG APPR.		
MFG APPR.		
Q.A.		

COMMENTS:

TITLE: Optics

SIZE	DWG. NO.	REV
B	MRT_assm_010s	5

SCALE: 1:5 | WEIGHT: | SHEET 1 OF 1

ITEM NO.	PART NUMBER	DESCRIPTION	QTY.
1	MRT011s_0319	Einzel Lens 2	4

Top View

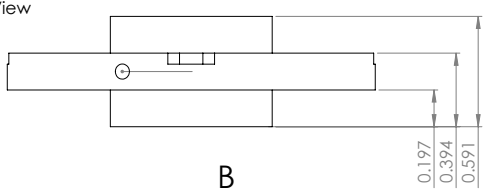

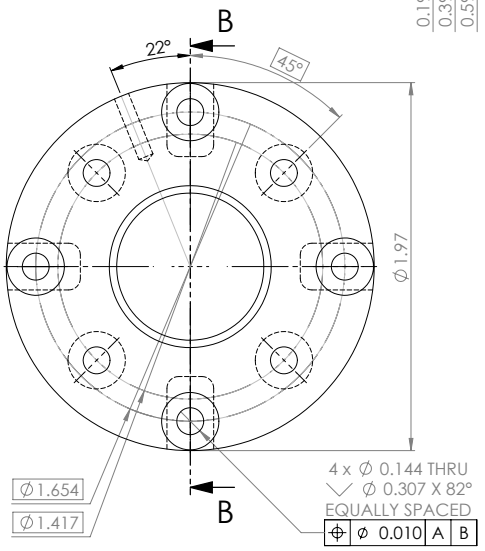

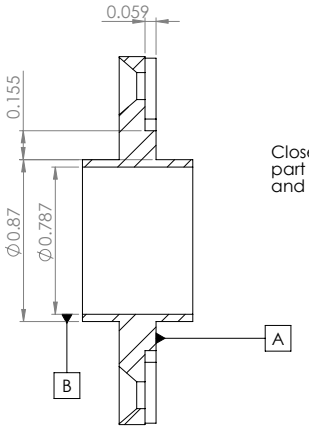

SECTION B-B

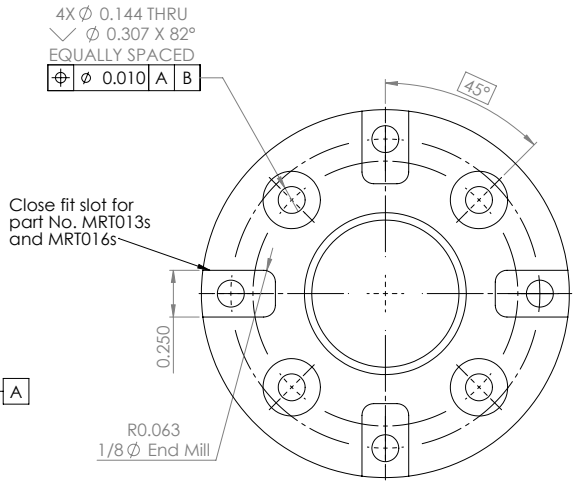

View normal to
banana plug hole

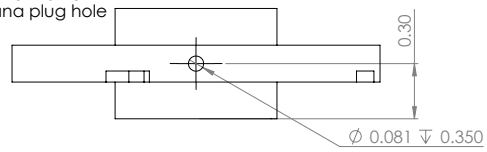

		UNLESS OTHERWISE SPECIFIED:		NAME	DATE
		DIMENSIONS ARE IN INCHES TOLERANCES: FRACTIONAL ± ANGULAR: MACH ±0.1 BEND ± TWO PLACE DECIMAL ±0.01 THREE PLACE DECIMAL ±0.005	DRAWN		
			CHECKED		
			ENG APPR.		
			MFG APPR.		
		INTERPRET GEOMETRIC TOLERANCING PER:	Q.A.		
		MATERIAL AISI 304	COMMENTS: This piece is the outer electrode for a three piece einzel lens.		
NEXT ASSY	USED ON	FINISH			
APPLICATION		DO NOT SCALE DRAWING			

TITLE:
Einzel Ground Lens

SIZE	DWG. NO.	REV
B	MRT011s	5
SCALE: 2:1	WEIGHT:	SHEET 1 OF 1

ITEM NO.	PART NUMBER	DESCRIPTION	QTY.
1	MRT012s_0319	Einzel Lens 1	2

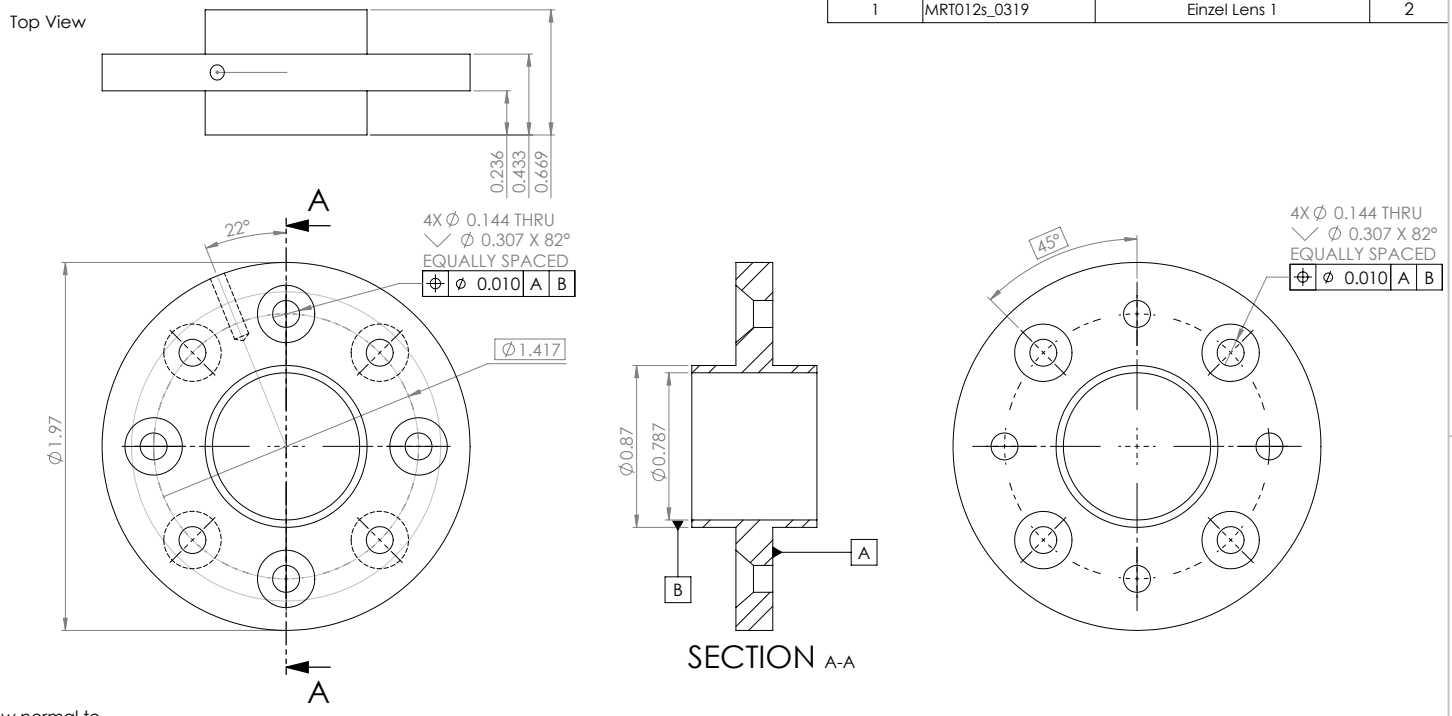

		UNLESS OTHERWISE SPECIFIED:		NAME	DATE
		DIMENSIONS ARE IN INCHES TOLERANCES: FRACTIONAL ± ANGULAR: MACH ±0.1 BEND ± TWO PLACE DECIMAL ±0.01 THREE PLACE DECIMAL ±0.005	DRAWN		
			CHECKED		
			ENG APPR.		
			MFG APPR.		
			Q.A.		
		INTERPRET GEOMETRIC TOLERANCING PER:	COMMENTS:		
		MATERIAL AISI 304	This is the middle electrode of a three piece einzel lens.		
NEXT ASSY	USED ON	FINISH			
APPLICATION		DO NOT SCALE DRAWING			

TITLE:

Einzel Floating Lens

SIZE	DWG. NO.	REV
B	MRT012s	5
SCALE: 2:1	WEIGHT:	SHEET 1 OF 1

ITEM NO.	PART NUMBER	DESCRIPTION	QTY.
1	MRT013s_0319	X-Y Rod	4

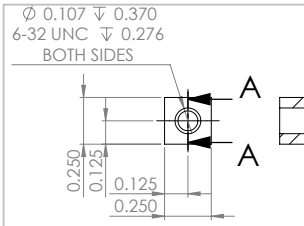

SECTION A-A
SCALE 2 : 1

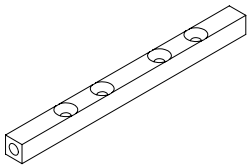

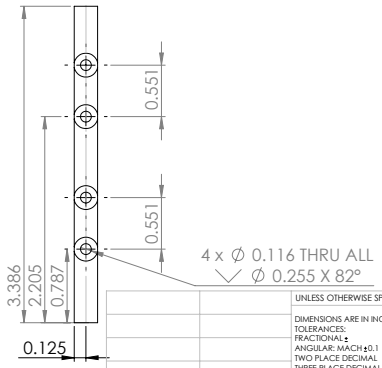

UNLESS OTHERWISE SPECIFIED:
DIMENSIONS ARE IN INCHES
TOLERANCES:
FRACTIONAL ±
ANGULAR: MACH ±0.1 BEND ±
TWO PLACE DECIMAL ±0.01
THREE PLACE DECIMAL ±0.005
INTERPRET GEOMETRIC TOLERANCING PER:
MATERIAL
Polyetheretherketone (PEEK)
FINISH
DO NOT SCALE DRAWING

	NAME	DATE
DRAWN		
CHECKED		
ENG APPR.		
MFG APPR.		
Q.A.		

COMMENTS:
An electrically insulating rod used to mount and correctly orient x-y steerers.

NEXT ASSY | USED ON
APPLICATION

TITLE:
Steerer Rod

SIZE	DWG. NO.	REV
A	MRT013s	5
SCALE: 1:1	WEIGHT:	SHEET 1 OF 1

ITEM NO.	PART NUMBER	DESCRIPTION	QTY.
1	MRT014s_0319	X-Y Deflector	8

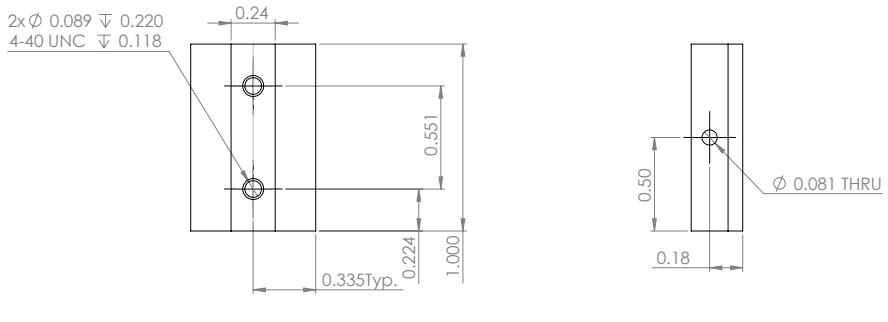

			NAME	DATE
		UNLESS OTHERWISE SPECIFIED:		
		DIMENSIONS ARE IN INCHES TOLERANCES: FRACTIONAL ± ANGULAR: MACH ± 0.01 BEND ± TWO PLACE DECIMAL ±0.01 THREE PLACE DECIMAL ±0.005	DRAWN		
			CHECKED		
			ENG APPR.		
			MFG APPR.		
			Q.A.		
		INTERPRET GEOMETRIC TOLERANCING PER:	COMMENTS:		
		MATERIAL AISI 304	Electrode for an x-y steerer used for ion beam alignment.		
NEXT ASSY	USED ON	FINISH			
APPLICATION		DO NOT SCALE DRAWING			

TITLE:

X-Y Deflector

SIZE	DWG. NO.	REV
A	MRT014s	5
SCALE: 2:1	WEIGHT:	SHEET 1 OF 1

ITEM NO.	PART NUMBER	DESCRIPTION	QTY.
1	MRT016s_0319	Einzel Standoff	8

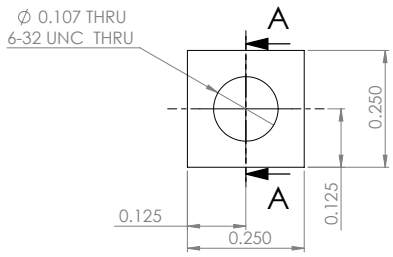

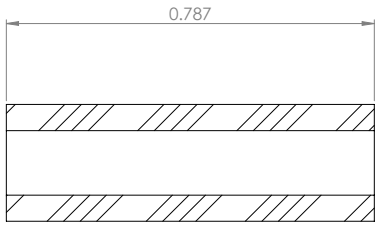

SECTION A-A

UNLESS OTHERWISE SPECIFIED:
DIMENSIONS ARE IN INCHES
TOLERANCES:
FRACTIONAL ±
ANGULAR: MACH ±0.01 BEND ±
TWO PLACE DECIMAL ±0.01
THREE PLACE DECIMAL ±0.005
INTERPRET GEOMETRIC TOLERANCING PER:
MATERIAL
Polyetheretherketone (PEEK)
FINISH
NEXT ASSY | USED ON
APPLICATION | DO NOT SCALE DRAWING

	NAME	DATE
DRAWN		
CHECKED		
ENG APPR.		
MFG APPR.		
Q.A.		

COMMENTS:
Insulating standoff between einzel lenses.

TITLE:
Einzel Standoff

SIZE	DWG. NO.	REV
B	MRT016s	5
SCALE: 5:1	WEIGHT:	SHEET 1 OF 1

ITEM NO.	PART NUMBER	DESCRIPTION	QTY.
1	MRT017s_0319	Support Rod	4

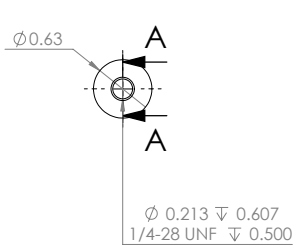

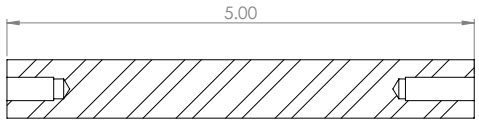

SECTION A-A
SCALE 1 : 1

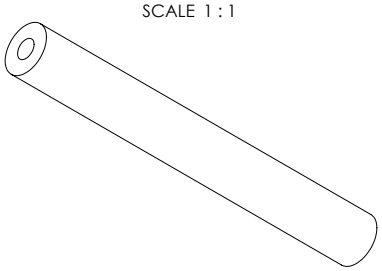

				NAME	DATE
		UNLESS OTHERWISE SPECIFIED:	DRAWN		
		DIMENSIONS ARE IN INCHES TOLERANCES: FRACTIONAL ± ANGULAR: MACH ±0.1 BEND ± TWO PLACE DECIMAL ±0.01 THREE PLACE DECIMAL ±0.005	CHECKED		
			ENG APPR.		
			MFG APPR.		
		INTERPRET GEOMETRIC TOLERANCING PER:	Q.A.		
		MATERIAL AISI 304	COMMENTS: Support rod for the optics plate.		
NEXT ASSY	USED ON	FINISH			
APPLICATION		DO NOT SCALE DRAWING			

TITLE:
Support Rod

SIZE	DWG. NO.	REV
A	MRT017s	5
SCALE: 1:2	WEIGHT:	SHEET 1 OF 1

ITEM NO.	PART NUMBER	DESCRIPTION	QTY.
1	MRT018s_0319	Optics Mounting Plate	1

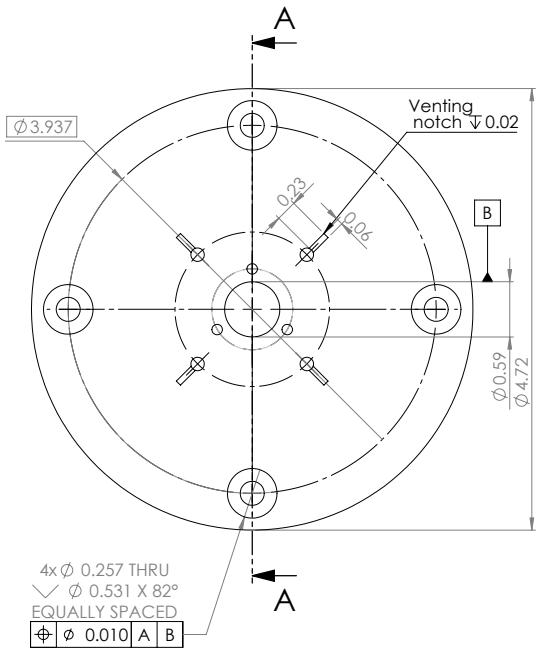

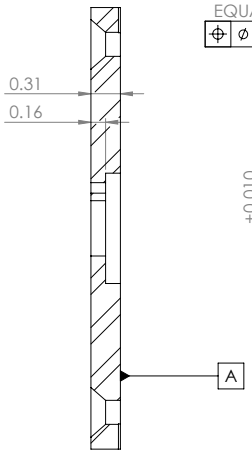

SECTION A-A

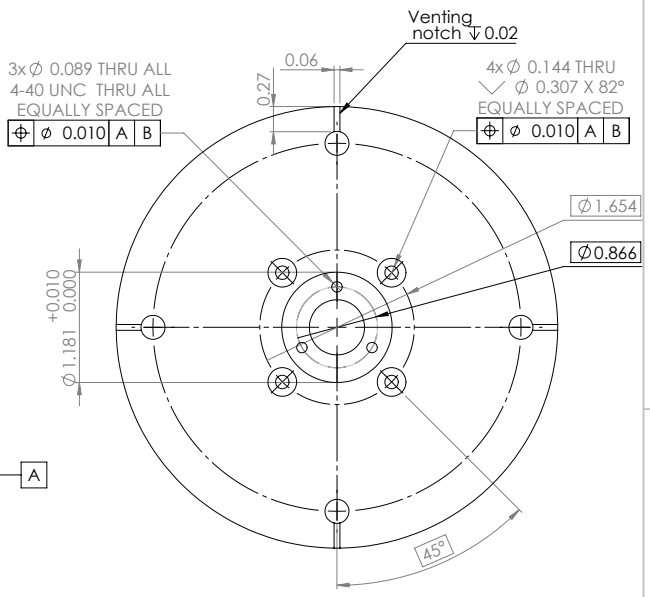

		UNLESS OTHERWISE SPECIFIED:		NAME	DATE
		DIMENSIONS ARE IN INCHES TOLERANCES: FRACTIONAL ± ANGULAR: MACH ±0.01 BEND ± TWO PLACE DECIMAL ±0.01 THREE PLACE DECIMAL ±0.005	DRAWN		
			CHECKED		
			ENG APPR.		
			MFG APPR.		
		INTERPRET GEOMETRIC TOLERANCING PER:	Q.A.		
		MATERIAL AISI 304	COMMENTS:		
NEXT ASSY	USED ON	FINISH			
APPLICATION		DO NOT SCALE DRAWING			

TITLE:
Optics Mounting Plate

SIZE	DWG. NO.	REV
B	MRT018s	5
SCALE: 1:1	WEIGHT:	SHEET 1 OF 1

ITEM NO.	PART NUMBER	DESCRIPTION	QTY.
1	MRT020s_0319	Collimator	1

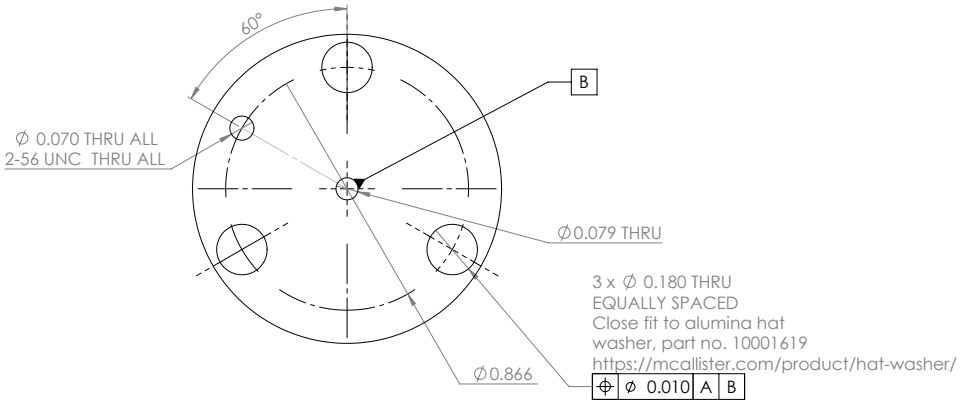

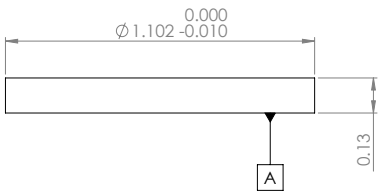

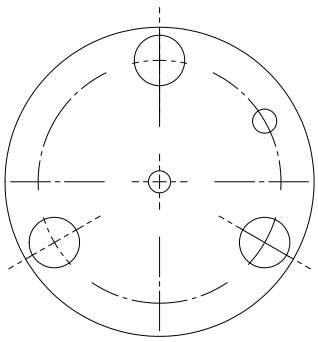

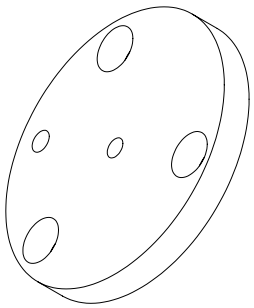

		UNLESS OTHERWISE SPECIFIED:		NAME	DATE
		DIMENSIONS ARE IN INCHES TOLERANCES: FRACTIONAL ± ANGULAR: MACH ±0.1 BEND ± TWO PLACE DECIMAL ±0.01 THREE PLACE DECIMAL ±0.005	DRAWN		
			CHECKED		
			ENG APPR.		
			MFG APPR.		
		INTERPRET GEOMETRIC TOLERANCING PER:	Q.A.		
		MATERIAL AISI 304	COMMENTS: Plate for collimating the ion beam		
NEXT ASSY	USED ON	FINISH			
APPLICATION		DO NOT SCALE DRAWING			

TITLE: Collimator

SIZE	DWG. NO.	REV
B	MRT020s_03195	
SCALE: 2:1	WEIGHT:	SHEET 1 OF 1

ITEM NO.	PART NUMBER	DESCRIPTION	QTY.
1	MRT021_0319	Optics End Cap	1

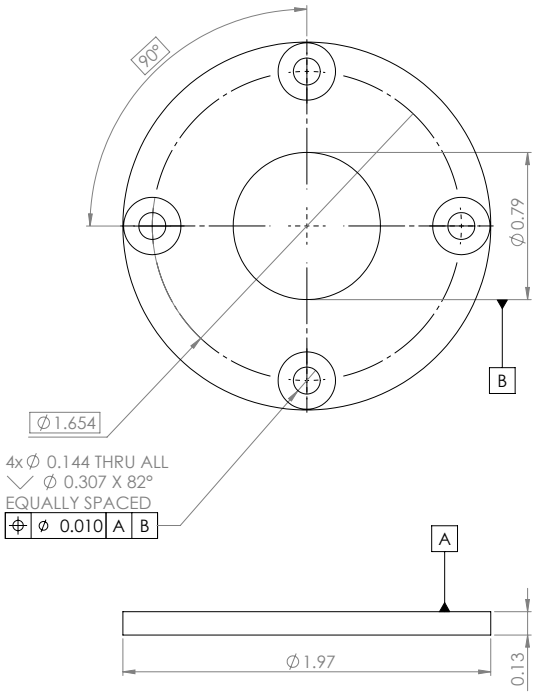

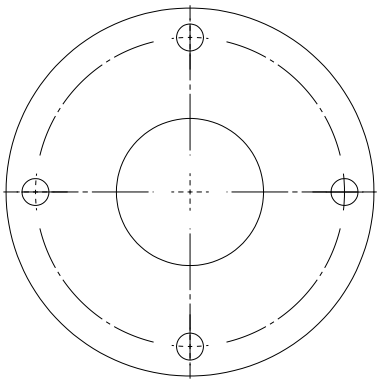

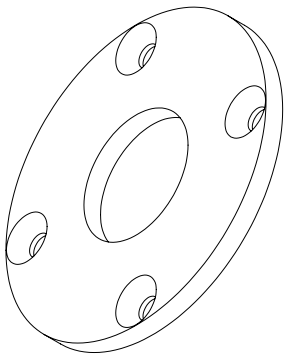

		UNLESS OTHERWISE SPECIFIED:		NAME	DATE
		DIMENSIONS ARE IN INCHES TOLERANCES: FRACTIONAL ± ANGULAR: MACH ±0.1 BEND ± TWO PLACE DECIMAL ±0.01 THREE PLACE DECIMAL ±0.005	DRAWN		
			CHECKED		
			ENG APPR.		
			MFG APPR.		
		INTERPRET GEOMETRIC TOLERANCING PER:	Q.A.		
		MATERIAL AISI 304	COMMENTS: Ground plate for field termination.		
NEXT ASSY	USED ON	FINISH			
APPLICATION		DO NOT SCALE DRAWING			

TITLE:
Optics End Cap

SIZE	DWG. NO.	REV
B	MRT021	5
SCALE: 2:1	WEIGHT:	SHEET 1 OF 1

Assembly No.	Qty
nBend_asm01	2

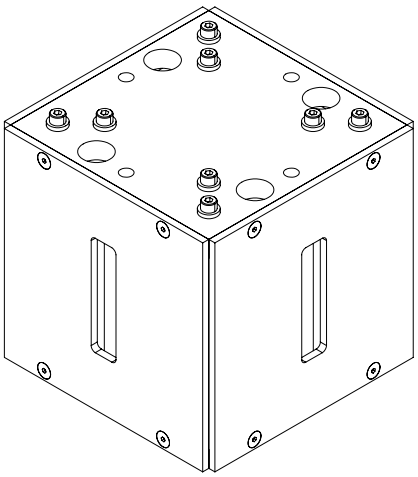

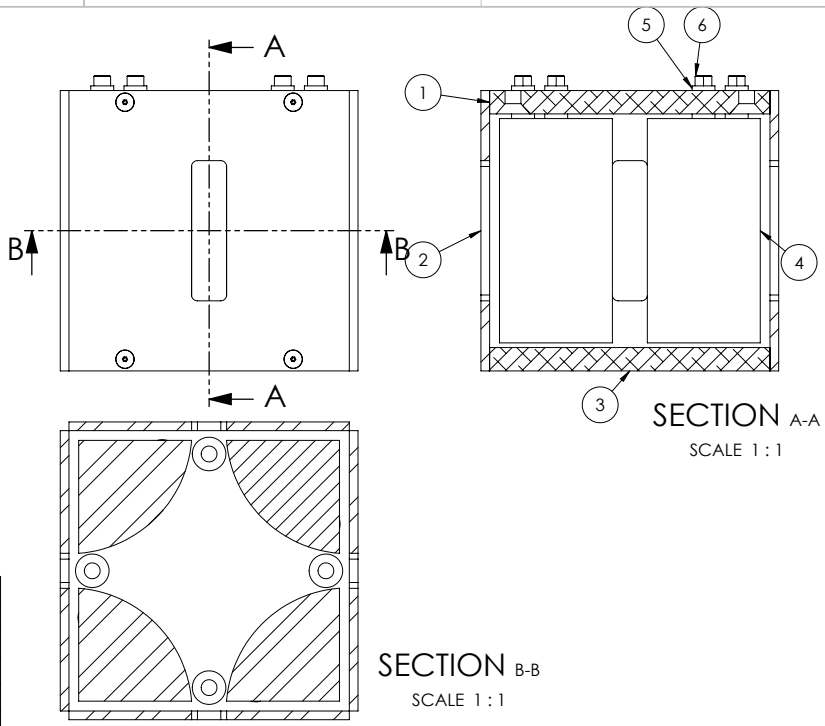

SECTION A-A
SCALE 1 : 1

SECTION B-B
SCALE 1 : 1

ITEM NO.	PART NUMBER	DESCRIPTION	QTY.
1	nBend_001_0319	Top Plate	1
2	nBend_002_0319	Side Plate	4
3	nBend_003_0319	Ground Bottom Plate	1
4	nBend_006_0319	Bending Electrode	1
5	nBend_4_40_hat_0319		4
6	nC-408-A_0319		8
11	nFA-206-A_0319		16

UNLESS OTHERWISE SPECIFIED:
DIMENSIONS ARE IN INCHES
TOLERANCES:
FRACTIONAL ±
ANGULAR: MACH ± BEND ±
TWO PLACE DECIMAL ±
THREE PLACE DECIMAL ±
INTERPRET GEOMETRIC TOLERANCING PER:
MATERIAL
FINISH
NEXT ASSY | USED ON
APPLICATION | DO NOT SCALE DRAWING

	NAME	DATE
DRAWN		
CHECKED		
ENG APPR.		
MFG APPR.		
Q.A.		
COMMENTS:		

TITLE:
Quadrupole Bender

SIZE	DWG. NO.	REV
B	nBend_asm01	5
SCALE: 1:2	WEIGHT:	SHEET 1 OF 1

ITEM NO.	PART NUMBER	DESCRIPTION	QTY.
1	nBend_001_0319	Top Plate	2

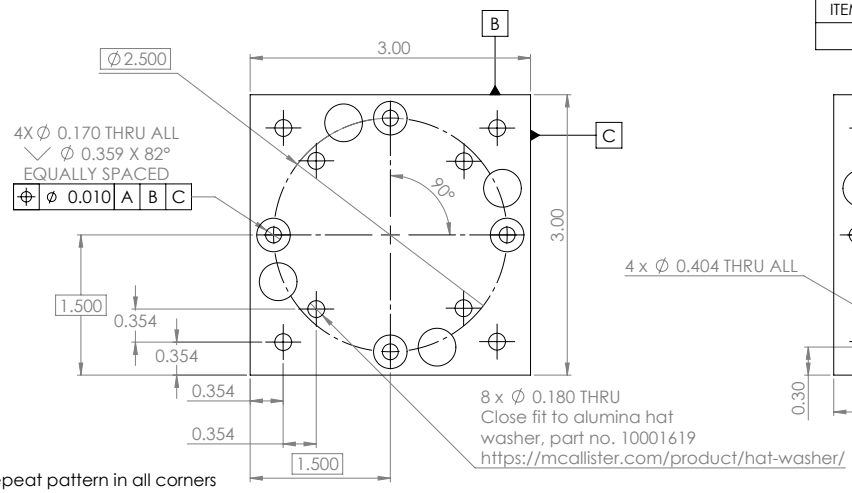

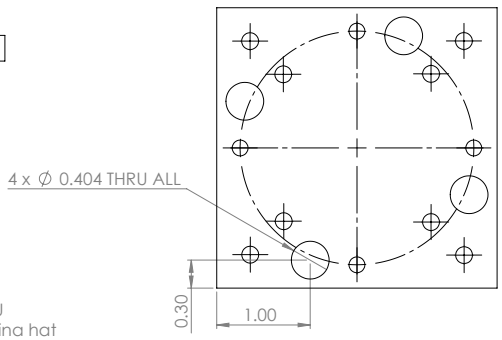

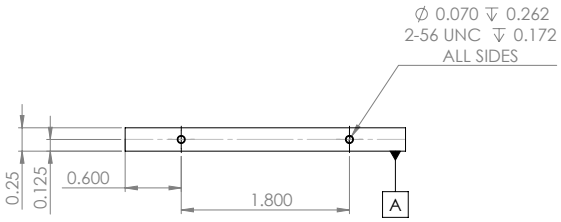

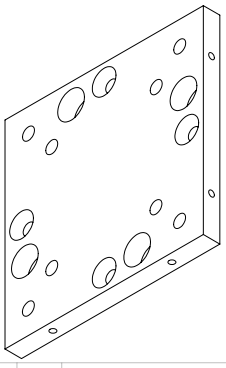

			NAME	DATE
		UNLESS OTHERWISE SPECIFIED:		
		DIMENSIONS ARE IN INCHES TOLERANCES: FRACTIONAL ± ANGULAR: MACH ±0.1 BEND ± TWO PLACE DECIMAL ±0.01 THREE PLACE DECIMAL ±0.005	DRAWN	
			CHECKED	
			ENG APPR.	
			MFG APPR.	
		INTERPRET GEOMETRIC TOLERANCING PER:	Q.A.	
		MATERIAL 6061 Alloy	COMMENTS:	
		FINISH		
NEXT ASSY	USED ON			
APPLICATION		DO NOT SCALE DRAWING		

TITLE: Top Plate

SIZE	DWG. NO.	REV
B	nBend_001	5

SCALE: 1:1 | WEIGHT: | SHEET 1 OF 1

ITEM NO.	PART NUMBER	DESCRIPTION	QTY.
1	nBend_002_0319	Side Plate	8

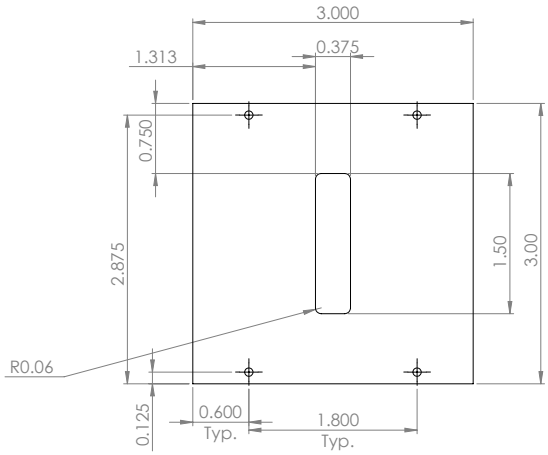

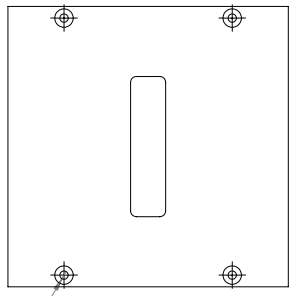

4 x ∅ 0.089 THRU ALL
⌵ ∅ 0.197 X 82°

		UNLESS OTHERWISE SPECIFIED:		NAME	DATE
		DIMENSIONS ARE IN INCHES TOLERANCES: FRACTIONAL ± ANGULAR: MACH ±0.1 BEND ± TWO PLACE DECIMAL ±0.01 THREE PLACE DECIMAL ±0.005	DRAWN		
			CHECKED		
			ENG APPR.		
			MFG APPR.		
		INTERPRET GEOMETRIC TOLERANCING PER:	Q.A.		
		MATERIAL AISI 304	COMMENTS:		
NEXT ASSY	USED ON	FINISH			
APPLICATION		DO NOT SCALE DRAWING			

TITLE: Side Plate

SIZE	DWG. NO.	REV
B	nBend_002	5

SCALE: 1:1 | WEIGHT: | SHEET 1 OF 1

ITEM NO.	PART NUMBER	DESCRIPTION	QTY.
1	nBend_003_0319	Ground Bottom Plate	2

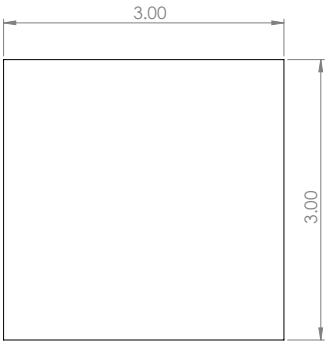

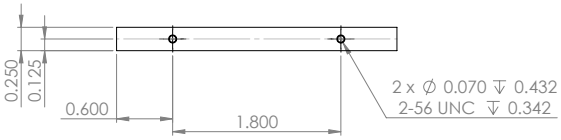

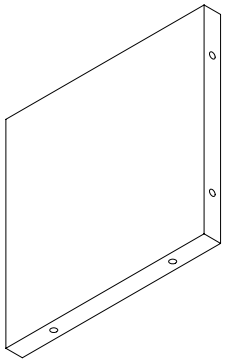

UNLESS OTHERWISE SPECIFIED:		
DIMENSIONS ARE IN INCHES TOLERANCES: FRACTIONAL ± ANGULAR: MACH ±0.1 BEND ± TWO PLACE DECIMAL ±0.01 THREE PLACE DECIMAL ±0.005		
INTERPRET GEOMETRIC TOLERANCING PER:		
MATERIAL	6061 Alloy	
FINISH		
NEXT ASSY	USED ON	
APPLICATION	DO NOT SCALE DRAWING	

	NAME	DATE
DRAWN		
CHECKED		
ENG APPR.		
MFG APPR.		
Q.A.		
COMMENTS:		

TITLE:

Ground Bottom Plate

SIZE	DWG. NO.	REV
B	nBend_003	5

SCALE: 1:1 | WEIGHT: | SHEET 1 OF 1

ITEM NO.	PART NUMBER	DESCRIPTION	QTY.
1	nBend_006_0319	Bending Electrode	8

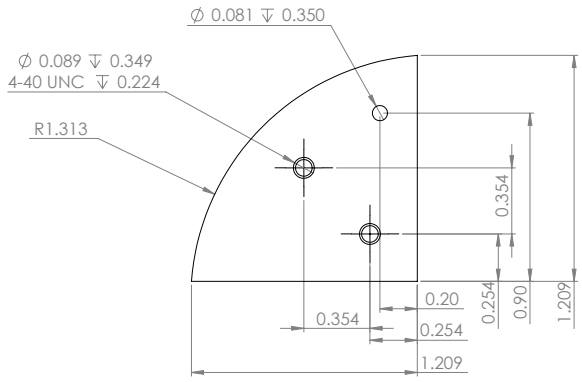

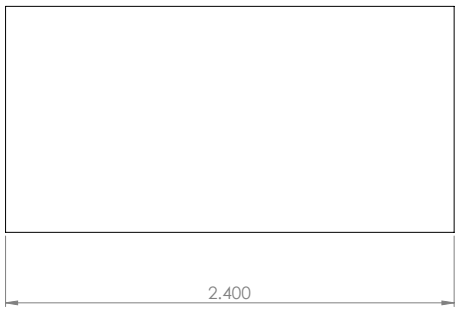

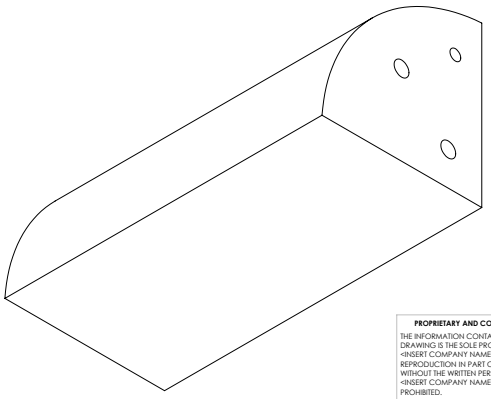

		UNLESS OTHERWISE SPECIFIED:		NAME	DATE
		DIMENSIONS ARE IN INCHES TOLERANCES: FRACTIONAL ± ANGULAR: MACH ±0.1 BEND ± TWO PLACE DECIMAL ±0.01 THREE PLACE DECIMAL ±0.005	DRAWN		
			CHECKED		
			ENG APPR.		
			MFG APPR.		
			Q.A.		
		INTERPRET GEOMETRIC TOLERANCING PER:	COMMENTS:		
		MATERIAL AISI 304	Electrode for quadrupole 90 degree bender.		
NEXT ASSY	USED ON	FINISH	**Material can be SS or Copper**		
APPLICATION		DO NOT SCALE DRAWING			

TITLE: Bending Electrode

SIZE	DWG. NO.	REV
B	nBend_006	5

SCALE: 1:1 | WEIGHT: | SHEET 1 OF 1

ITEM NO.	PART NUMBER	DESCRIPTION	QTY.
1	nQUAD001_up_0319	Quadrupole Fastener	1

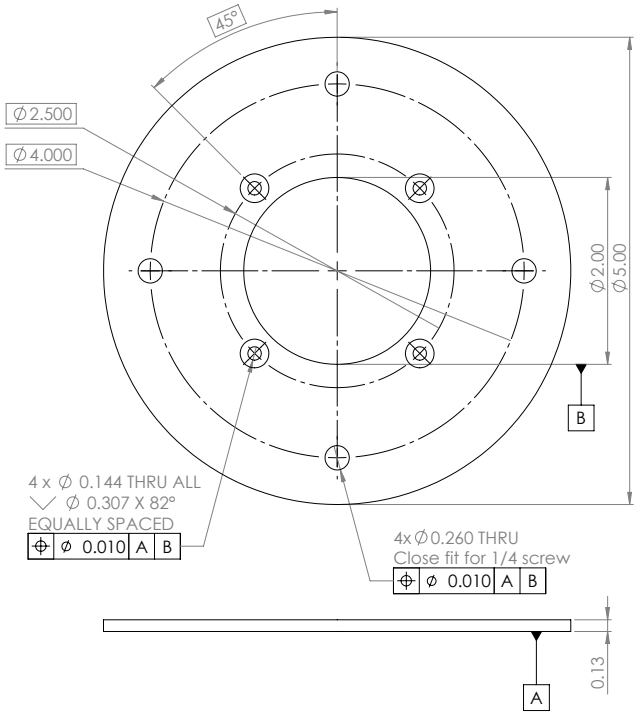

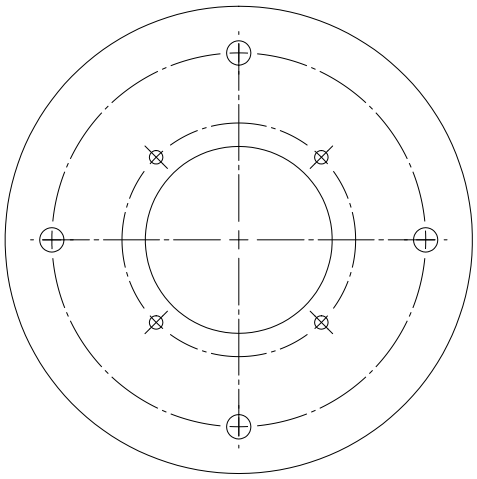

		UNLESS OTHERWISE SPECIFIED:		NAME	DATE
		DIMENSIONS ARE IN INCHES TOLERANCES: FRACTIONAL ± ANGULAR: MACH ±0.1 BEND ± TWO PLACE DECIMAL ±0.01 THREE PLACE DECIMAL ±0.005	DRAWN		
			CHECKED		
			ENG APPR.		
			MFG APPR.		
		INTERPRET GEOMETRIC TOLERANCING PER:	Q.A.		
		MATERIAL 6061 Alloy	COMMENTS: Adapter plate for mounting the Quadrupole bender.		
NEXT ASSY	USED ON	FINISH			
APPLICATION		DO NOT SCALE DRAWING			

TITLE:

Quadrupole Fastener

SIZE	DWG. NO.	REV
B	nQUAD001_up_0319	5

SCALE: 1:2 | WEIGHT: | SHEET 1 OF 1

ITEM NO.	PART NUMBER	DESCRIPTION	QTY.
1	dff800x000	F0800X000NT	1

For Reference Only

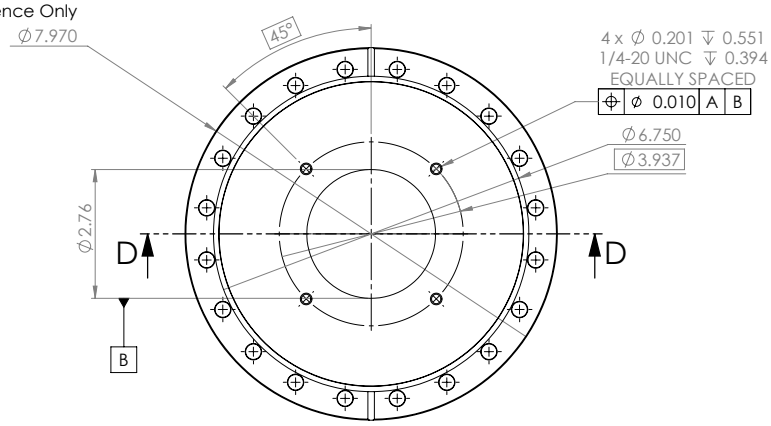

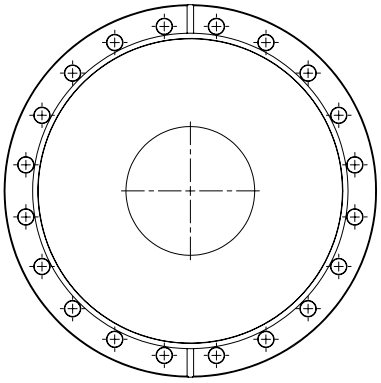

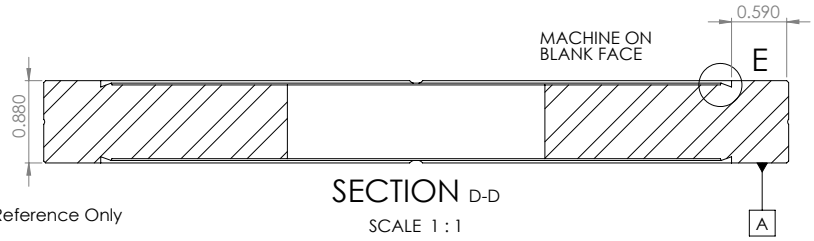

SECTION D-D
SCALE 1 : 1

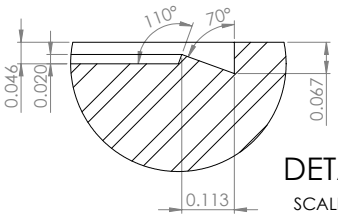

DETAIL E
SCALE 5 : 1

For Reference Only

Description: This drawing illustrates the conversion of a blank Flange from Kurt J. Lesker (Part # F0800N600TLN), into a double faced flange with custom bore.

		UNLESS OTHERWISE SPECIFIED:		NAME	DATE
		DIMENSIONS ARE IN INCHES TOLERANCES: FRACTIONAL ± ANGULAR: MACH ±0.1 BEND ± TWO PLACE DECIMAL ±0.01 THREE PLACE DECIMAL ±0.005	DRAWN		
			CHECKED		
			ENG APPR.		
			MFG APPR.		
		INTERPRET GEOMETRIC TOLERANCING PER:	Q.A.		
		MATERIAL	COMMENTS:		
NEXT ASSY	USED ON	FINISH			
APPLICATION		DO NOT SCALE DRAWING			

TITLE: F0800X000NT

SIZE	DWG. NO.	REV
B	Tap_DFF_8	5

SCALE: 1:2 | WEIGHT: | SHEET 1 OF 1

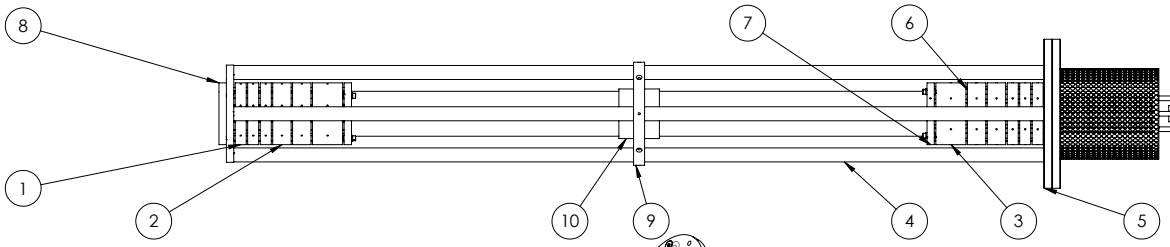

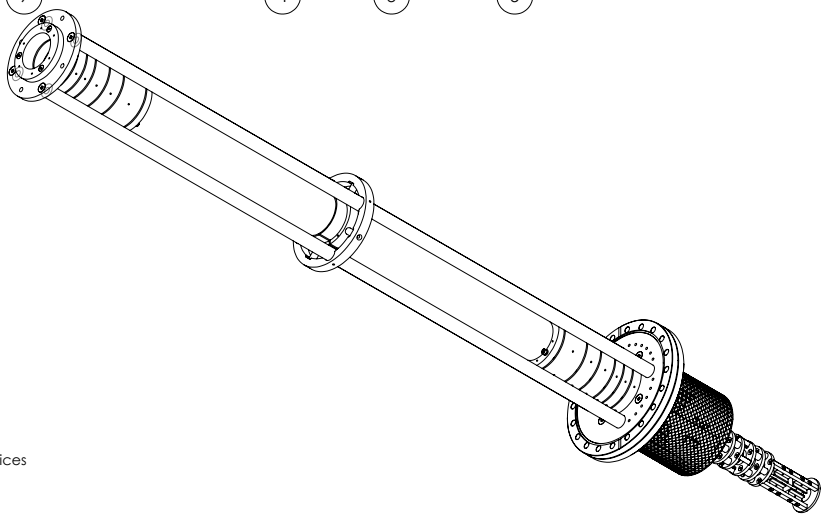

MR TOF Parts

ITEM NO.	PART NUMBER	DESCRIPTION	QTY.
1	MRT001s	Retarding Lenses 1,2,3	6
2	MRT002s	Lenses 4,5	4
3	MRT003s	Steering lens	2
4	MRT008s	Support Rod	4
5	MRT006s	DFF800x000 Baseplate	1
6	MRT007s	Mirror Rod	6
7	MRT005s	Drift Tube 1	2
8	MRT010s	End Cap Electrode	1
9	Deflector_mount	Mass Selector Mount	1
10	MRT020	Selector Hemisphere	2
11	Wire_guide	Wire Guide (Not Shown)	2

Fasteners and Ceramics

Component	Quantity
UCC FA-2024-A	8
UCC FA-2012-A	4
UCC FA-820-A	6
UCC C-816-A	6
UCC FA-610-A	4
UCC T-608-A	4
UCC T-402-A	12
5mm_diam_ceram_ball	84
MA SW-8-AlO(Hat-W)	12
MMC 94335A126	4

UCC - UC Components
MA - McAllister Technical Services
MMC - McMaster-Carr

UNLESS OTHERWISE SPECIFIED:
DIMENSIONS ARE IN INCHES
TOLERANCES:
FRACTIONAL ±
ANGULAR: MACH ± BEND ±
TWO PLACE DECIMAL ±
THREE PLACE DECIMAL ±
INTERPRET GEOMETRIC TOLERANCING PER:
MATERIAL
FINISH
NEXT ASSY | USED ON
APPLICATION | DO NOT SCALE DRAWING

	NAME	DATE
DRAWN		
CHECKED		
ENG APPR.		
MFG APPR.		
Q.A.		
COMMENTS:		

TITLE: MR TOF

SIZE B | DWG. NO. MRT_asm_009 | REV 4
SCALE: 1:20 | WEIGHT: | SHEET 1 OF 1

ITEM NO.	PART NUMBER	DESCRIPTION	QTY.
1	MRT001s	Retarding Lenses 1,2,3	6

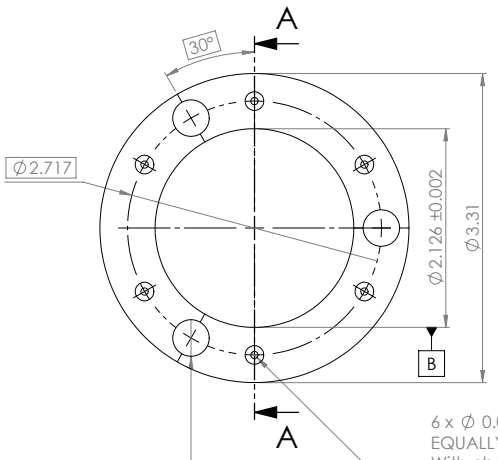

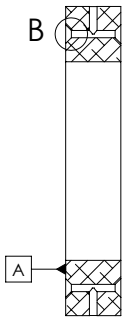

SECTION A-A

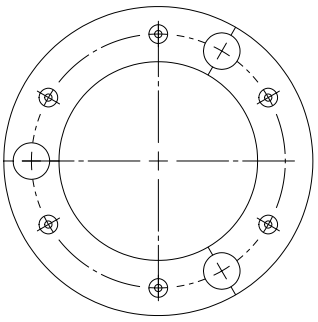

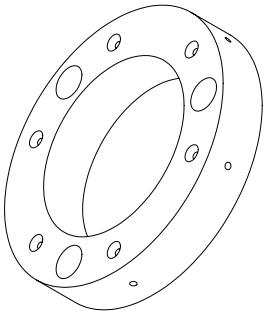

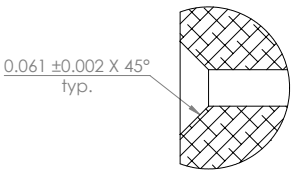

DETAIL B
SCALE 5 : 1

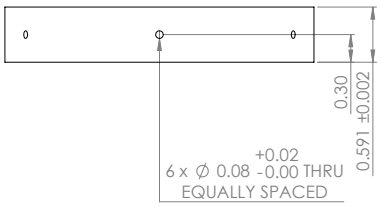

Author's note:
The tolerance of 0.002 is set to precisely space space the MR TOF electrodes (MRT001s,MRT002s,MRT003s), and ensure that they are as parallel to one another as possible. The mirrors formed by these electrodes need to be as concentric as possible

UNLESS OTHERWISE SPECIFIED:
DIMENSIONS ARE IN INCHES
TOLERANCES:
FRACTIONAL ±
ANGULAR: MACH ± BEND ±
TWO PLACE DECIMAL ±.010
THREE PLACE DECIMAL ±.005
INTERPRET GEOMETRIC TOLERANCING PER:
MATERIAL 6061 Alloy
FINISH
NEXT ASSY | USED ON
APPLICATION | DO NOT SCALE DRAWING

	NAME	DATE
DRAWN		
CHECKED		
ENG APPR.		
MFG APPR.		
Q.A.		
COMMENTS:		

TITLE: Lens 1,2,3

SIZE	DWG. NO.	REV
B	MRT001s	4
SCALE: 1:1	WEIGHT:	SHEET 1 OF 1

ITEM NO.	PART NUMBER	DESCRIPTION	QTY.
1	MRT002s	Lenses 4,5	4

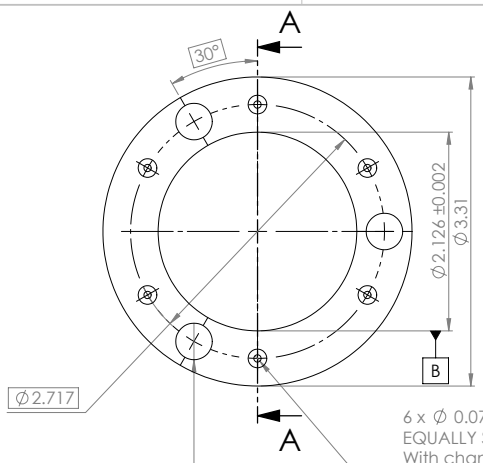

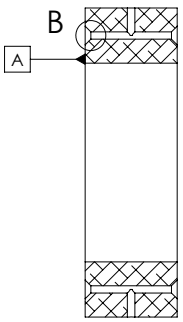

SECTION A-A

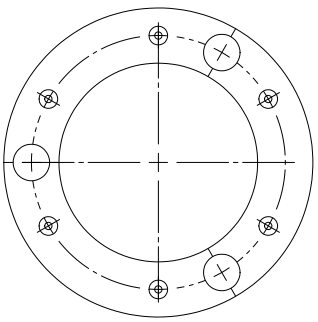

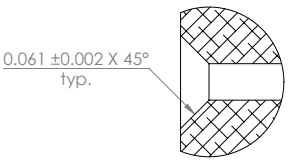

DETAIL B
SCALE 5 : 1

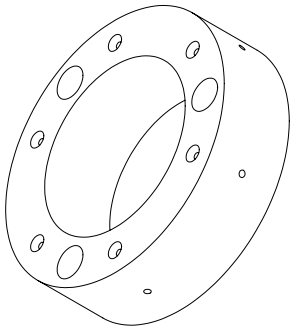

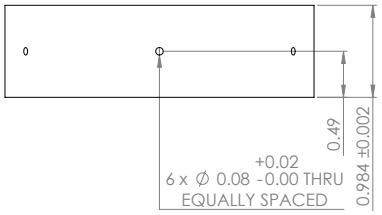

			NAME	DATE
		UNLESS OTHERWISE SPECIFIED:		
		DIMENSIONS ARE IN INCHES TOLERANCES: FRACTIONAL ± ANGULAR: MACH ± BEND ± TWO PLACE DECIMAL ±.010 THREE PLACE DECIMAL ±.005	DRAWN	
			CHECKED	
			ENG APPR.	
			MFG APPR.	
		INTERPRET GEOMETRIC TOLERANCING PER:	Q.A.	
		MATERIAL 6061 Alloy	COMMENTS:	
NEXT ASSY	USED ON	FINISH		
APPLICATION		DO NOT SCALE DRAWING		

TITLE: Lens 4,5

SIZE	DWG. NO.	REV
B	MRT002s	4
SCALE: 1:1	WEIGHT:	SHEET 1 OF 1

ITEM NO.	PART NUMBER	DESCRIPTION	QTY.
1	MRT003s	Steering lens	2

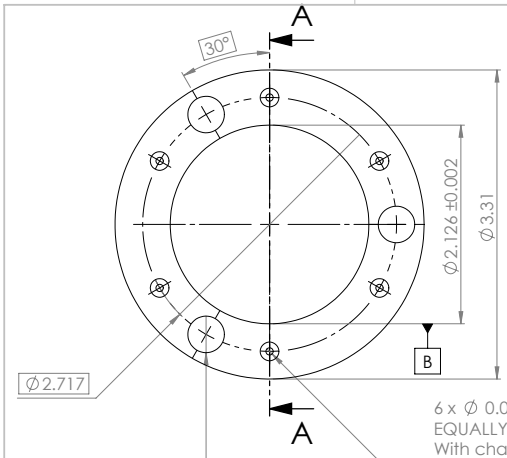

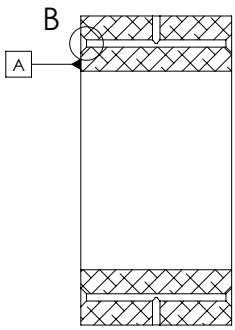

SECTION A-A

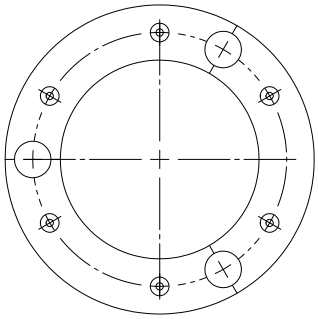

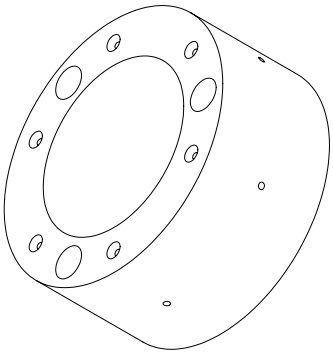

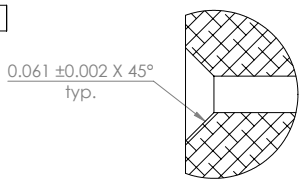

DETAIL B
SCALE 5 : 1

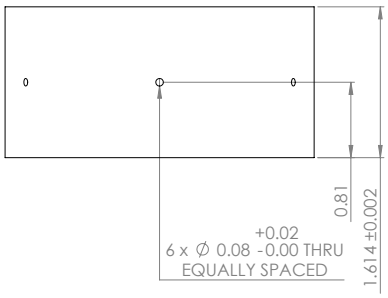

		UNLESS OTHERWISE SPECIFIED:		NAME	DATE
		DIMENSIONS ARE IN INCHES TOLERANCES: FRACTIONAL ± ANGULAR: MACH ± BEND ± TWO PLACE DECIMAL ±.010 THREE PLACE DECIMAL ±.005	DRAWN		
			CHECKED		
			ENG APPR.		
			MFG APPR.		
		INTERPRET GEOMETRIC TOLERANCING PER:	Q.A.		
		MATERIAL 6061 Alloy	COMMENTS:		
		FINISH			
NEXT ASSY	USED ON				
APPLICATION		DO NOT SCALE DRAWING			

TITLE: Steering lens

SIZE	DWG. NO.	REV
B	MRT003s	4

SCALE: 1:1	WEIGHT:	SHEET 1 OF 1

ITEM NO.	PART NUMBER	DESCRIPTION	QTY.
1	MRT005s	Drift Tube 1	2

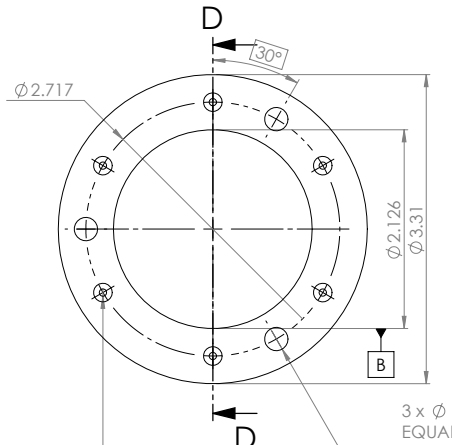

6 x ∅ 0.078±0.002 THRU
EQUALLY SPACED
With Chamfer
(Detail G)

⌖	0.002	A	B

3 x ∅ 0.250 THRU
EQUALLY SPACED
Close fit to alumina hat washer,
part number: 10003768
url: https://mcallister.com/product/hat-washer/

⌖	0.005	A	B

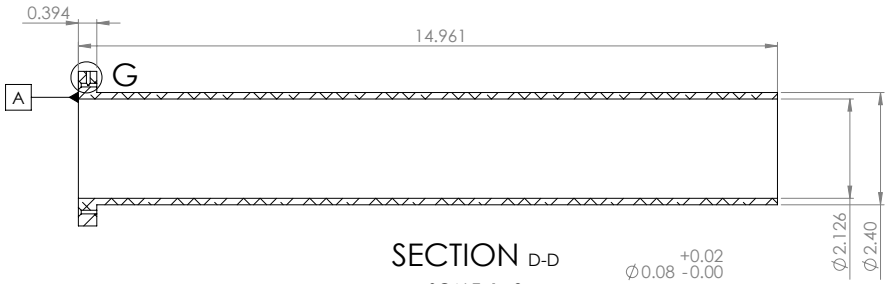

SECTION D-D
SCALE 1 : 2

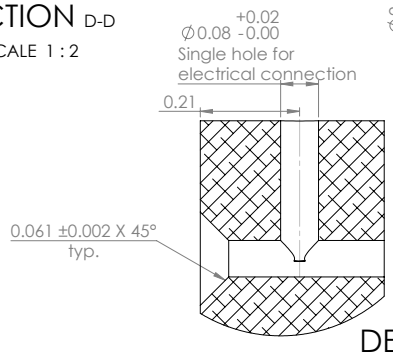

DETAIL G
SCALE 5 : 1

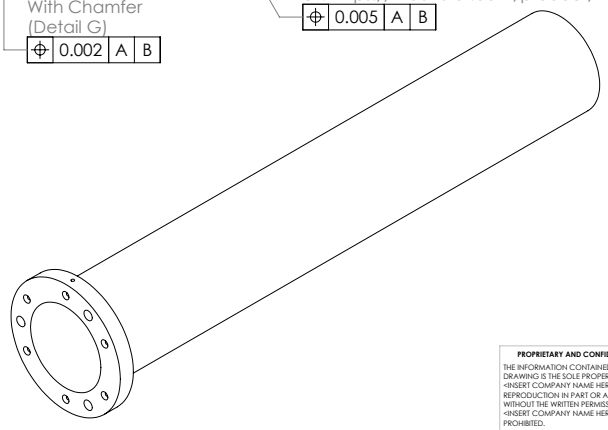

		UNLESS OTHERWISE SPECIFIED:		NAME	DATE
		DIMENSIONS ARE IN INCHES TOLERANCES: FRACTIONAL ± ANGULAR: MACH ± BEND ± TWO PLACE DECIMAL ± .010 THREE PLACE DECIMAL ± .005	DRAWN		
			CHECKED		
			ENG APPR.		
			MFG APPR.		
		INTERPRET GEOMETRIC TOLERANCING PER:	Q.A.		
		MATERIAL 6061 Alloy	COMMENTS:		
NEXT ASSY	USED ON	FINISH			
APPLICATION		DO NOT SCALE DRAWING			

TITLE: Drift Tube

SIZE	DWG. NO.	REV
B	MRT005s	4
SCALE: 1:5	WEIGHT:	SHEET 1 OF 1

ITEM NO.	PART NUMBER	DESCRIPTION	QTY.
1	MRT006s	DFF800x000 Baseplate	1

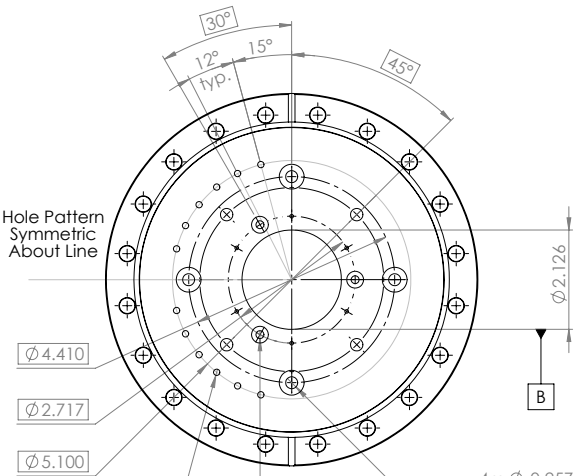

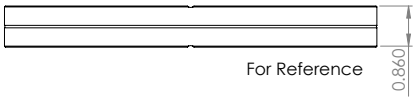

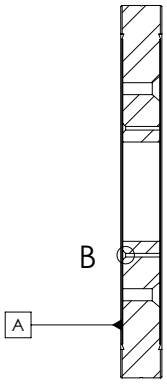

SECTION A-A

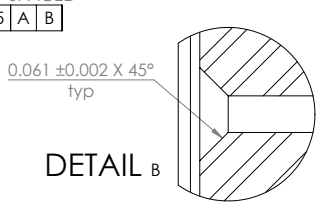

DETAIL B

SCALE 5 : 1

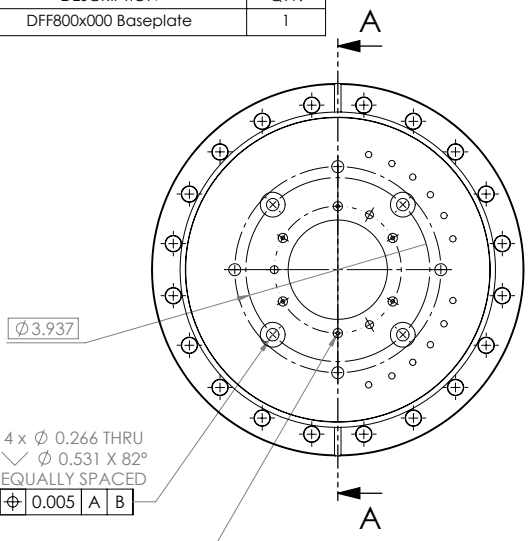

Description: This drawing is intended for a DN160CF Double Faced Flange from Kurt J. Lesker.

UNLESS OTHERWISE SPECIFIED:
DIMENSIONS ARE IN INCHES
TOLERANCES:
FRACTIONAL ±
ANGULAR: MACH ± BEND ±
TWO PLACE DECIMAL ± .010
THREE PLACE DECIMAL ± .005
INTERPRET GEOMETRIC TOLERANCING PER:
MATERIAL: Alloy Steel (SS)
FINISH
NEXT ASSY | USED ON
APPLICATION | DO NOT SCALE DRAWING

	NAME	DATE
DRAWN		
CHECKED		
ENG APPR.		
MFG APPR.		
Q.A.		
COMMENTS:		

TITLE: DFF800x000

SIZE	DWG. NO.	REV
B	MRT006s	4

SCALE: 1:2 | WEIGHT: | SHEET 1 OF 1

ITEM NO.	PART NUMBER	DESCRIPTION	QTY.
1	MRT007s	Mirror Rod	6

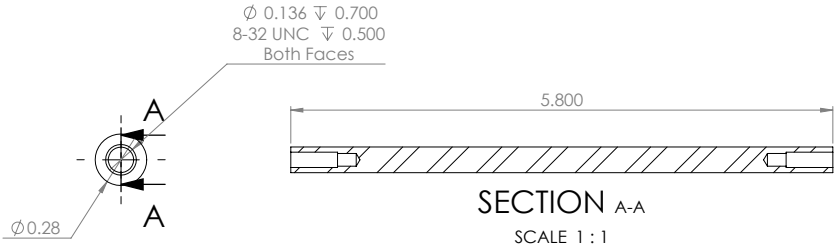

SECTION A-A
SCALE 1 : 1

				NAME	DATE
		UNLESS OTHERWISE SPECIFIED:	DRAWN		
		DIMENSIONS ARE IN INCHES TOLERANCES: FRACTIONAL ± ANGULAR: MACH ± BEND ± TWO PLACE DECIMAL ± .010 THREE PLACE DECIMAL ± .005	CHECKED		
			ENG APPR.		
			MFG APPR.		
		INTERPRET GEOMETRIC TOLERANCING PER:	Q.A.		
		MATERIAL AISI 304	COMMENTS:		
NEXT ASSY	USED ON	FINISH			
APPLICATION		DO NOT SCALE DRAWING			

TITLE: Mirror Rod

SIZE	DWG. NO.	REV
A	MRT007s	4
SCALE: 1:2	WEIGHT:	SHEET 1 OF 1

ITEM NO.	PART NUMBER	DESCRIPTION	QTY.
1	MRT008s	Support Rod	4

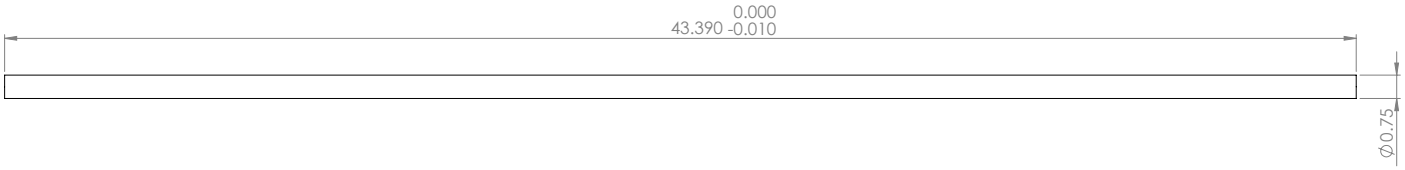

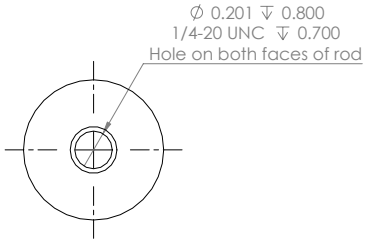

UNLESS OTHERWISE SPECIFIED:
DIMENSIONS ARE IN INCHES
TOLERANCES:
FRACTIONAL ±
ANGULAR: MACH ± BEND ±
TWO PLACE DECIMAL ± .010
THREE PLACE DECIMAL ± .005
INTERPRET GEOMETRIC TOLERANCING PER:
MATERIAL: AISI 304
FINISH
NEXT ASSY | USED ON
APPLICATION | DO NOT SCALE DRAWING

	NAME	DATE
DRAWN		
CHECKED		
ENG APPR.		
MFG APPR.		
Q.A.		
COMMENTS:		

TITLE: Support Rod

SIZE	DWG. NO.	REV
B	MRT008s	4

SCALE: 1:10 WEIGHT: SHEET 1 OF 1

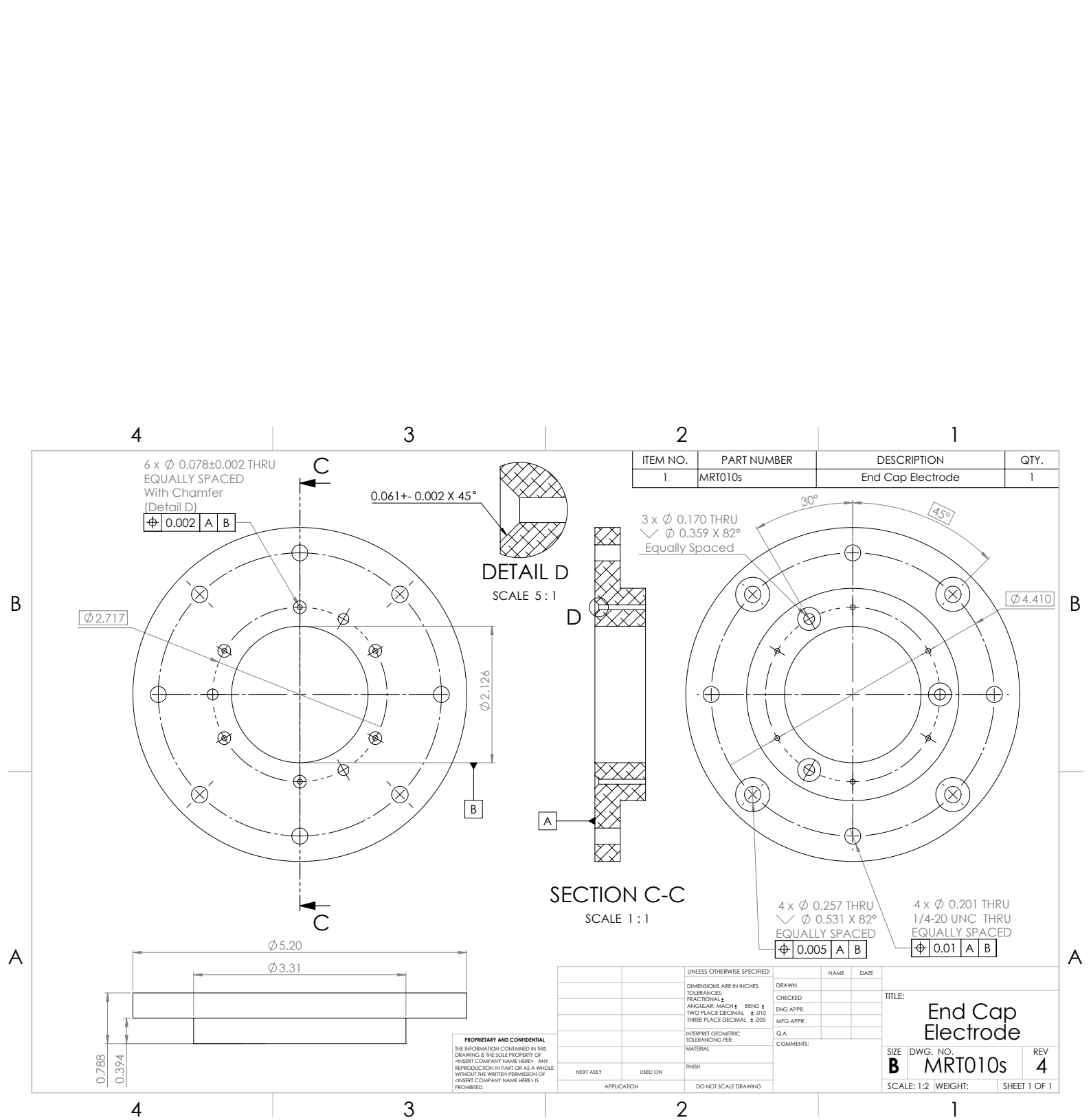

ITEM NO.	PART NUMBER	DESCRIPTION	QTY.
1	MRT010s	End Cap Electrode	1

UNLESS OTHERWISE SPECIFIED:
DIMENSIONS ARE IN INCHES
TOLERANCES:
FRACTIONAL ±
ANGULAR: MACH ± BEND ±
TWO PLACE DECIMAL ± .010
THREE PLACE DECIMAL ± .005
INTERPRET GEOMETRIC TOLERANCING PER:
MATERIAL
FINISH
NEXT ASSY | USED ON
APPLICATION | DO NOT SCALE DRAWING

	NAME	DATE
DRAWN		
CHECKED		
ENG APPR.		
MFG APPR.		
Q.A.		
COMMENTS:		

TITLE: End Cap Electrode

SIZE	DWG. NO.	REV
B	MRT010s	4
SCALE: 1:2	WEIGHT:	SHEET 1 OF 1

ITEM NO.	PART NUMBER	DESCRIPTION	QTY.
1	MRT020	Selector Hemisphere	2

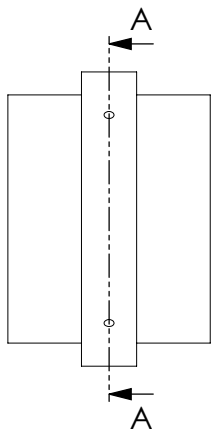

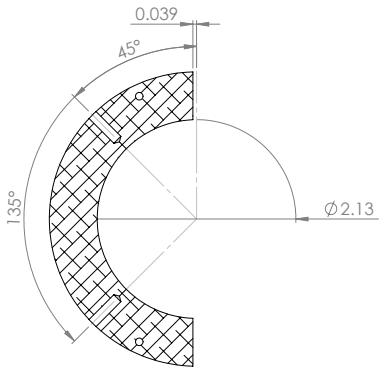

SECTION A-A

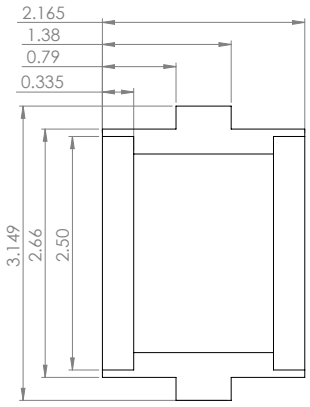

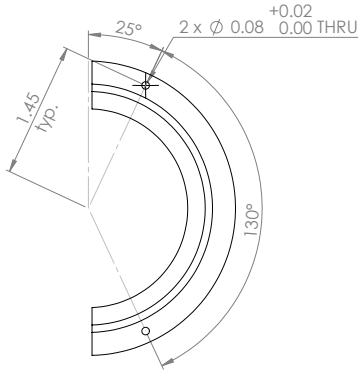

Planar View of Hole

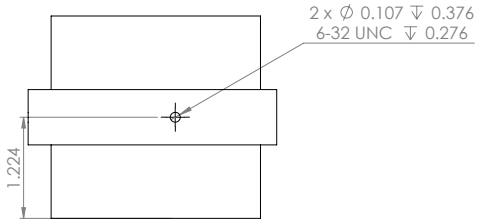

		UNLESS OTHERWISE SPECIFIED:		NAME	DATE
		DIMENSIONS ARE IN INCHES TOLERANCES: FRACTIONAL ± ANGULAR: MACH ± BEND ± TWO PLACE DECIMAL ± .010 THREE PLACE DECIMAL ± .005	DRAWN		
			CHECKED		
			ENG APPR.		
			MFG APPR.		
		INTERPRET GEOMETRIC TOLERANCING PER:	Q.A.		
		MATERIAL 6061 Alloy	COMMENTS:		
NEXT ASSY	USED ON	FINISH			
APPLICATION		DO NOT SCALE DRAWING			

TITLE: Selector Hemisphere

SIZE	DWG. NO.	REV
B	MRT020	4

SCALE: 1:1	WEIGHT:	SHEET 1 OF 1

ITEM NO.	PART NUMBER	DESCRIPTION	QTY.
1	Deflector_mount	Mass Selector Mount	1

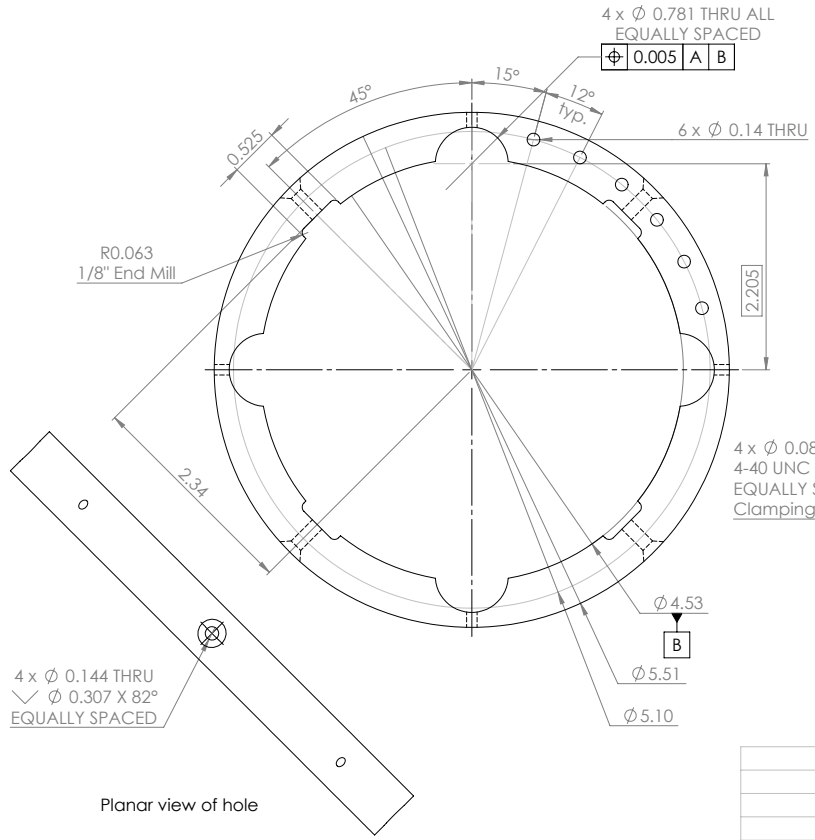

Planar view of hole

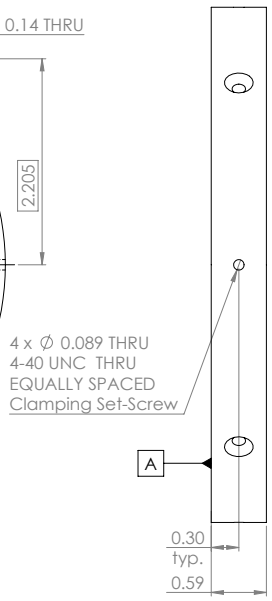

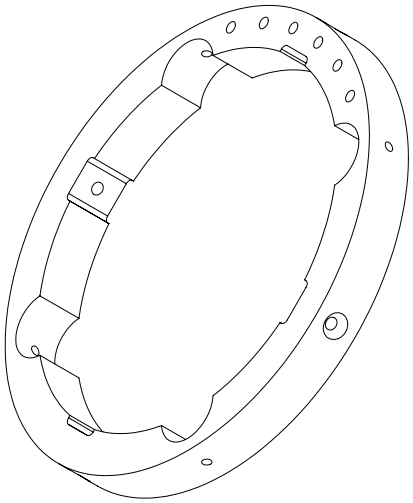

UNLESS OTHERWISE SPECIFIED:
DIMENSIONS ARE IN INCHES
TOLERANCES:
FRACTIONAL ±
ANGULAR: MACH ± BEND ±
TWO PLACE DECIMAL ± .010
THREE PLACE DECIMAL ± .005
INTERPRET GEOMETRIC TOLERANCING PER:
MATERIAL 6061 Alloy
FINISH
NEXT ASSY | USED ON
APPLICATION | DO NOT SCALE DRAWING

	NAME	DATE
DRAWN		
CHECKED		
ENG APPR.		
MFG APPR.		
Q.A.		

COMMENTS:

TITLE:
Mass Selector Mount

SIZE	DWG. NO.	REV
B	Deflector_mount	4

SCALE: 1:2 | WEIGHT: | SHEET 1 OF 1

ITEM NO.	PART NUMBER	DESCRIPTION	QTY.
1	Wire_guide	Wire Guide	2

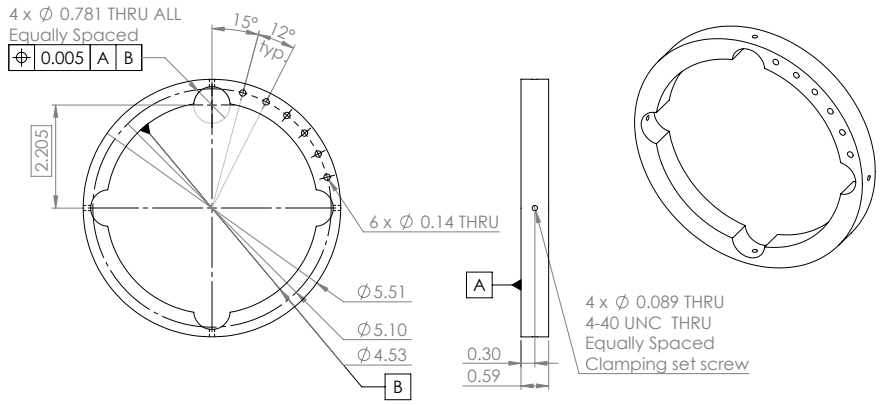

		UNLESS OTHERWISE SPECIFIED:		NAME	DATE
		DIMENSIONS ARE IN INCHES TOLERANCES: FRACTIONAL ± ANGULAR: MACH ± BEND ± TWO PLACE DECIMAL ± .010 THREE PLACE DECIMAL ± .005	DRAWN		
			CHECKED		
			ENG APPR.		
			MFG APPR.		
			Q.A.		
		INTERPRET GEOMETRIC TOLERANCING PER:	COMMENTS:		
		MATERIAL 6061 Alloy			
NEXT ASSY	USED ON	FINISH			
APPLICATION		DO NOT SCALE DRAWING			

TITLE:
Wire Guide

SIZE	DWG. NO.	REV
A	Wire_guide	4
SCALE: 1:2	WEIGHT:	SHEET 1 OF 1